

The Design and Preparation of Metal-Organic Nanosheets for Water Purification Applications



The
University
Of
Sheffield.

Freya Emily Cleasby

180126327

A thesis submitted to the University of Sheffield in partial fulfilment
of the requirements for the Degree of Doctor of Philosophy

September 2022

The University of Sheffield

Faculty of Science

Department of Chemistry



Sheffield, May 2020

Abstract

Metal-organic framework nanosheets (MONs) are a unique class of two-dimensional (2D) material. MONs can be defined as free-standing, 2D materials, approaching monolayer thickness, formed by the coordination of organic ligands with metal ions or clusters. The unique combination of properties such as large external surface areas, nanoscopic dimensions, high aspect ratio, periodic structures and tuneability has led to the use of MONs in a vast range of applications.

In recent years, there has been a growing concern over the demand for freshwater. Factors such as industrialisation, growing populations and climate change are all putting pressure on this resource. Using separation techniques such as membrane technology can enable alternative water sources such as industrial wastewater and seawater to be utilised. However, new materials are needed to overcome fundamental limitations between the permeability and selectivity of these membranes. MONs are promising candidates thanks to their tunable porosity, surface chemistry and their 2D surface area. Early publications have shown examples of high performing membranes formed using MONs can lead to improved water purification performances. In this thesis, the use of MON-membranes for water purification was explored. Extensive screening and optimisation studies were undertaken to further understand and improve the MON-membranes prepared. The synthesis of novel MONs using defect-mediated synthesis routes was also explored.

In **Chapter 2**, the synthesis of novel MONs is investigated. Using a modulating agent, analogues of UiO-66 were synthesised with defects that allowed the formation of a hexagonal close packed (**hcp**) crystal phase. It is the formation of this layered phase that allows the normally three-dimensional interpenetrated UiO-66 structure to form free-standing nanosheets. Synthesis of 2D UiO-66 analogues using tetrafluoro terephthalic acid yielded ultrathin nanosheets that undergo self-exfoliation upon suspension. The use of mixed linkers, tetrafluoro- and 2-amino- terephthalic acids, allowed the synthesis of a 2D UiO-66 analogue material containing amino functionality. The mixed linker 2D UiO-66 analogues were subjected to ultrasonic liquid exfoliation, forming monolayer nanosheets with high aspect ratios.

Chapter 3 takes the tetrafluoro terephthalate UiO-66 nanosheets and explores their use in water purification membranes. Prior to the work carried out in this thesis, the preparation and testing of water purification membranes was unknown in the Foster group. Therefore, a large focus of this chapter was development of the processes of membrane preparation, optimisation, and water purification testing. Important lessons about additive solubility and the importance of homogeneity in MON active layers were learnt.

Using the optimised MON loadings from the previous chapter, an extensive screening study was conducted in **Chapter 4**. Five different MONs were deposited onto membranes and tested for water purification efficacy. From this screening study, it was identified that Zr-4''(pyridine-2,4,6-triyl)tribenzoate (Zr-PTB) MONs were the most promising candidate and were taken forward for optimisation in **Chapter 5**. Optimisation of loadings, inclusion of polydopamine as an additive and the introduction of a compression step to the membrane preparation yielded a Zr-PTB membrane with stable rejection of 84 %.

Overall, this thesis demonstrates the how MONs can be utilized for the improvement of water purification membranes. It also offers some insight into modulated synthesis routes to allow the formation of MONs from non-layered structures. The growing field of MONs and their unique set of properties demonstrates why MONs have significant potential in water purification applications.

Acknowledgements

First and foremost, I offer my absolute gratitude to my supervisor, **Dr Jonathan Foster**, thank you for your invaluable guidance, insight, and support throughout this PhD. Sometimes I required a kick up the arse, and sometimes I needed a supportive word of encouragement, all of which and much more you have offered. **Jona**, your dedication to your students, willingness to improve and unwavering high standards makes you everything a supervisor should strive to be. I will never forget the mentor you have been to me.

Thank you both to **Dr Rob Dawson** and **Dr Tim Easun** for taking on the roles of my examiners. Thank you for taking the time to read this work, I hope it is as interesting as it is long.

Thank you to the Foster group past and present, I couldn't have imagined my PhD experience with a better group of people. **Dr Dave Ashworth, Dr Josh Nicks, Dr Kezia Sasitharan**, thank you for imparting your incredible knowledge, wisdom, and love for snacks upon me, I doubt I'd have made it through first year without you. **Dr Ram Prasad, Dr Charlotte Kiker, Benedict Smith, Jiangtian (Andy) Tan and Sanyou (Victor) Xu**, you have all been fantastic colleagues, I hope the lab hasn't collapsed without me and I wish you all every success in the future. Thanks to **Mike Harris**, it's been a joy to go through the last 4 years together, I'll miss reminding you of everything and of course the cakes! Special shout out to **Amelia Wood**, what a best friend you have become, I am so glad you joined the Foster group and will miss seeing you every day! You inspire me with your hard work and inherent coolness, I know great things are in store for you!

The PhD experience extends beyond your research group, and without the D85 alumni, **Dr Alex James, Dr Jenny Train, Dr James Railton, Dr Dylan Pritchard**, and other D-floor inhabitants, **Dr Thomas Roserveare, Dr Samantha Peralta** and the rest of the Brammer and Weinstein groups, I wouldn't have done nearly as many crosswords or had nearly as much fun.

I am especially thankful to the staff within the Department of Chemistry at the University of Sheffield, without whom none of us would achieve our PhDs. **Dr Craig Robertson, Denise Richards, Simon Thorpe, Elaine Frary, Nick Smith** and **Sharon Curl**, thank you all for your time, patience and expertise.

Thank you to the **Polymers, Soft Matter and Colloids CDT**, and the **EPSRC** for funding this PhD, and to **Jennifer Dick** for being a fantastic CDT manager, even after your contract ended. To my fellow 5th cohort members – thank you for making the CDT business days and summer schools so much fun. Additionally thank you to **Evo** for partially funding this work, and to my industrial supervisors **Dr Kangsheng Lui** and **Dr Fan Fei** for your expert advice and freedom in this research.

I have been fortunate to make many friends during my time in Sheffield, all of whom have kept me going and made life so much fun over the last 8 years in the city. My flatmates from first year, **Gillian Mackie, Jordan Sullivan, Katie Lonsdale, Rhys Prosser**, and honorary extra **Tom Elliot**, I feel so lucky that we were all put in A6 together, thank you for being fantastic friends, even after we've all departed Sheffield. To the G-floor lunch crew, **Alice Rhind-Tutt, Amelia Wood, Beth Ritchie, Courtney Thompson, Ellen Quane, Jonny Gregg, Josh Hayles, Reuben Ouanounou, Simon Fawcett** and **Xander Praet** and the many more additions, thank you all for the laughs. **Courtney Thompson**, my oldest friend, we have shared so many memories since CERN all those years ago and I am so proud of the

person you've grown into. I can't wait to make more memories with you and **Suraj Smith**. Thanks also to **Dan Murray, Alan Hoodless, and Luke Quane** for all the drunken evenings and games nights.

To my incredible family, I can't thank you all enough. **Nannie, Auntie Helen, Archie, and Uncle Rich** thank you for your unwavering support and continued interest despite having absolutely no idea what I've been talking about these past 4 years. **Grandma** and **Grandpa**, thank you so much for your generosity, without it I doubt I'd have had the same university experience and certainly wouldn't have been able to move to London. **Elliot**, thank you for being there for me in Sheffield, I'll really miss living so close to you. **Mum** and **Dad**, I cannot put into words how grateful I am to you both, but I'll try. You are the best parents I could wish for, and I wouldn't be where I am without you. You pushed and believed in me so much, I hope I've done you both proud.

Finally, **Sam**, my love. Thank you for everything, but mostly for believing in me, for pushing me to work harder, inspiring me with your passion for your job, making me laugh till I cry, and for moving across the country with me. You make my life infinitely better for being in it and I can't wait for all our future adventures.



Peak District, Jan 2020

Author's Declaration

This research has been performed between the months of October 2018 and October 2022, within the Department of Chemistry at the University of Sheffield, under the supervision of Dr Jonathan Foster.

1st referee Dr Robert Dawson, The University of Sheffield

2nd referee, external Dr Timothy Easun, The University of Cardiff

I, the author, confirm that this Thesis is my own work. I am aware of the University's Guidance on the Use of Unfair Means (www.sheffield.ac.uk/ssid/unfair-means). This work has not previously been presented for an award at this, or any other, university.

Table of Contents

Abstract	i
Acknowledgements	ii
Author's declaration	iv
Table of contents	v
List of common abbreviations	viii
Chapter 1: Introduction and review of literature	1
1.1 Water purification	2
1.2 Membrane filtration	4
1.3 Composite and mixed matrix membranes	7
1.4 Metal-organic frameworks for water purification	8
1.5 2D materials for water purification	11
1.6 Membrane characterisation and tests	12
1.7 Metal-organic nanosheets	14
1.7.1 Synthesis and exfoliation	15
1.7.2 Bottom-up synthesis	15
1.7.3 Top-down synthesis	18
1.7.4 MON characterisation	20
1.7.5 Applications	21
1.8 MONs for water purification	23
1.8.1 Examples of MON-membranes in the literature	23
1.9 Conclusions	36
1.10 References	38
Chapter 2: Defect-mediated synthesis to access nanosheet phases of UiO family metal-organic frameworks	43
2.1 Introduction	44
2.2 Results and discussion	46
2.2.1 Synthesis and characterisation of $Zr_6(F_4BDC)$	46
2.2.2 Synthesis and characterisation of $Zr_6(NH_2:F_4BDC)$	51
2.2.3 Synthesis and characterisation of $Zr_6(BDC)$ and $Zr_6(BrBDC)$	60
2.3 Conclusions	63
2.4 References	66
Chapter 3: Preparation and water purification performance of $Zr_6(F_4BDC)$ membranes	66
3.1 Introduction	68
3.2 Results and discussion	70
3.2.1 Pristine PES membrane	70
3.2.2 $Zr_6(F_4BDC)$ membranes on PES supports	71
3.2.3 $Zr_6(F_4BDC)$ /PDDA membranes on PES supports	73
3.2.4 PDDA effect on absorbance measurements	78

3.2.5	Zr ₆ (F ₄ BDC)/PDDA membranes on different pore size PES supports	81
3.2.6	Zr ₆ (F ₄ BDC) “MON-only” membranes	83
3.3	Conclusions	85
3.4	References	87
Chapter 4:	Preliminary testing of metal-organic nanosheets for the use in water purification membranes	89
4.1	Introduction	90
4.2	Results and discussion	90
4.2.1	Pristine PES membrane	90
4.2.2	CuBDC	91
4.2.3	NH ₂ -MIL-53	94
4.2.4	ZIF-7	98
4.2.5	Zr-tricarboxylates	101
4.3	Conclusions	106
4.4	References	107
Chapter 5:	Preparation and water purification performance of Zr-PTB membranes	109
5.1	Introduction	110
5.2	Results and discussion	112
5.2.1	Synthesis and characterisation of Zr-tricarboxylates	112
5.2.2	Zr-tricarboxylate MON membranes on PES supports	114
5.2.3	Compression step optimisation	116
5.2.4	Prolonged testing	120
5.2.5	Zr-PTB membranes with additives on PES supports	122
5.2.6	Zr-PTB/GO membranes on PES supports	122
5.2.7	Zr-PTB/PDA membranes on PES supports	124
5.3	Conclusion	127
5.4	References	128
Chapter 6:	Conclusions and outlook	130
6.1	Summary of aims	131
6.2	Synthesis of water stable MONs	131
6.3	Development of MON based membranes	133
6.4	Industrial applicability	135
6.5	Outlook	135
6.6	References	136
Chapter 7:	Experimental techniques	137
7.1	Metal-organic nanosheet synthesis and exfoliation	138
7.1.1	Zr ₆ (XBDC) compounds	138
7.1.1.1	Zr ₆ (F ₄ BDC)	139
7.1.1.2	Zr ₆ (NH ₂ :F ₄ BDC)	140
7.1.1.3	Zr ₆ (XBDC) liquid exfoliation	142

7.1.2	CuBDC	143
7.1.3	NH ₂ -MIL-53	143
7.1.4	ZIF-7	144
7.1.5	Zr-tricarboxylates	145
7.1.6	Membrane preparation	146
7.1.7	MON/PDDA membranes	146
7.1.8	MON/GO membranes	146
7.1.9	MON/PDA membranes	146
7.2	Characterisation	147
7.2.1	Atomic force microscopy	147
7.2.2	Dynamic light scattering	147
7.2.3	Elemental analysis	147
7.2.4	Nuclear magnetic resonance spectroscopy	147
7.2.5	Powder x-ray diffraction	148
7.2.6	Scanning electron microscopy	148
7.2.7	Thermogravimetric analysis	148
7.2.8	Ultraviolet-visible spectroscopy	148
7.2.9	Water purification testing	149
7.3	References	150

List of Common Abbreviations

Please note, all abbreviations are defined at first use in each chapter. Some abbreviations are only used in one chapter, and are not included in this list, which is intended to summarise terms used across multiple chapters.

2D	Two-dimensional
3D	Three-dimensional
AFM	Atomic force microscopy
BDC	1,4-benzenedicarboxylate
BTB	1,3,5-benzenetribenzoate
DLS	Dynamic light scattering
DMF	<i>N,N</i> -dimethylformamide
DEC	Dead end cell
EtOH	Ethanol
F ₄ BDC	Tetrafluoro-1,4-benzenedicarboxylate
fcu	Face-centred-cubic
GO	Graphene oxide
hcp	Hexagonal-close-packed
hns	Nanosheet phase
LMHB	L m ⁻² h ⁻¹ bar ⁻¹
MIL	Matériaux de l'Institut Lavoisier
MOF	Metal-organic framework
MON	Metal-organic nanosheet
NH ₂ BDC	2-amino-1,4-benzenedicarboxylate
PES	Polyethersulfone
PDA	Polydopamine
PDDA	Polydiallyldimethylammonium chloride
PTB	4''-(pyridine-2,4,6-triyl)tribenzoate
PXRD	Powder x-ray diffraction
SEM	Scanning electron microscopy
UiO	Universitetet i Oslo
UV-Vis	Ultraviolet visible
VF	Vacuum filtration
ZIF	Zeolitic imidazolate framework

Chapter 1

Introduction and Review of Literature

1.1. Water purification

Clean, safe drinking water is essential for all life on earth and it is becoming a dwindling resource due to growing populations, industrialisation and climate change.^{1,2} With the deficiency of safe drinking water collectively accounting for 3.1% of death worldwide (in 2002), addressing the ever growing demand for safe, clean water is one of the biggest challenges of our time.³ In addition to the need for clean drinking water, industrialisation has led to an increase demand for water as a crucial feedstock. This in turn has led to an increase in wastewater production and it is estimated that the annual water consumption by industry to rise by 50% from 1995 by 2025.³ From this growth in industry, fresh water sources are being contaminated with micropollutants such as pharmaceuticals, personal care products and industrial chemicals, all of which can have detrimental health affects even at low concentrations.⁴

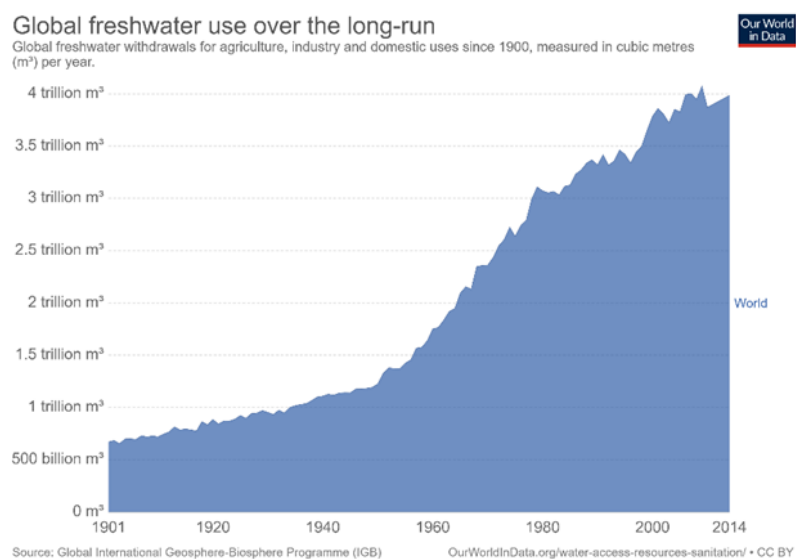


Figure 1.1. Global freshwater use for agriculture, industrial and domestic uses from 1900-2014. Figure adapted from reference 3.

Despite over 70% of the earth's surface being covered by water, only around 2.5% of this is freshwater, a large amount of which is inaccessible, trapped in glaciers and underground reservoirs (Figure 1.2).^{3,5} This means the utilisation of unconventional water sources must be explored to meet the growing water demand. Seawater is the most abundant source of water on earth, however the high salinity means it is not fit for domestic and industrial uses.³ In developing regions, such as countries in North

Africa, desalination of sea water might serve as a viable approach to providing a fresh drinking water supply.⁶ One of the largest aspects of water purification is recycling wastewater from industrial processes. Additionally, nutrients, resources and other substances of value such as pharmaceuticals and plastics can be extracted and the water recycled.⁴

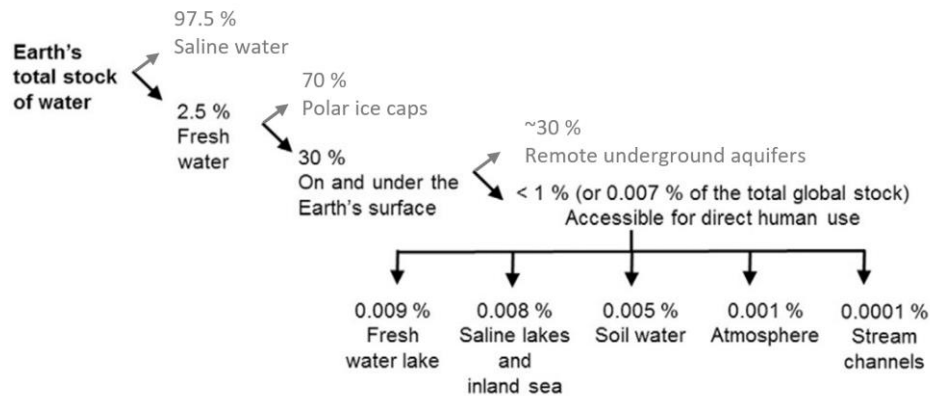


Figure 1.2. Flow chart showing the global stock of fresh water. Figure adapted from reference 7.

A range of conventional treatment processes have been developed which have been applied to water purification for the removal of contaminants, including coagulation-flocculation-sedimentation-filtration, ozonation, adsorption, membrane filtration and ultrasonication.⁸ Of these methods, polymeric membranes historically have been at the forefront of water purification and desalination, with excellent long term track records.⁶ However these systems are not without their limitations, namely the trade-off between flux and selectivity and problems arising from membrane fouling and chemical instability. Membrane lifetime, mechanical integrity, chemical and thermal stability, along with scalability for manufacturing and cost are also factors that need to be taken into account when developing separation membranes.⁹

With the challenge of meeting growing global water demands, new materials are needed to address the current membrane limitations. One of the types of new material that can be utilized in this area are composite and mixed matrix membranes. This class of material combines polymers and inorganic fillers to enhance membrane performance.¹⁰ Improved selectivity and flux, fouling resistance and improved hydrophilicity are all areas that can be targeted with the inclusion of inorganic materials.^{6,8}

Mixed matrix and composite membranes combine the processibility and variety of forms from polymeric membranes with the physicochemical stability from inorganic materials, and the often tunable selectivity from porous inorganic materials.

Two dimensional (2D) materials have shown promise as fillers in water purification membranes. Their properties such as ultrathin thickness, high surface areas and mechanical strength have been shown to improve membrane performance.¹¹

Despite advances already made, the demand for new materials to overcome the current limitations of water purification membrane technology is still growing. This thesis explores how combining the growing field of 2D metal-organic nanosheets (MONs) with polymer membranes could serve to address some of the issues faced by current water purification membranes. This chapter aims to discuss key concepts and literature relating to water purification membranes and metal-organic nanosheets. Firstly, membrane technology, types of filtration and methods for improving membrane performance will be introduced. The design, synthesis and applications of MONs will be discussed, followed by an in depth analysis of the current MON water purification literature.

1.2. Membrane filtration

Membrane based technologies are commonly used in separation processes due to their high energy efficiency, low cost and environmental friendliness. In this case we can define a membrane as a semi-permeable barrier that retains contaminants and allows water to pass through.¹⁰

There are a variety of different types of membrane filtration which are classified according to the size of the particle to be removed and the mechanism used to achieve this.¹² Microfiltration (MF) and ultrafiltration (UF) are classified as low-pressure (<2 bar) processes. These membranes allow molecules to pass through using a pore-flow mechanism in which the feed solution passes through pores with a pressure-driven convective flow. Separation is achieved between different permeants due to one permeant being excluded from the pores.^{9,13} Separation in MF membranes approximately occurs between 0.1 – 1.0 μm , removing particles, bacteria, some viruses, and colloids. For UF

membranes rejection occurs between 0.01 and 0.1 μm , allowing the removal of pathogens, viruses, and colloids.⁹

Nanofiltration (NF) and reverse osmosis (RO) are referred to as high pressure processes as they both require high hydraulic pressures. In nanofiltration membranes, a combination of solution-diffusion and pore-flow mechanisms are seen when molecules pass through (Figure 1.3).¹² The solution diffusion mechanism occurs when permeants diffuse through the membrane material at a concentration gradient.¹³ The differences in amount of material that dissolves into the membrane and the rate of diffusion gives rise to the separation. In nanofiltration solutes are rejected via a number of mechanisms (steric, dielectric, Donnan exclusion and adsorption) as illustrated in Figure 1.3.^{9,14} In reverse osmosis, it was widely thought that molecules primarily pass through via a solution-diffusion mechanism, however studies have recently shed light on the complexity of the RO desalination mechanism.¹² A more recent model proposed, the solution-friction model, suggests that the mechanism of water transport and ion rejection in RO membranes depends on steric, dielectric and Donnan exclusions as well as concentration, electric potential and hydraulic pressure gradients.¹⁵

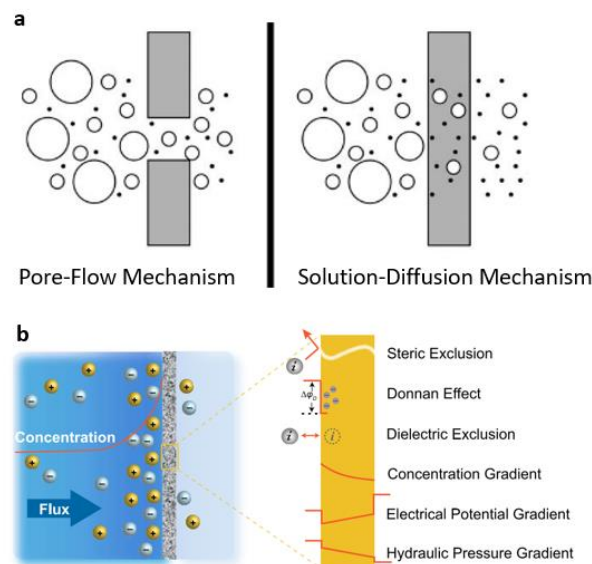


Figure 1.3. Schematic illustration of different transport mechanisms seen in membranes. (a) pore-flow (MF, UF, NF) and solution-diffusion mechanisms (NF), (b) solution-friction model (RO). Images reproduced from references 12 and 15.

Polymer based membranes currently dominate the membrane market, the wide range of polymers available and their flexibility to be fabricated into a variety of membrane types makes them very attractive candidates. Examples of common commercial polymers used for filtration membranes are polyether sulfone (PES), polyvinylidene fluoride (PVDF), polyethylene (PE), polypropylene (PP), polytetrafluoroethylene (PTFE) and polyacrylonitrile (PAN).⁷ These can be fabricated into a variety of membrane types, including flat-sheet, spiral wound and hollow fibre membranes.⁷

Polymeric membrane technology faces two big limitations; membrane fouling, and the trade-off between flux and selectivity. Fouling is where particles are deposited on the membrane surface during the filtration process, leading to a decline in membrane performance.¹⁶ There are two types of fouling, reversible and irreversible. Within the reversible category, there are a further two sub-categories; backwashable and non-backwashable. Membranes with backwashable fouling can undergo a physical washing process to remove foulants, whereas membranes with non-backwashable fouling must be subject to chemical cleaning. Reversible fouling occurs due to a concentration polarisation of particles at the membrane surface. Irreversible fouling is much more difficult to correct as it is the result of chemisorption and membrane pore plugging by particles in the filtrate. Some membranes can be restored with extensive chemical washing, but many have to be replaced.¹⁶ Regardless of the type of fouling, washing or membrane replacement involves filtration downtime, added complexity and incurs increases in operational costs.¹¹

The other significant limitation to membrane performance is the trade-off exhibited between flux and selectivity.¹⁷ Often with polymeric membranes, if you improve the water flux, the selectivity declines and vice versa. This trade-off was initially identified in gas separation membranes by L. M. Robeson, whereby an “upper-bound” of membrane performance was identified.¹⁸ This was then first applied to water purification membranes by G. M. Geise *et al.*¹⁹ This study observed that materials more permeable to water naturally tend to have a lower separation ability. However, it is suggested that the selectivity/permeability trade-off can be mitigated using smart design approaches and new

materials.^{20,21} These limitations in conventional polymer membranes mean developments in the technology is vital.

1.3. Composite and mixed matrix membranes

One of the methods of improving current polymer membranes is through the use of mixed matrix membranes and composite membranes. Composite membranes and mixed matrix membranes have overlapping qualities making their separate definitions difficult to distinguish and varied from paper to paper. For the purposes of this thesis, composite membranes are defined as membranes consisting of at least two different materials with the selective membrane material deposited as a thin layer upon a porous support (generally polymeric).²² A mixed matrix membrane is defined as the incorporation of nanomaterials in a continuous phase. The nanomaterial can either be porous (metal-organic frameworks, zeolites, graphene) or non-porous (silica, titanium oxides) and the continuous phase is polymeric.¹⁰ Figure 1.4 shows the difference between composite and mixed matrix membranes.

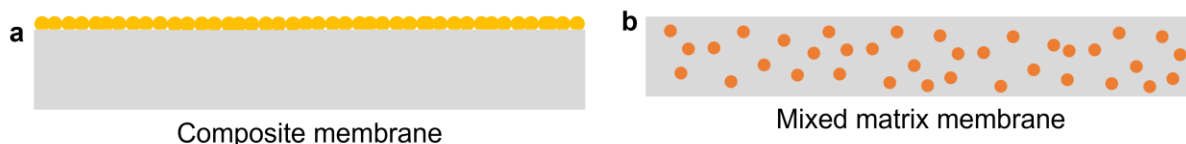


Figure 1.4. Schematic illustration of (a) a composite membrane compared to (b) a mixed matrix membrane using the definitions outlined in this thesis. Grey represents the polymeric support or continuous phase, and the yellow/orange represents the deposited/incorporated material.

Inorganic materials such as zeolites and ceramics are attractive separation materials due to their high chemical stability. Metal-organic frameworks (MOFs) have also gained considerable attention in separation applications because of their controllable porosity and good permeability.²³ However, when these inorganic materials are prepared as free-standing membranes, without any polymer support, while the performance can often be good, these membranes are typically highly fragile, rendering them incompatible for many applications.²⁴

In order to incorporate inorganic materials into membranes to form robust, flexible membranes with improved performance, composite and mixed matrix membrane techniques can be used.¹⁰ Inorganic fillers can be incorporated into polymeric membranes to combine the advantages of both materials; processing ease and mechanical strength of the polymers with improved permeability and selectivity afforded by the fillers.^{25,26} Adding inorganic fillers to the surface of a membrane support via deposition is a simple way of preparing composite membranes.¹⁰ Filler materials can be added to the polymer solution before the membrane is cast to incorporate the filler in the polymer matrix, forming a mixed matrix membrane.²⁷ Alternatively mixed matrix membranes can be prepared by including inorganic fillers in interfacial polymerisation processes. Fillers can be added to the support surface before the interfacial polymerisation takes place or they can be added to a monomer solution for direct inclusion in the polymerisation.^{28,29} Lastly, inorganic materials can be synthesised in-situ through solvothermal methods, whereby inorganic fillers are synthesised in-situ in the polymer during the formation of the membrane or on the surface of the membrane after formation.⁸

1.4. Metal-organic frameworks for water purification

One of the materials that can be used as a filler in composite and mixed matrix membranes is metal-organic frameworks. Metal-organic frameworks (MOFs) are part of a class of metal-organic materials, formed from the combination of metal ions and multitopic linkers.³⁰ The modular nature of MOFs allows for easy tuning of their structure, both pre- and post-synthetically.³¹ Additionally, it has been shown that the organic nature of MOF linkers can enhance interfacial interactions between the MOF and the polymer.³² These improved interactions reduce defects and void spaces in the mixed matrix and composite membranes, which in turn improves the membrane performance. Figure 1.5 depicts the difference between a membrane with poor interfacial interactions which lead to voids and defects (Figure 1.5a) and an ideal mixed matrix membrane with good interfacial interactions (Figure 1.5b).³³

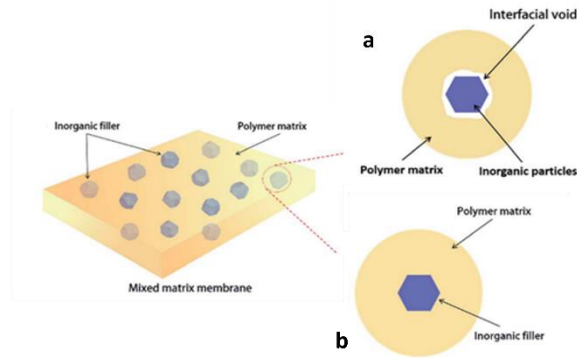


Figure 1.5. Schematic diagram of (a) a mixed matrix membrane with interfacial voids between the inorganic filler and polymer matrix, (b) an ideal mixed matrix membrane. Image adapted from reference 33.

Previously MOF membranes had been used for gas separation, however a 2014 paper by R. Zhang *et al.* was the first instance of water purification being the target application.³⁴ Zhang and co-workers successfully prepared ZIF-8/PSS membranes via an in-situ solvothermal method (ZIF-8 = $\text{Zn}(\text{mim})_2$ (Hmim=2-methylimidazole), PSS = polysodium 4-styrene-sulfonate). At an active layer thickness of 1 μm , the ZIF-8/PSS membrane gave a permeance of $26.5 \text{ L m}^{-2} \text{ h}^{-1} \text{ bar}^{-1}$ (units commonly referred to as LMHB) and a 98.6 % rejection of methyl blue. These results were not only an improvement on the pristine PSS membrane but also exceeded previously reported membranes (Figure 1.6).

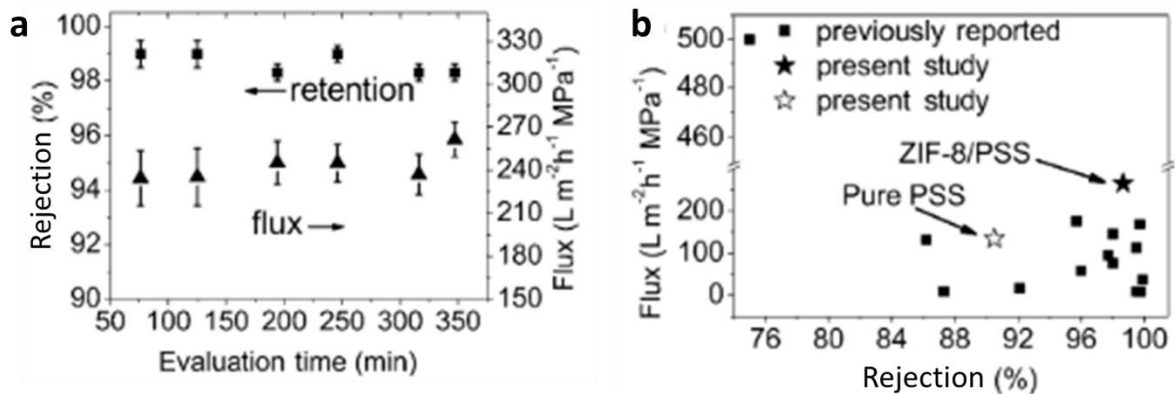


Figure 1.6. (a) Percentage rejection and flux (permeance) for ZIF-8/PSS membranes for the removal of methyl blue and (b) comparison of the dye removal performance of ZIF-8/PSS compared to previously reported membranes. Figure reproduced from reference 34.

Since this initial report, a search of the literature identified 67 further reports of MOF membranes used for water purification. Due to a large number of metal-organic materials being unstable in water, emphasis has been put on developing systems such as the UiO-, ZIF- and MIL- (Universitetet i Oslo,

zeolitic imidazolate framework- and Matériaux de l'Institut Lavoisier- respectively) families of MOFs that exhibit exceptional water stability.^{34–37} This is reflected in the fact that 43 of the 68 MOF membrane papers published included MOFs belonging to these families (Figure 1.7).

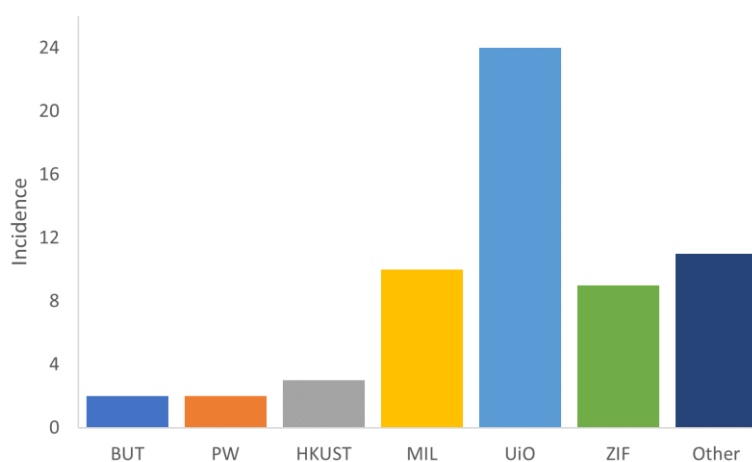


Figure 1.7. Bar chart showing the incidence of MOF systems used in MOF-membranes for water purification applications, accurate to 30.01.2022. Abbr.: BUT = Beijing University of Technology, PW = paddlewheel-based MOFs, HKUST = Hong Kong University of Science and Technology, MIL = Material Institut Lavoisier, UiO = Universitetet i Oslo, ZIF = Zeolitic Imidazolate Frameworks.

Examples of high performing membranes have been produced for each of the UiO-, ZIF- and MIL-families. UiO-66 has been investigated for water-purification applications in composite and mixed matrix membranes based on the good water stability mentioned above. When the UiO-66 framework was deposited onto membranes it displayed excellent salt rejection rates (up to 94.4%) and moderate water permeability (up to $3.31 \text{ L m}^{-2} \text{ h}^{-1} \text{ bar}^{-1}$ (LMHB)).^{38–40} It is thought that the water stability and chemical resistance of the UiO-66 MOF accounts for the fact that neither of these membranes showed any signs of degradation after prolonged filtration experiments.

ZIF-8 was used in membranes for water purification it showed a 162% flux increased from the pristine membrane while retaining 98% salt rejection.^{41,42} MIL-53(Al) was incorporated into a membrane, the water flux was high (above 45 LMHB) with nearly 100% dye rejection.²⁷

For the three examples described above, we can see that MOFs can be effective membranes for a range of different applications. However, it should be noted that the polymeric membrane support and additives used, the solutes rejected, and the method of testing are all different. The flux values

reported for each system are also in different forms (LMHB and percentage increase). These differences make direct comparisons of different MOF based composite and mixed matrix membranes challenging. However, these examples of MOF incorporation into membranes still serve as a small picture of the wider field. This shows that metal-organic materials have great potential for use in the improvement of water purification membrane technology.

1.5. 2D materials for water purification

In addition to three-dimensional (3D) filler materials such as zeolites, silica and MOFs, using two-dimensional (2D) materials for water purification membranes has been gaining interest in recent years.¹¹ The atomic thickness, flexibility, robustness and potential for functionalisation that 2D nanosheets possess make them stand out candidates for membrane technologies.⁴³ Currently, the most widely researched 2D material for membranes are graphene-based, including nanoporous graphene, graphene oxide and reduced graphene oxide.⁴³ The use of transition metal dichalcogenides, MXenes, 2D covalent organic frameworks, boron nitride, graphitic carbon nitride and metal-organic nanosheets have also been reported.¹¹

The first report of a graphene-based membrane for water purification was from a computational study carried out by D. Cohen-Tanugi and J. C. Grossman in 2012.⁴⁴ The authors used molecular dynamics to model the desalination potential of nanoporous graphene membranes. The study found that 100 % of NaCl ions could be rejected at a permeance of up to $100 \text{ L cm}^{-1} \text{ day}^{-1} \text{ MPa}^{-1}$. However, the issue with nanoporous graphene is the high cost and poor scalability of nanosheet production. A cheaper, easier to produce alternative is graphene oxide (GO).⁴⁵ Stacked GO membranes are more commonly used in water purification membranes due to the oxygen containing functional groups giving the nanosheets good hydrophilicity and excellent dispersion in water.⁴⁶ Additionally, GO nanosheets can be crosslinked due to the available hydroxyl and carboxyl groups on its surface. An example of this, GO nanosheets were covalently crosslinked by 1,3,5-benzenetricarbonyl trichloride (TMC) to give stable, well-defined interlayer nanochannel sizes for water to flow through.⁴⁷ The water flux was reported to

be up to 10 times higher than commercial examples and the composite membrane was able to reject Rhodamine-WT at 93 – 95 %.

One of the next most widely researched 2D materials are transition metal dichalcogenides (TMDs), with MoS₂ being the most popular material in this class.⁴⁸ TMDs are atomically thin materials consisting of layers of transition-metals (M) sandwiched between two layers of chalcogen atoms (X) to give the form MX₂.⁴⁹ The first reported MoS₂ membrane exhibited a water permeance 3 -5 times higher than previously reported GO membranes (245 LMHB), with 89 % rejection of Evans blue dyes and no degradation.⁵⁰ Another family of 2D materials that have attracted some attention in the water purification literature are MXenes. MXenes are 2D materials consisting of transition metal carbides, nitrides or carbonitrides.⁵¹ A robust and flexible Mxene membrane made from Ti₃C₂T_x displayed improved separation of cations with high charge compared to GO with a water flux of 37.4 LMHB, which the authors quote as “rapid”.⁵²

While all of these 2D materials have been shown to perform well in water purification membranes, the small amount of tunability and change in functionality afforded to these materials limits their potential.

1.6. Membrane characterisation and tests

There are a number of characterisation techniques that are required to get a full picture of mixed matrix and composite membranes. The characterisation can be broadly split into two categories, chemical composition, and surface properties. Chemical composition can be characterised by Fourier transform infrared spectroscopy (FTIR), Raman spectroscopy, energy-dispersive X-ray spectroscopy (EDX) and X-ray photoelectron spectroscopy (XPS). These techniques allow the identification of different chemical bonds, helping to understand the incorporation and cross-linking of MMM fillers. Additionally, powder X-ray diffraction (PXRD) can be used when crystalline compounds, such as MOFs are incorporated into the membrane to show that the crystalline nature of these materials is still present.^{53,54} The other important aspect of these membranes is the surface properties, these can be

characterised by scanning electron microscopy (SEM) or field emission SEM (FESEM), transmission electron microscopy (TEM), atomic force microscopy (AFM) and contact angle measurements.⁵³ These surface analysis techniques enable the roughness and hydrophilicity of membrane to be measured, as well as being able to look at the morphology of the surfaces and any MMM fillers either incorporated within the membrane or deposited on the surface.

Once the membranes have been prepared, their filtration performance must be tested. There are a few common set-ups used to test membrane performance; dead-end cell, cross flow, and forward osmosis (FO). Dead-end cell filtration is the most common lab scale filtration test. Water is directed perpendicular to the membrane surface, and the applied pressure forces the water through the membrane.⁵⁵ If the concentration of pollutants in the feed solution is too high, pollutant material can accumulate on the membrane surface. This affect is called fouling, and results in a pressure drop across the membrane which causes a reduction in permeance. While dead-end cell filtration is not commonly used in industrial settings, it allows researchers to carry out quick tests to evaluate whether membranes have the potential to be used in large scale filtration set-ups.⁵⁶ Cross-flow filtration is often a larger scale operation than the dead-end cell set-up. In a cross-flow set-up, water flows parallel to the membrane surface. This creates a shear force that reduces the build-up of pollutant materials on the surface, therefore reducing the effect of fouling.⁵⁵ FO is a similar process to cross-flow, however rather than the applied pressure driving the separation, the osmotic pressure gradient drives the filtration.⁵⁷ Water passes from the feed solution to the draw solution with high water flux, low fouling and low energy cost.

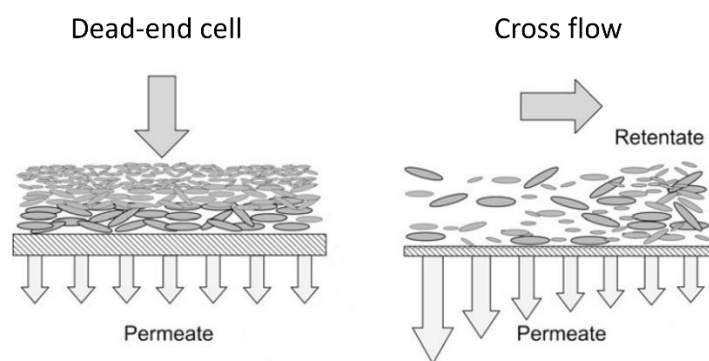


Figure 1.8. Schematic comparing dead-end cell and cross-flow filtration types. Figure adapted from reference 58.

Molecular weight cut-off (MWCO) is a value used to determine whether a membrane is appropriate for a specific application. The MWCO of a membrane is the minimum molecular weight of a solute (in Daltons), that is 90% retained by the membrane. Currently there isn't a universal standard method for MWCO determination, with methods in the literature ranging from polystyrene glycols (PEGs) to heavy metals and nanoparticles.⁵⁹

1.7. Metal-organic nanosheets

Combining the unique properties of 2D and metal-organic materials gives rise to a whole new distinct class of materials. Metal-organic framework nanosheets, MONs, have the advantages of molecular thickness, high surface-to-volume ratio alongside molecular design and tunability.⁶⁰ MONs can be defined as free-standing, two-dimensional materials, approaching monolayer thickness, formed by the coordination of organic ligands with metal ions or clusters.⁶¹ MONs follow the general structure of other layered materials, strong connectivity within a plane and weak interlayer interactions in the bulk material which allows the separation of individual layers. With MONs, the strong interactions within a plane are usually achieved by inorganic connectivity or the bridging of isolated metal ions or clusters with organic ligands. The combination of organic ligands and metal nodes gives MONs an advantage over simple inorganic nanosheets like graphene as they allow the chemical and physical properties of MONs to be systematically tuned.⁶² The interactions in the 3rd dimension are often a combination of weaker dispersive, hydrogen bonding and ionic interactions.⁶³

Since the 1st example of nanoscale MOFs in 2008,⁶⁴ examples of MONs in the literature have been presented under a multitude of names, including metal-organic framework nanosheets (MOF nanosheets),⁶⁵ 2D metal-organic frameworks (2D MOF),⁶⁶ coordination nanosheets (CONASH),⁶⁷ metal-organic layers (MOLs).⁶⁸ Throughout this report the terminology MON or metal-organic nanosheet will be used.

1.7.1. Synthesis and exfoliation

MON synthesis can be broadly separated into two classifications; “bottom-up” and “top-down”. The bottom-up synthetic approach starts with reagents, directly synthesising nanosheets through controlled crystallisation methods. Top-down synthesis involves using bulk layered materials and “exfoliating” apart the layers to give discrete nanosheets. Figure 1.9 illustrates the range of different synthetic methods employed within the bottom-up and top-down categories.

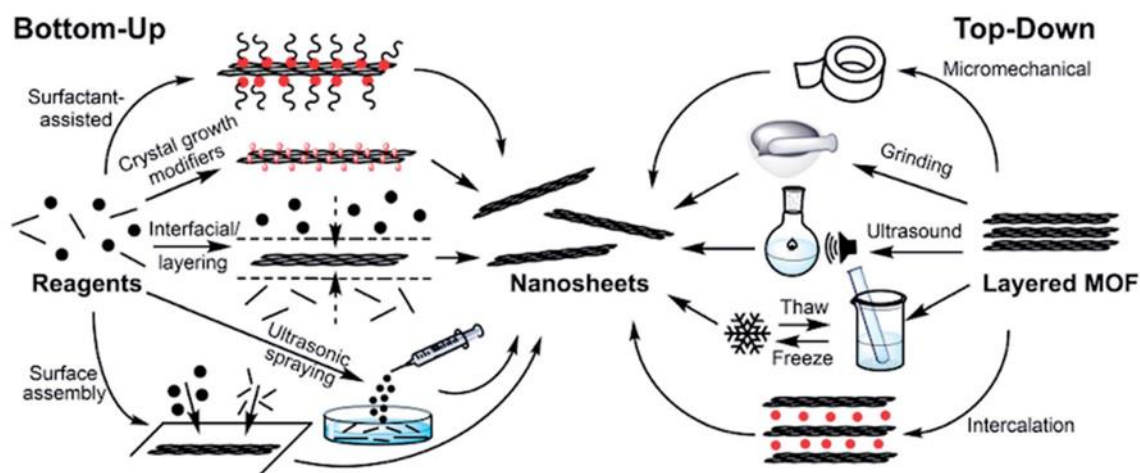


Figure 1.9. Schematic depicting different techniques of metal-organic nanosheet synthesis. Image reproduced from reference 63.

1.7.2. Bottom-up synthesis

Starting with the organic linkers and metal ions, bottom-up methods seek to form the nanosheet directly from the constituent parts. This can take place in one of two ways; selectively blocking the crystal growth in one direction or promote growth in the 2D at the expense of growth in the 3rd dimension. This allows nanosheets to form without the need for additional synthesis steps. Choosing

ligands and secondary building units with a predisposition to crystallise in two-dimensions is a useful design feature in these crystal structures.⁶³ Using bottom-up approaches can also allow nanosheets to be prepared from non-layer structured MOF analogues, further expanding the potential of these materials.⁶⁹ Figure 1.9 shows the different bottom-up approaches that have been reported in the literature.

The surfactant assisted method works in two different ways in the preparation of nanosheets. In one method, shown by the use of polyvinylpyrrolidone (PVP) in Figure 1.10a, surfactant molecules selectively cap the surface of the MOF, inhibiting growth in one direction, leading to the formation of anisotropic nanosheets.⁷⁰ Alternatively, as seen in the synthesis of MIL-53 nanosheets, the cetyltrimethyl ammonium bromide (CTAB) surfactant preassembles Al^{3+} ions between the surfactant lamellae within which the nanosheet crystals grow, causing MIL-53 to preferentially form in one plane (Figure 1.10b).⁷¹

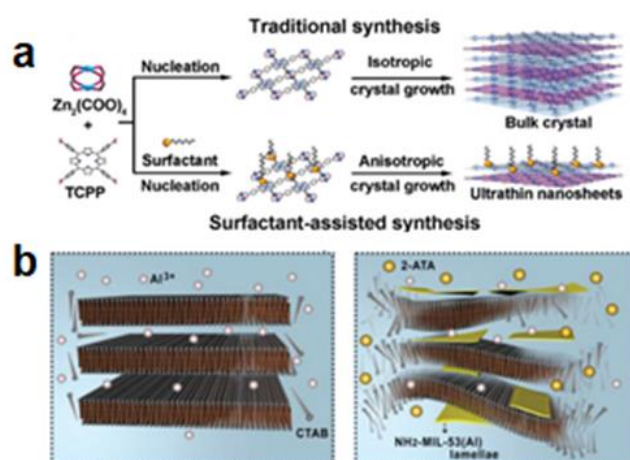


Figure 1.10. (a) Scheme of traditional synthesis and surfactant-assisted synthesis of Zn-TCPP MOFs. Image reproduced from reference. (b) Example of surfactant-assisted synthesis of MIL-53 nanosheets. Reproduced from reference 71.

Adding a modulator with competing functional groups as the ligands, that coordinates to the metal ions is another method to preferentially form nanosheets over the 3D structure. An example of this modulator method is selecting monotopic ligands that coordinate in specific crystal planes can allow the formation 2D nanosheets from MOF structures that would have otherwise been 3 dimensional.⁷²

An example of this is UiO-67 nanosheet synthesis, in which formic acid is used as a modulating agent. Formic acid acts as a monodentate ligand, binding to the Hf_6 cluster, preventing the formation of the bridged double cluster normally seen in UiO- MOFs.⁷³ This leads to defects in the MOF structure which can be exploited to form nanosheets through grinding or sonication.⁷⁴ In the case of UiO-67, these defects also lead to a stacked structure if the synthesised MOF is left in ambient conditions. Figure 1.11 shows the structural changes UiO-67 undergoes with the addition of a formic acid as a modulating agent.

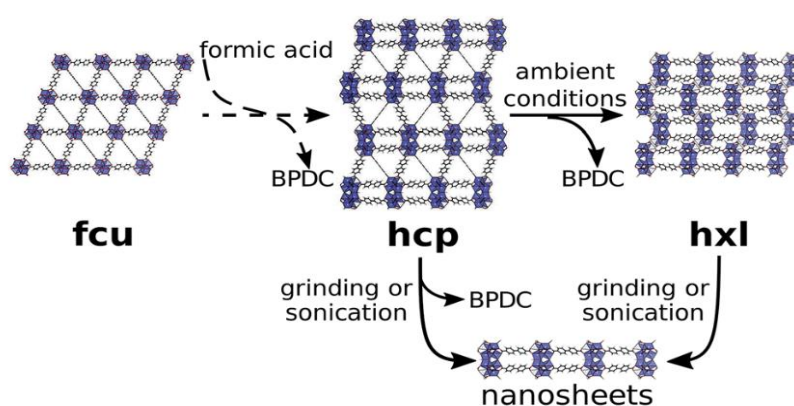


Figure 1.11. Modulated synthesis of UiO-67 nanosheets. Image reproduced from reference 74.

In interfacial synthesis, the reaction between organic linkers and the metal nodes happens at an interface. There are 3 different types of interfaces that can be used in MON synthesis; liquid/air, liquid/liquid, and liquid/solid.⁶⁹ In liquid/air synthesis, a very small amount of immiscible solvent is added onto the surface of another bulk solvent, the deposited solvent then evaporates creating the liquid/air interface. In this scenario one solvent would contain the ligand and one would contain the metal ions. For example, R. Makiura *et al.* deposited 5,10,15,20-tetrakis(4-carboxyphenyl)porphyrinato-cobalt(ii) (TCPP(Co)) dissolved in a mixture of pyridine, chloroform and methanol onto an aqueous solution of $CuCl_2 \cdot H_2O$ to form monolayer nanosheets.⁷⁵ The reaction takes place at the surface of the bulk solvent, allowing control over the nucleation and growth kinetics of the MONs.⁷⁵

Another method of using an interface to control crystal growth is using a three-layer technique. Layering two different solvents of different densities, with a buffer zone in the middle, slows the diffusion and growth rate of the MONs. This technique was successfully employed by Rodenas *et al.* when preparing a CuBDC MONs.⁷⁶ Figure 1.12 shows how the Cu²⁺ and BDC solutions were layered to form ultrathin CuBDC MONs.

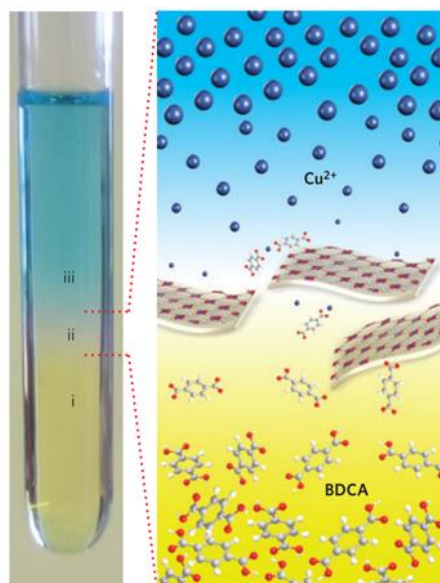


Figure 1.12. Scheme showing the synthesis of CuBDC MONs via a layering method. Image reproduced from reference 76.

1.7.3. Top-down synthesis

Top-down synthetic methods almost exclusively rely on the separation of layers from pre-ordered layered 2D MOF structures. Weak interactions, such as van der Waals forces, π - π stacking and hydrogen bonding stack the layers within these MOF structures. These layers can then easily be separated through various exfoliation methods. When graphene was originally synthesised, the “Scotch tape” method was used, this method can produce graphene nanosheets down to 2 nm, and has been used to exfoliate benzimidazole based MONs down to thicknesses of 6 nm.⁷⁷ This method however, is both impractical, as it requires very large crystals to start the exfoliation process and has very limited scalability.⁷⁸ Since this first graphene synthesis, a multitude of other top-down synthesis methods have been developed, depicted in Figure 1.9.

The most common of these methods in the literature is liquid exfoliation by sonication. The energy input from the ultrasonicator is enough to overcome the weak inter-layer interactions, allowing solvent molecules to penetrate the structure and force layers apart into discrete nanosheets.⁷¹ Sonication causes bonds within layers to break also, leading to fragmentation and broader particle size distribution of MONs when compared to bottom-up approaches.⁶³ Solvent choice plays an important role in sonication of MOFs and can greatly impact exfoliation rates.⁶⁹ Using a mixture of solvents is believed to improve exfoliation by sonication. One solvent for highly exfoliating the layered MOFs and the other for stabilising the exfoliated MONs.⁷⁹ An example of the use of a mixed solvent system can be seen in the exfoliation of ZIF-7. A 50:50 mixture of methanol: n-propanol is used during the sonication of ZIF-7, yielding nanosheets of a thickness in agreement with the theoretical thickness of a single layer.⁸⁰

Intercalation is a method whereby molecular/ionic species are introduced between layers in MOF structures to increase the interlayer distance and lead to easy exfoliation to produce MONs.⁸¹ Wang *et al.* successfully used lithium-ions to intercalate various frameworks, with the suggestion that the hydration of these Li-ions push the MOF layers apart far enough that the effect from the interlayer interactions becomes negligible, subsequently allowing complete exfoliation by sonication.⁸² Freeze-thaw is another method where layers are forced apart by shear force. The volumetric change between the liquid and solid states of the chosen solvent results in exfoliation of the layered MOF into free standing nanosheets.⁸³

Layered MOFs can be mechanically exfoliated through grinding or ball milling. Due to the nature of these mechanical methods a wide range of thicknesses and lateral sized particles are produced.⁷³ Wet-ball-milling is another variation on this technique, where it is suggested that due to the ball-milling process, the solvent penetrates the voids between the layers in the MOF, aiding exfoliation.⁷⁹

While top-down methods are relatively simple, and efficiently produce phase pure, highly crystalline metal-organic nanosheets, the yield and rate of production is not scalable. Conversely, bottom-up

approaches are often one-pot methods, that require minimal synthesis steps. Bottom-up methods are not always as efficient in producing highly crystalline, phase pure samples, they are far more scalable, giving a tangible solution to practical applications.

1.7.4. MON Characterisation

Just as with MOFs, the molecular structure and composition of MONs can be characterised through a variety of solid-state characterisation techniques. The primary method of characterisation for MOFs is single crystal X-ray diffraction. The diffraction pattern from the crystalline solid allows determination of crystal structure.⁸⁴ However this technique requires crystals of sufficient size and quality for the measurement, the growth of which is not possible with metal-organic nanosheets. Therefore, powder X-ray diffraction (PXRD) is used to evaluate the overall phase of the MONs and compare this with the pre-determined structure of the parent MOF. As the microcrystalline powder used in this method is randomly oriented, the resultant pattern consists of diffraction intensities as a function of the diffraction angle (2θ).⁸⁵ While PXRD is mostly used for bulk phase evaluation, high-resolution data can allow for structure determination without the growth of large single crystals.⁸⁶ In MON PXRD patterns there is often a systematic loss of peaks and peak broadening which is a result of the reduced dimensions of the nanosheet and the preferred orientation of the microcrystals in the powder sample.⁷⁶

Nuclear magnetic resonance (NMR) spectroscopy is also used to accompany X-ray diffraction methods; the solid-state structure of MONs can be determined by solid-state NMR. Additionally, MONs can often be easily “digested” by aqueous HCl, allowing the characterisation of the ligands in the solution state by NMR spectroscopy and mass spectrometry. These techniques can be instrumental in the analysis of post-synthetically modified systems, where ligands are altered after the MON has been synthesised. Fourier-transform infra-red (FTIR) spectroscopy, thermogravimetric analysis (TGA), elemental analysis are also commonly employed techniques used to corroborate the structure identified by PXRD and to confirm composition and purity of metal-organic nanosheets.

When analysing nanosheets, in order to get a full picture, the structure at a nanoscopic level must be considered. Microscopy is a useful tool in the characterisation of the nanoscopic size and morphology of produced nanosheets. Atomic force microscopy (AFM) is a key technique in MON characterisation being the best way to accurately measure the height of nanosheets in your sample. Comparing the height measured by AFM to the calculated layer size from crystal structures allows for the determination of the number of layers present in the nanosheets.⁸⁷ Scanning electron microscopy (SEM) and transmission electron microscopy (TEM) are used for visualising the bulk of the particulates. Rough particle shape, size and local features can also be seen using these microscopes. Additionally, electron diffraction can be used in conjunction with TEM to probe the nanosheet structure.

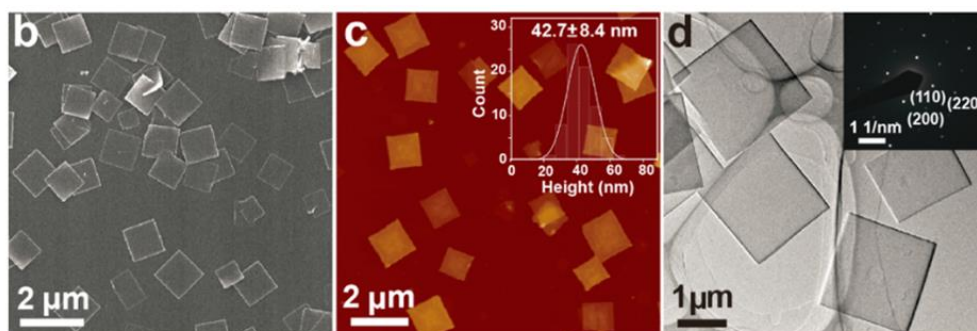


Figure 1.13. Examples of images of MONs produced using microscopy techniques. b) SEM image, c) AFM image, inset: statistical analysis of the thickness of nanosheets, d) TEM image, inset: selected area electron diffraction of a nanosheet. Image reproduced from reference 88.

1.7.5. Applications

As already discussed, MONs have a unique combination of properties stemming from their 2D structure, and the ability to design this structure through the choice of metal nodes and ligands. This opens MONs up as solutions to a wide range of real-world applications. Figure 1.14 shows the main areas of application for MONs and the MON features that lend these materials to said applications.

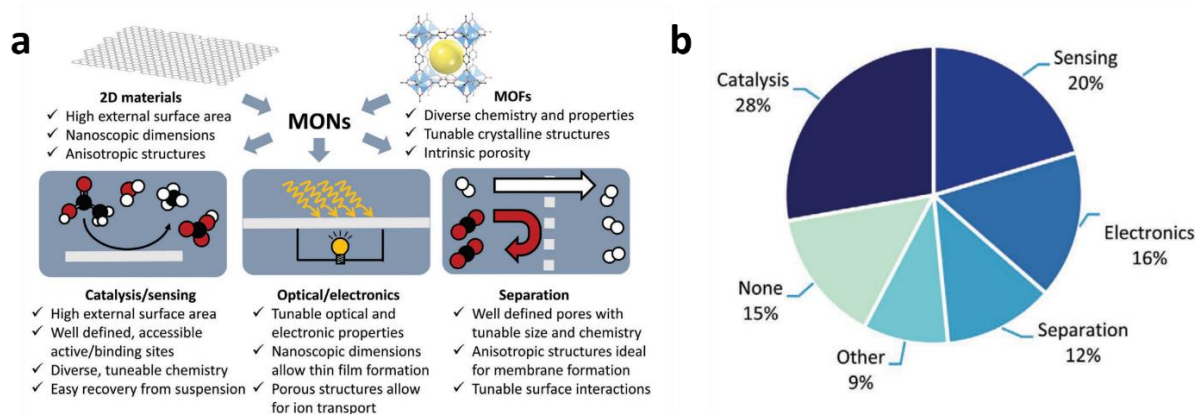


Figure 1.14. (a) Schematic showing the MON features applicable for the main categories of application and (b) pie chart showing percentage of MON articles categorized based on application. Figure adapted from reference 62.

Not only do the highly accessible active sites on a MON surface improve their catalysis ability but the ultrathin thickness means there is no diffusion rate through the catalyst, improving it further.^{89,90} As an example, L. Cao *et al.* reported the use of Hf-TPY-BTB MONs (BTB = benzene-1,3,5-tribenzoate, TPY = 4'- (4-benzoate)-(2,2',2''-terpyridine)-5,5''-dicarboxylate) as hydrosilylation catalysts.⁹¹ Zero catalytic activity in the bulk material compared to 100 % conversion with the MONs was observed. The authors attribute this to “formidable diffusion resistance” in the bulk material.⁹¹ Additionally the tunable nature of MONs allows multiple catalytic reactions to occur in tandem.^{92,93}

The highly accessible active sites on MONs can also be exploited for sensing applications. The tunability of these nanosheets allows researchers to design materials for the sensing of specific molecules. For example, Cu-TCPP nanosheets were used by Q. Yang *et al.* as a fluorescence aptasensor for the detection of antibiotics.⁹⁴ The nanosheets outperformed graphene oxide by 7.5-fold, proving the MONs can sense with high sensitivity.

It is hypothesised that the high transparency, tunable energy band structure, and good solution processability makes metal-organic nanosheets good candidates for wide range of electronic applications.⁹⁵ In the first report of MONs used in photovoltaic devices, tellurophene based MONs were blended with a polymer and included in a device as a buffer layer.⁹⁵ Alone, the polymer decreased the solar cell work function, however upon the addition of MONs, the work function increased. The porous structure of the MONs enhanced charge transfer, improving the device

performance. Additionally, the space between layers is thought to improve the storage ability of supercapacitors.⁹⁶

One of the largest areas of application explored for MOFs is molecular separation. The porous nature and tunability of these materials means you can tailor your design to selectively trap some molecules while allowing others to pass through. This can be done by size exclusion mechanisms or through frameworks selectively interacting with certain molecules. As MONs possess the same tunable quality as their 3D analogues, tailoring the design of MONs to selectively trap or reject certain molecules can also be applied. Their ultrathin structure allows for excellent membrane flexibility,⁹⁷ it also enables improved flux compared to the bulkier crystals,⁷⁶ even at lower loadings.⁹⁸ There are two main applications of MON-membranes; water purification (see section 1.8) and gas separation. The first example of MONs used in gas separation membranes was reported by Y. Peng *et al.* in 2014.⁹⁹ Zn₂(bim)₄ nanosheets were deposited onto α -Al₂O₃ support disks via a hot drop method before being tested for H₂ and CO₂ separation. The membranes exceeded the performance of all previously reported molecular sieve membranes and showed exceptional thermal and hydrothermal stability.

1.8. MONs for water purification

At the beginning of this project in October 2018, there was a single literature example of MON-membranes for water purification, since then nine further papers have been published. This section explores these ten MON-membrane papers, and critically compares their preparation and performance.

1.8.1. Examples of MON-membranes in the literature

Ang and Hong pioneered the field MON-membranes for water purification using 2D Zn- tetra(4-carboxyphenyl)porphyrin(Fe) (Zn-TCPP(Fe)) deposited onto nylon supports along with polycationic polymer additives (Figure 1.15).¹⁰⁰ The paper explores the use of Co-TCPP(Fe) and Cu-TCPP(Fe) nanosheets as well as Zn-TCPP(Fe), concluding that Zn-TCPP(Fe) gives the best performance. Ang and Hong then go on to state that the separation performance of the MON-membrane is improved with

the addition of the polycations polyethylenimine (PEI) and poly(diallyldimethylammonium chloride) (PDDA). The polycations are stated to cross-link the edges of the nanosheets, forming a more robust, continuous selective layer on the nylon support. Ang and Hong prove the cross-linking behaviour with the presence of an amine functional group and quaternary nitrogen species in the XPS spectra of PEI/Zn-TCP(Fe) and PDDA/Zn-TCP(Fe) respectively. The addition of polycations improves the water permeance by up to 2 times (2120 LMHB to 4243 LMHB), gives rejection of small dye molecules of over 90% and demonstrates improved salt rejection at 20 – 40%. The paper does not provide evidence to explain the vast improvements of these parameters; however, the authors reason that the polycations regulate the nanosheets, leading to a crack-free, well-aligned selective layer which could account for the superior performance of the polycation cross-linked Zn-TCP(Fe) membranes.

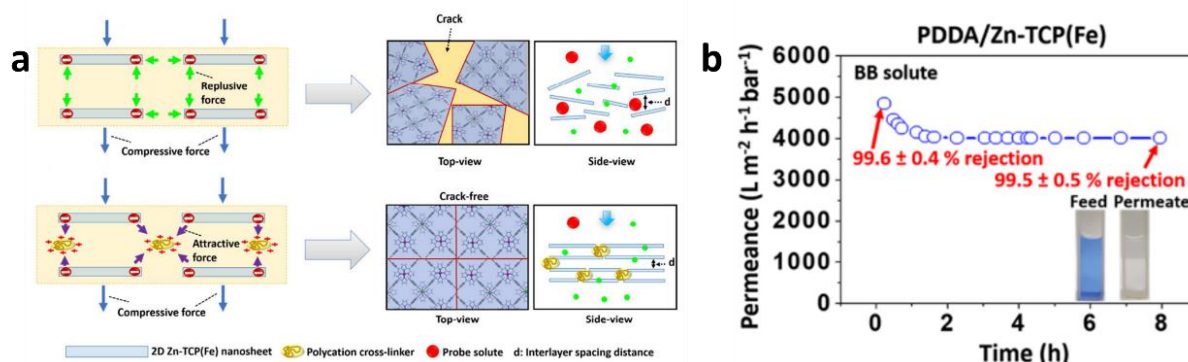


Figure 1.15. (a) Schematic illustrating the cross-linking behaviour of PEI/PDDA on the Zn-TCP(Fe) nanosheets and (b) the water purification performance of PDDA/Zn-TCP(Fe) membranes tested with brilliant blue G dye. Figure reproduced from reference 100.

Since this initial publication, four of the nine following MON-membrane papers use porphyrin-based MONs in their membranes. Firstly, in 2020, *Jia et al.* deposited Zn-TCP(Fe) MONs, alongside two stabilising agents (poly(N-vinyl caprolactam) (PVCL) and polyvinylpyrrolidone (PVP)) on a nylon support to create a thermoresponsive membrane.¹⁰¹ The thermoresponsive nature of the membrane comes from the PVCL inclusion, whereby the polymer chains reversibly collapse upon heating (see Figure 1.16), drastically affecting the rejection and permeance performance of the membrane. The PVP is simply used to provide interfacial stability. At ambient temperatures, the permeance is 959 LMHB and the rejection of the dye brilliant green is 99.0%. When the temperature is cycled between

20 °C and 60 °C the permeance switches between 885 LMHB and 1532 LMHB, while the rejection of neutral red reduces from 99.0% to 1.3% at higher temperature. This study proves the ability to engineer responsive membranes for controlled separation applications.

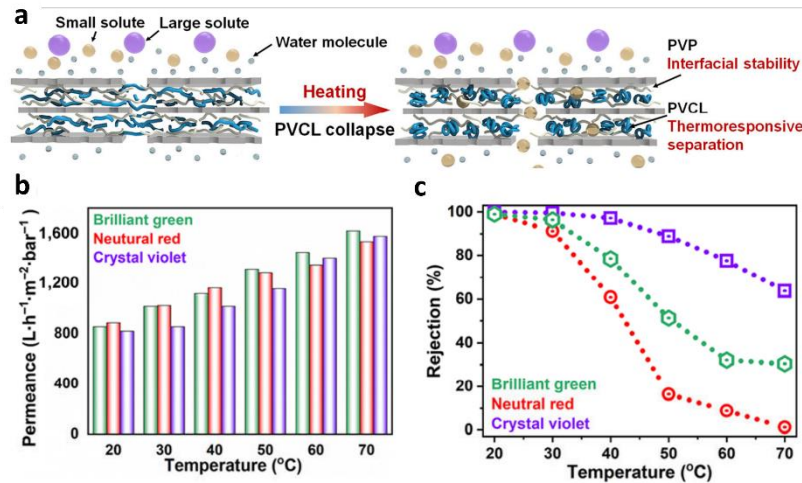


Figure 1.16. (a) Schematic illustration of the thermoresponsive mechanism of the Zn-TCPP nanosheet membrane, (b) Temperature-dependent permeance and (c) rejection percentage for different dye solutions. Figure reproduced from reference 101.

Also in 2020 were papers from *Jian et al* and *Wen et al.*^{102,103} The former synthesised Al-TCPP nanosheets that were subsequently deposited on anodic aluminium oxide supports (100 nm pores) using a vacuum filtration method. As can be seen in Figure 1.17, they reported permeation of 2.2 mol m⁻² h⁻¹ bar⁻¹, with nearly 100% rejection of all investigated ions (Na⁺, K⁺, Mg²⁺, Ca²⁺, Al³⁺, Co²⁺).¹⁰² As this study uses diffusion cells to test the performance of the membranes, it is not very comparable to the other MON-membranes published and will be excluded from further comparison.

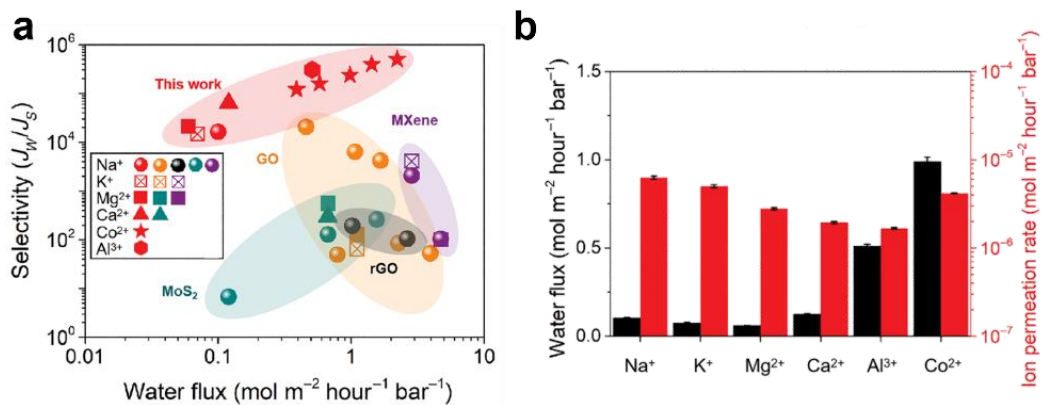


Figure 1.17. (a) Water flux and corresponding ion permeation rate using different draw solutions (0.5 M) through a 100 nm thick Al-TCPP membrane, (b) Comparison of results published in the paper to other 2D laminar membranes. Figure reproduced from reference 102.

Wen *et al.* synthesised a thin-film composite (TFC) membrane using Zn-TCPP MONs as the selective layer.¹⁰³ In this case the MONs were deposited onto a polyethersulfone (PES) support layer following the synthesis of a polyamide top layer via interfacial polymerisation (Figure 1.18). The addition of the Zn-TCPP nanosheets nearly triples the permeance of the membrane to 4.82 ± 0.55 LMHB. The membrane also reaches rejection of $97.4 \pm 0.6\%$ for the removal of NaCl. Unlike the previous two Zn-TCPP papers that have nanofiltration performances, these membranes show reverse osmosis (RO) behaviour. Therefore, while the permeance appears low in comparison to the other examples, it is actually in the expected region for RO membranes. This paper carried out layer thickness study, observing that the optimum thickness of Zn-TCPP MONs is 66 nm. The improvement of permeance is attributed to a number of factors including decreased intrinsic thickness and enhanced effective filtration surface area provided by the MONs. The decrease in permeance at 166 nm is not discussed, however this could be due to the overall membrane thickness increase overpowering the aforementioned affects.

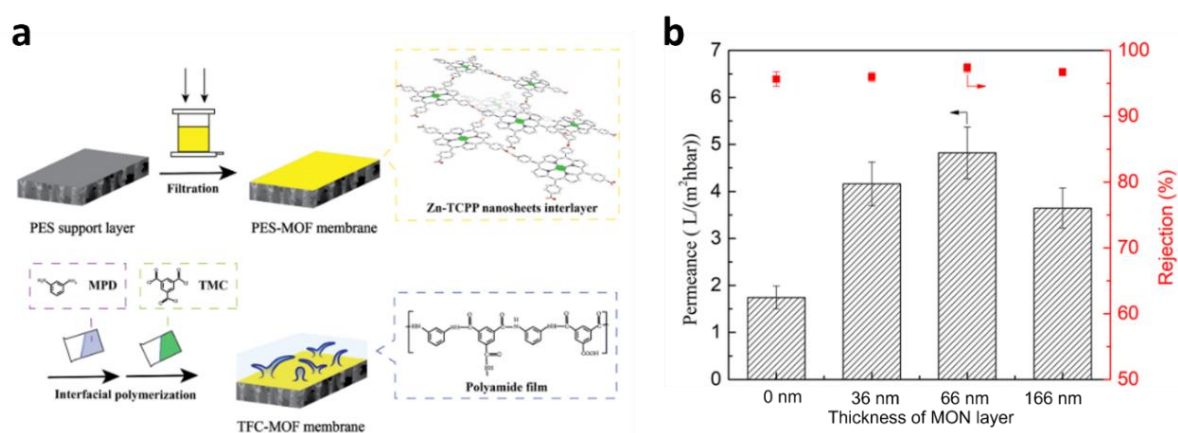


Figure 1.18. (a) schematic illustration of the fabrication process of the Zn-TCPP membrane, and (b) separation performance based on MON layer thickness. Figure reproduced from reference 103.

The final porphyrin-based MON-membrane paper published at the time of submission used M-TCPP (M = Zn, Cu, Co, Ni) in a P84 (polyimide) matrix for organic solvent nanofiltration (OSN).¹⁰⁴ Yao *et al.* dope a solution of the P84 polymer with M-TCPP before casting the membranes using a casting knife method. Zn-TCPP showed the greatest improvement of membrane permeance (from 0.7 LMHB to 1.8 LMHB) with only a slight decrease in rejection (Figure 1.19). M-TCPP were also ultrasonically treated,

yielding a nanosheet dispersion. Treated Cu-TCPP (*t*-CuTCPP) showed further improvements in permeance (2.81 LMHB) while keeping rejection above 90%.

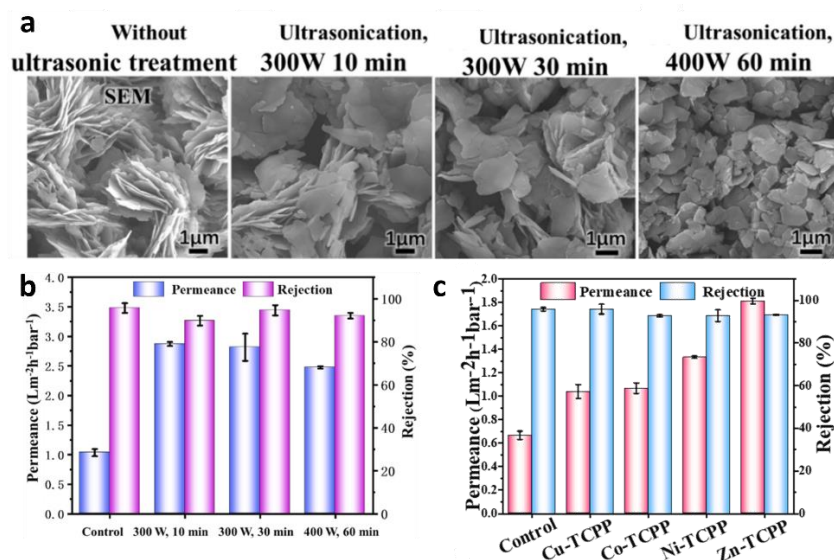


Figure 1.19. SEM images of Cu-TCPP nanosheets after varying amounts of ultrasonic treatments, organic solvent nanofiltration performance of membranes made using (b) Cu-TCPP with varying ultrasonic treatments and (c) different MON systems. Image reproduced from reference 104.

Another frequently used MON for water purification membranes is CuBDC. First in 2019 *R. Dai et al.* developed thin-film nanocomposites containing CuBDC nanosheets for forward osmosis applications.¹⁰⁵ Interfacial polymerisation was used to incorporate the CuBDC nanosheets into a polyamide (PA) active layer. After doing high-resolution XPS on the CuBDC-PA membranes, the N-C=O* to O*-C=O ratio decrease, compared to the pristine membrane, is ascribed to the presence of the carboxylic acid groups from the CuBDC in the membranes. Authors even speculate that the nanosheets could have cross-linked to the polyamide via the formation of amide bonds during interfacial polymerisation, however there is no concrete evidence to confirm this. The CuBDC-PA membranes performed at around 50% higher water flux than a pristine sample, and a reduction in the solute flux, suggesting an improvement in selectivity. The CuBDC-PA membranes show a slower decline in water flux than the pristine membrane, indicating some anti-fouling behaviour. This is expected to arise from the hydrophilic surface of the CuBDC-PA membrane, trapping a thin film of water against the membrane surface which serves as a barrier against foulant adhesion.

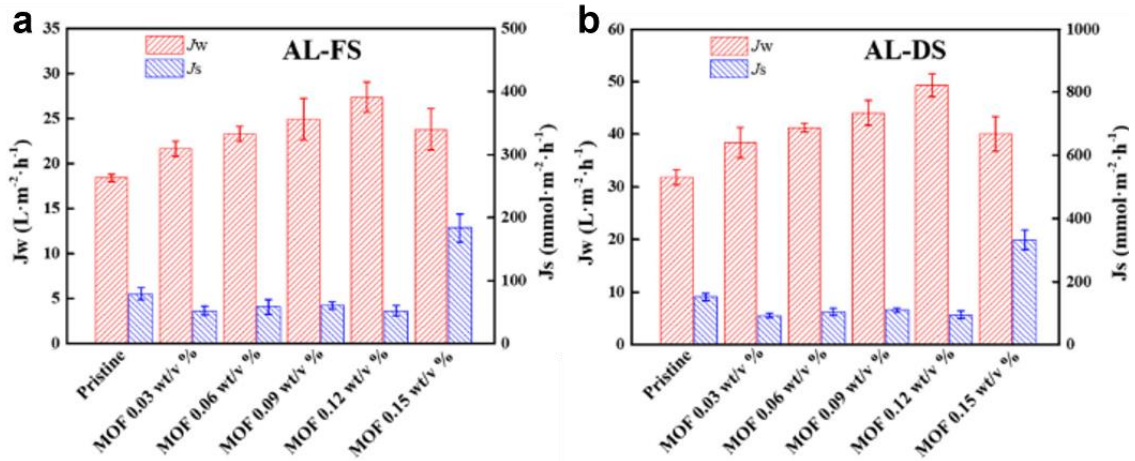


Figure 1.20. Osmotic water flux (J_w) and reverse solute flux (J_s) under (a) AL-FS mode and (b) AL-DS mode. Image reproduced from reference 105.

In 2021, X. Yin *et al.* reported a continuous coating of 2D CuBDC on hyaluronic acid modified bacterial cellulose as a way of removing nitrobenzene from water.¹⁰⁶ The bacterial cellulose membrane is impregnated with hyaluronic acid to provide surface carboxyl groups, this is then immersed in the precursor solution for CuBDC, and the nanosheets are synthesised in situ, to form a continuous thin film approx. 20 nm in thickness. The study shows that using this method, compared to an unmodified cellulose surface containing hydroxyl groups, or a surface containing amino groups, enables the synthesis of CuBDC nanosheets that are parallel to the surface. Both the water permeance (160.5 LMHB) and rejection of nitrobenzene (68.6%) are reported as higher than state-of-the-art polymeric membranes and any previous studies (Figure 1.21b).

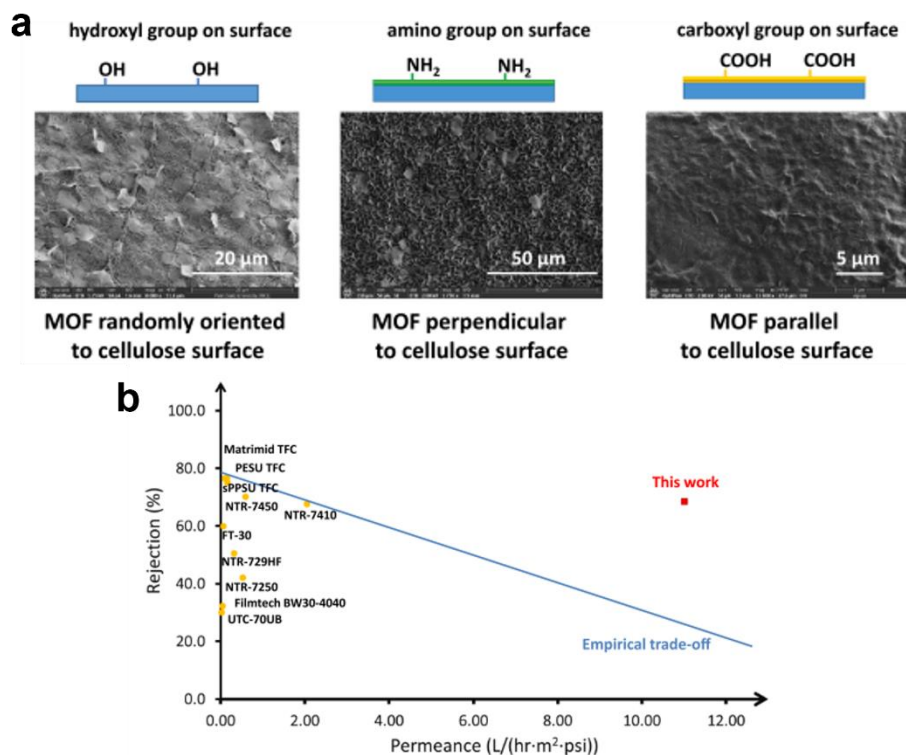


Figure 1.21. (a) SEM images showing the effect of surface modification on MON orientation, (b) comparison of work reported in this paper to previous studies. Image reproduced from reference 106.

Zeolitic imidazolate frameworks (ZIFs) have attracted a lot of interest in the past years due to their high stability and easy synthesis.¹⁰⁷ *Y. Peng et al.* reported the use of the layered ZIF – $Zn_2(Bim)_3(OH)(H_2O)$, where Bim = benzimidazole, grafted to poly(amidoamine) (PAMAM) nanoparticles as crosslinkers then deposited onto porous $\alpha-Al_2O_3$ substrates.¹⁰⁸ A blue-shift in bands assigned to the PAMAM amino group in the Fourier transform infrared (FTIR) spectra of the ZIF nanosheet after the grafting process is used to confirm the success of the cross-linking process. This is corroborated by increases in peak intensity when PAMAM is incorporated with the nanosheets in x-ray photoelectron spectroscopy (XPS) results. *Peng et al.* report that their PAMAM grafted ZIF nanosheets has two different morphologies – one rough side (side A) and one smooth side (side B), something that is not seen in the pristine ZIF nanosheets. The authors attribute this to the PAMAM grafting preferentially to one side of the nanosheets (side A). It is thought that side A has a more hydrophilic nature, and side B displays a steric hinderance and hydrophobic nature due to the orientation of the Bim ligands in the $Zn_2(Bim)_3(OH)(H_2O)$ nanosheets. This PAMAM-ZIF nanosheet

membrane was tested for rejection of Evans blue dye. It was found that with increasing the amount of nanosheet suspension returned improved rejection (17% to 99.4%) but reduced the permeance (421 LMHB to 67 LMHB) – unfortunately the authors did not give an optimised system whereby the rejection was improved without sacrificing the permeance. Additionally, the study shows the importance of a compaction step in some membrane fabrications. A pure water feed at 5 bar was passed through the PAMAM-ZIF membrane, compacting the nanosheets onto the surface of the support to give a well-distributed and more compact coverage of PAMAM-ZIF nanosheets on the support.

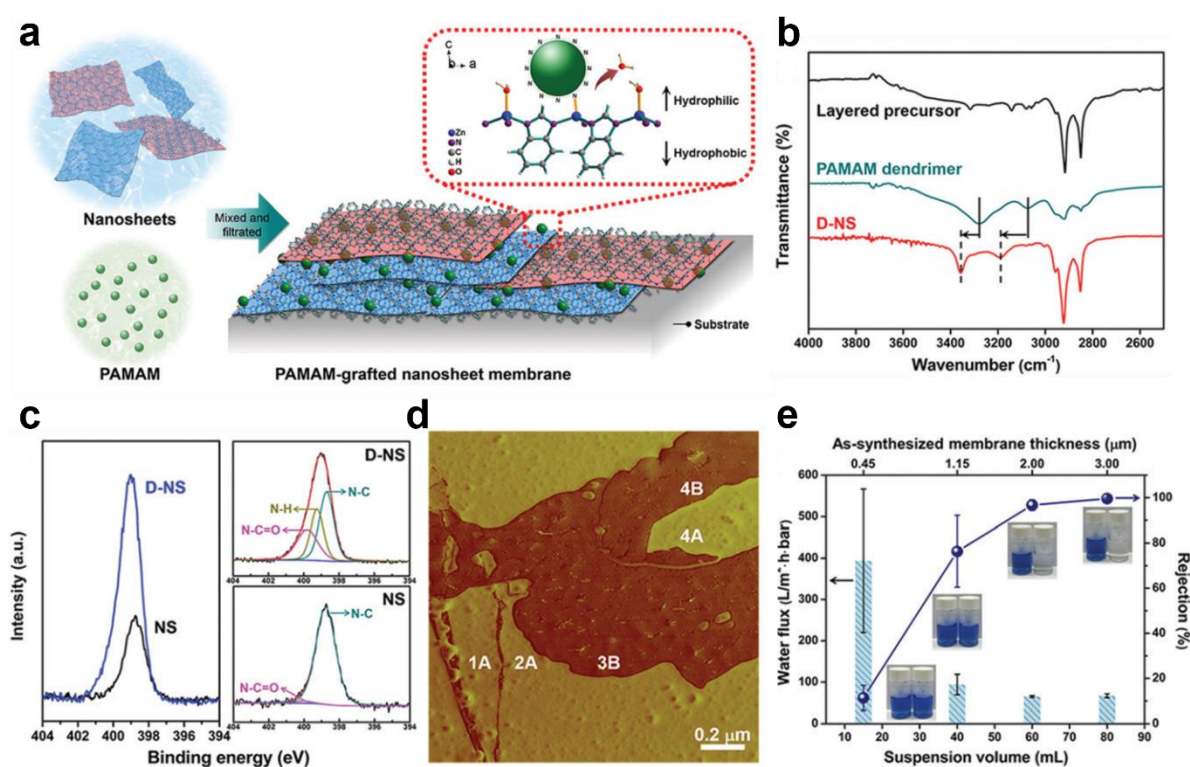


Figure 1.22. (a) schematic illustration of the PAMAM-grafted nanosheet membrane fabrication. Blue and pink represent the hydrophilic and hydrophobic nanosheet faces respectively. (b) FTIR spectra showing the blue-shift and (c) XPS spectra showing peak intensity increase, both used to confirm PAMAM grafting. (d) AFM showing the hydrophilic side (A) and hydrophobic side (B) of ZIF nanosheets. (e) Separation performance of the D-NS membrane with respect to membrane thickness when rejecting Evans blue dye. The pristine nanosheets and PAMAM grafted nanosheets are denoted as NS and D-NS respectively. Figure reproduced from reference 108.

T Li *et al.* also used ZIFs in thin-film composites to remove organic dyes and salts from water.¹⁰⁹ The 2D ZIF used in this case was Zn₂(Bim)₄, crosslinked by PEI and deposited on polyvinylidene fluoride (PVDF). The PEI was attributed to the crack-free functional layer on the membrane which enabled the

improved performance. The membranes showed a good permeance of 290 LMHB and high rejection rates (> 98%) of organic dyes. The paper reports a good stability as the rejection and permeance remain relatively stable over a 20-hour prolonged test period.

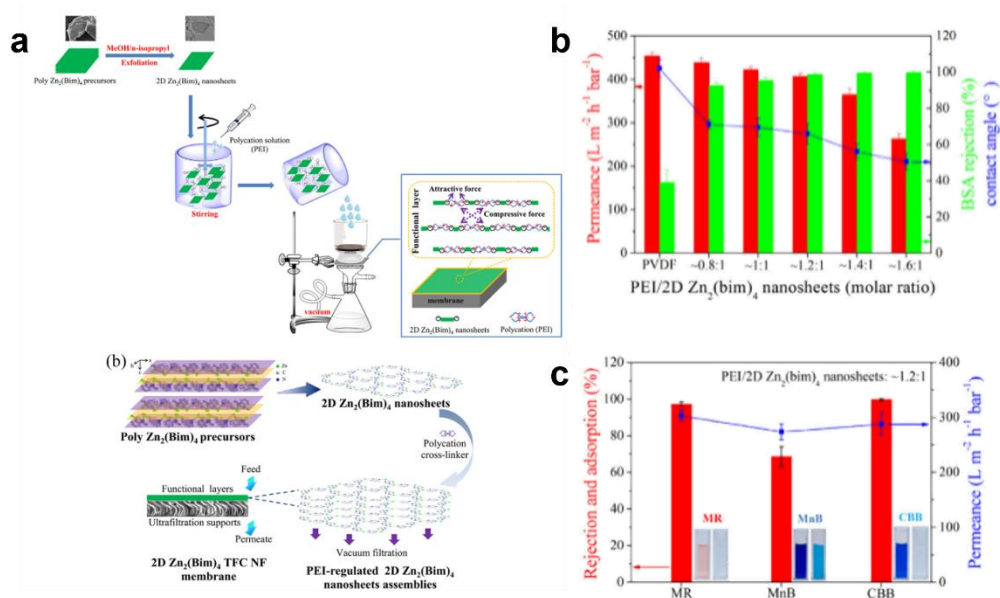


Figure 1.23. (a) schematic illustrating of fabrication of the 2D Zn₂(Bim)₄ TFC membrane, membrane performance for the rejection of (b) BSA solution and (c) organic dyes, whereby MR = methyl red, MnB = methylene blue, CRR = Coomassie brilliant blue (also known as brilliant blue G). Figure reproduced from reference 109.

The final paper to be discussed in this section was published in 2020 by *L Shu et al.* and involved the use of a 2D MOF named BUT-203 in a polyethyleneimine (PEI) and hydrolysed polyacrylonitrile (HPAN) mixed matrix membrane (MMM).¹¹⁰ BUT-203 was specifically designed and synthesised for nanofiltration MMMs, and consists of the formula Cu(NDC(SO₃)₂)_{0.5}(DPE)(H₂O), where NDC(SO₃)₂⁴⁻ and DPE refer to 4,8-disulfonyl-2,6-naphthalenedicarboxylate and 1,2-di(4-pyridyl)ethylene respectively. The BUT-203 nanosheets and PEI were pre-mixed then cast onto the HPAN substrate using spin coating. Prepared membranes were tested on a cross-flow system, different to all the previous papers discussed in this section, which were tested using a dead-end cell set-up (with the exception of *R. Dai et al.*¹⁰⁵).^{100–104,106,108,109} As the loading of the MONs was increased from 0 to 73 %, the permeance of the membrane increased from 148.3 to 885.1 L m⁻² h⁻¹ MPa⁻¹ while the rejection of methyl blue didn't drop below 93%. Once the BUT-203 loading exceeded 73% the rejection begins to drop, the authors attribute this to the reduction of PEI in the membranes allowing nanosheets to peel-off the substrate

during the cross-flow tests. Five anionic dyes were also tested with eriochome black T giving the best performance with permeance of $910 \text{ L m}^{-2} \text{ h}^{-1} \text{ MPa}^{-1}$ and a rejection of 99.7%.

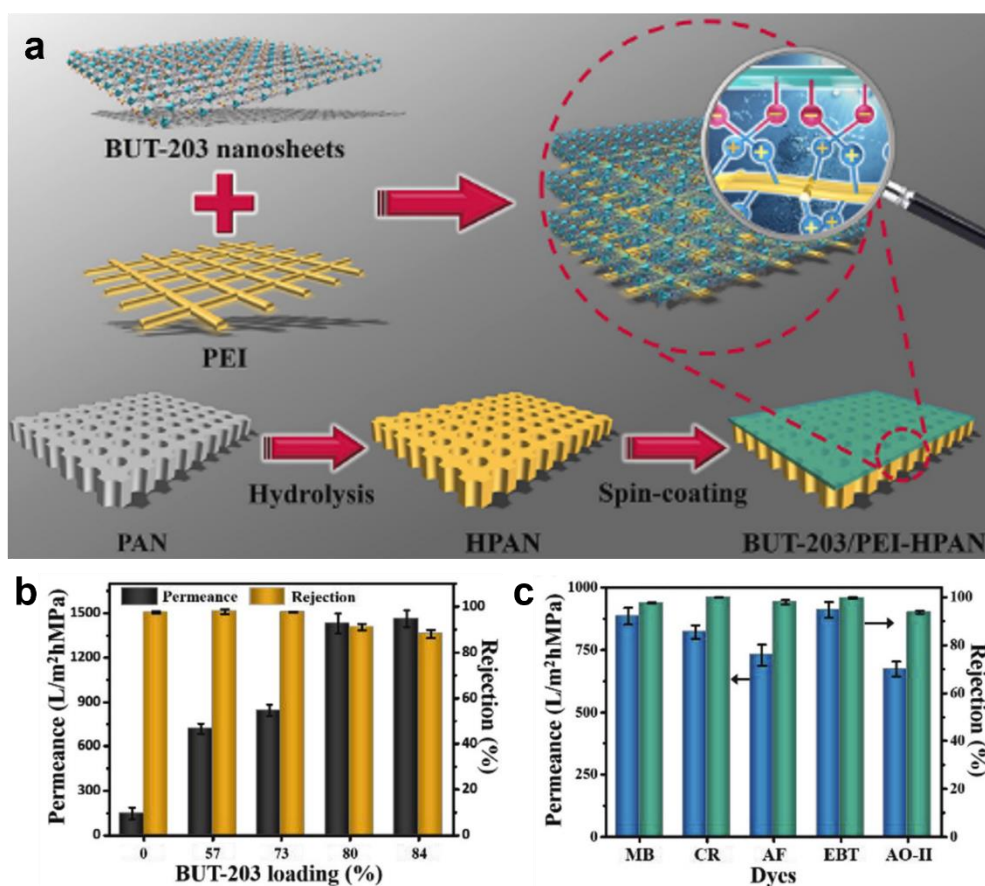


Figure 1.24. (a) schematic illustration showing the BUT-203/PEI-HPAN membrane fabrication method, (b) membrane performance with increasing BUT-203 loading tested with methylene blue, (c) membrane performance when tested with different anionic dyes, namely methylene blue (MB), congo red (CR), acid fuchsin (AF), eriochome black T (EBT) and acid orange II (AO-II). Figure adapted from reference 110. Table 1.1 was constructed by extracting from the 9 most relevant papers' key details about the conditions under which maximum rejection and permeance were achieved. The small number of examples combined with the significant differences in the membrane type, composition and applications make it difficult to draw many general conclusions, but this data does provide some useful insights.

Membrane	MON loading	Pore aperture (nm)	Analyte	Permeance (LMHB)	Rejection (%)	Operating pressure (bar)	Filtration system	Reference
Zn-TCPP(Fe)/PEI-Nylon	80 mg/m ²	1.18	Brilliant Blue G	4243	99	0.01	Stirred vacuum filtration	100
Zn-TCPP/PVCL-PVP-Nylon	10.3 mg/m ²	1.18	Crystal Violet	818	99.9	1	Dead-end cell	101
Zn-TCPP/PA-PES	269 mg/m ²	1.18	NaCl	4.82	97.4	16	Cross-flow	103
Cu-TCPP/P84	1.5 wt%	1.18	Brilliant Blue R	2.8	94.7	7	Dead-end cell	104
CuBDC/PA-PES	0.12 wt%	0.52	NaCl	3.13	-	0.1	Cross-flow	105
CuBDC/BC	-	0.52	Nitrobenzene	160.5	68.6	1.38	Dead-end cell	106
Zn ₂ (Bim) ₃ (OH)(H ₂ O)/PAMAM-Al ₂ O ₃	6.3 wt%	0.62	Evans blue	67	99.4	1	Dead-end cell	108
Zn ₂ (Bim) ₄ /PEI-PVDF	0.12 wt%	0.21	Brilliant Blue G	290	98	1	Dead-end cell	109
BUT-203/PEI-HPAN	0.63 mg/ml	1.1	Methyl blue	8851	97.9	8	Cross-flow	110

Table 1.1. Comparison of previously published MON-membrane water purification papers. Membrane notation is as follows: MON/polymer-support.

In Table 1.1 **Error! Reference source not found.**, MON loadings are recorded as a mass loading of MONs deposited onto a membrane support, in this table optimum loadings from reference papers are compared. Due to the disparity in reporting style for water purification papers, a variety of units are used to describe the MON-membrane preparation. Where possible, these units were converted to mg m^{-2} for easy comparison, however due to varying amounts of details being published, this was not possible in all cases.

As can be seen in Table 1.1, MON loadings vary from 10.3 to 269 mg m^{-2} , in alternative notation, loadings of other MONs vary from 0.12 wt% to 6.3 wt%. Membranes with lower loadings do display higher permeance, as is expected, but rejection of the individual analytes does not necessarily improve with increasing loadings.

With the exception of the CuBDC/BC membranes, all of the rejections are >90%, irrespective of the analyte the membrane is rejecting. Only Zn-TCPP(Fe)/PEI and $\text{Zn}_2(\text{Bim})_4/\text{PEI-PVDF}$ reject the same analyte, Brilliant blue G (BBG) so a more direct comparison can be drawn. The pore apertures are 1.18 and 0.21 nm respectively, showing that the smaller pore size is not necessary for the rejection of BBG. The permeance and rejections are 4243 LMHB and 99% for Zn-TCPP(Fe)/PEI and 290 LMHB and 98% for $\text{Zn}_2(\text{Bim})_4/\text{PEI-PVDF}$. 4243 LMHB is a remarkable permeance and is likely due to the significantly larger pore size of Zn-TCPP compared to CuBDC, however 290 LMHB is still an acceptable permeance for an ultrafiltration membrane. At 99% and 98% both membranes have excellent rejection that would be accepted on a commercial membrane. The final difference is the filtration system the authors used, with the former using a stirred vacuum filtration set up at 0.01 bar, while the latter uses the more common dead-end cell at 1 bar. A better comparison would be to see if the performance of the Zn-TCPP(Fe)/PEI membrane holds up under the dead-end cell tests.

When looking more broadly at pore apertures, the nanosheets with the smallest pores would be expected to have the highest rejection and lowest permeance. Considering that PA based membranes will have intrinsically low permeance and excluding those MON-membranes, the other membranes

do not follow this trend. Figure 1.25 shows the pore apertures against permeance (Figure 1.25a) and rejection (Figure 1.25b) for the data detailed in Table 1.1.

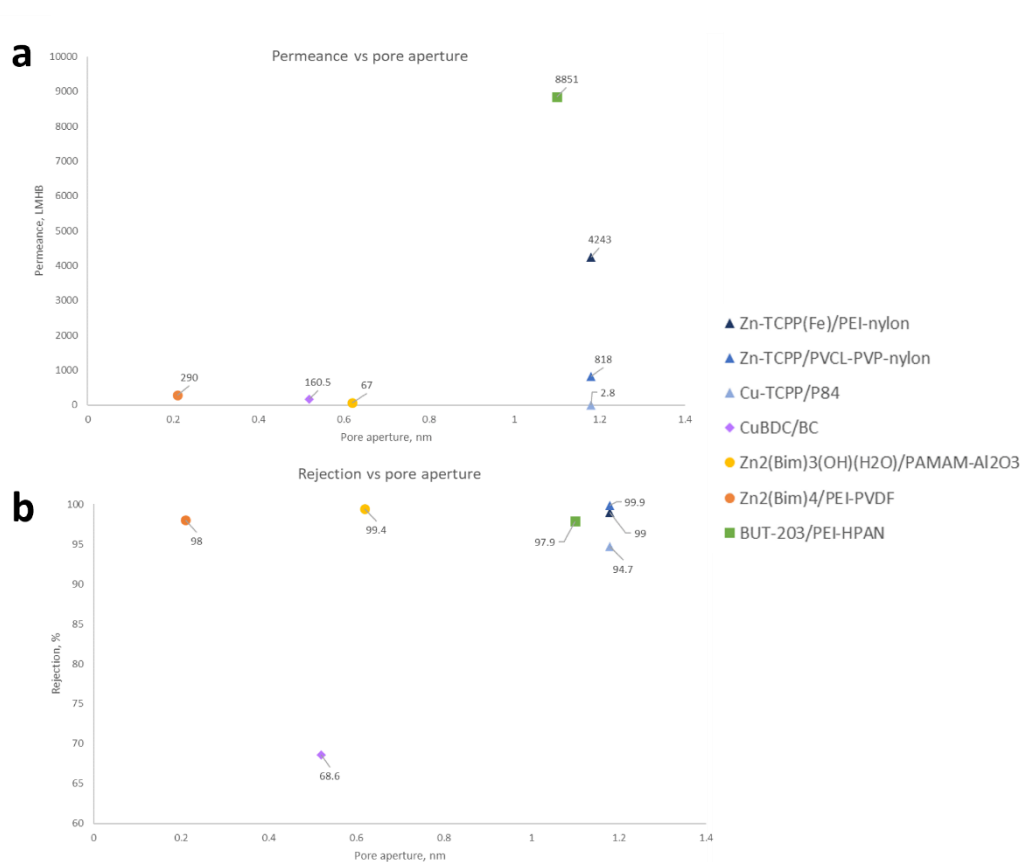


Figure 1.25. comparisons of pore aperture against (a) permeance and (b) rejection for results detailed in **Error! Reference source not found.**

With the exception of Cu-TCPP/P84 where the Cu-TCPP is incorporated into P84 without a support layer, and CuBDC/BC where the membrane consists of only MON and support, all of the membranes have a polymer additive in addition to the support membrane. In the case of Zn-TCPP/PA-PES and CuBDC/PA-PES, polyamide is technically the additive in the mixed matrix membrane, it is actually a thin film nanocomposite (TFN) formed via interfacial polymerisation, so the MONs are intrinsically part of the polymer active layer rather than just coated/cross-linked by a polymer additive. Polyamides have such a small pore structure they are mainly classed as RO membranes, and occasionally used for NF applications.¹¹¹ There can be difficulties incorporating different nanocomposites into polyamides, however the organic character in metal-organic nanosheets allow MONs to be effectively incorporated into the TFN, with evidence for potential cross-linking.¹¹² When comparing Zn-TCPP/PA-

PES and *CuBDC/PA-PES*, the MON with the larger pores, *Zn-TCPP*, provides the bigger improvement in permeance.

The other commonly used polymer additive in MON-membranes is polyethylenimine (PEI). For the three examples of MON-membranes where PEI is the polymer additive, the permeance is wildly different, whereas the rejection of organic dyes is relatively similar. The explanation of this differing permeance can come from the pore apertures. The larger pored MONs (*Zn-TCPP* and *BUT-203*) have a higher permeance than $\text{Zn}_2(\text{Bim})_4$. Apart from the frequency of its use suggesting it is easy to work with, and does not negatively affect the membranes, there is no other evidence to suggest PEI is a superior additive to the other polymers used in MON-membranes.

Similarly, to the additives there is a range of substrates used in the membrane preparation, Nylon and *PES* seem popular, however other than this there are no obvious differences in any of the substrate choices.

1.9. Conclusions

There are significant limitations to current commercial water purification technology that mean it is not able to rise to meet the growing industrial and domestic demands. Polymeric membranes offer low cost, easy processability and flexibility, however the trade-off between water permeance and separation is the largest issue facing polymer membranes, with a poor resistance to fouling close behind. The use of inorganic filler materials in membranes to prepare composite and mixed matrix membranes is a technique used to improve polymer membranes and reduce the effect of aforementioned issues. While 3D inorganic materials such as zeolites, ceramics and MOFs have been incorporated into membranes with success, the bulky nature of these materials can prevent the formation of thin films, in turn slowing the permeance of the membranes. 2D materials have been gaining interest in recent years due to the atomic thickness and flexibility that 3D materials cannot offer. Graphene-based material as well as transition metal dichalcogenides, MXenes and 2D covalent organic frameworks to name but a few examples have all been investigated in composite and mixed

matrix membrane applications. One 2D material that has been gaining traction in water purification membranes since the first published example in 2017 is metal-organic nanosheets (MONs). MONs offer ultrathin thickness (often approaching monolayer) and flexibility, allowing the formation of thin films. Additionally, MONs offer well defined and tunable pores and adaptable surface chemistry granting the ability to tailor nanosheets to specific membrane applications.

This PhD thesis aims to explore the use of MONs in water purification membranes and demonstrate their potential in this application. In this work, a MON-membrane preparation and testing method is developed and used to test a number of different MON-membrane systems. Promising composites are then optimised to evaluate their water purification efficacy. **Chapter 2** explores the synthesis of 2D UiO analogues for inclusion in composite membranes, including the synthesis of a novel mixed amino- and tetrafluoro- linker system. In **Chapter 3** these 2D UiO analogues are used to develop the method of membrane preparation and testing that underpins the rest of this work. **Chapter 4** serves as a screening experiment where MON systems already known to the Foster group were synthesised and analysed for water purification membranes. **Chapter 5** takes the most promising MON candidate from the screening experiments for further optimisation and testing to understand the capabilities of this MON-membrane. Finally, **Chapter 6** draws the previous four chapters together in an overall conclusion and outlook.

1.10. References

- 1 M. Elimelech, *J. Water Supply Res. Technol. - AQUA*, 2006, **55**, 3–10.
- 2 M. A. Shannon, P. W. Bohn, M. Elimelech, J. G. Georgiadis, B. J. Marñas and A. M. Mayes, *Nature*, 2008, **452**, 301–310.
- 3 Y. H. Teow and A. W. Mohammad, *Desalination*, 2019, **451**, 2–17.
- 4 J. R. Werber, C. O. Osuji and M. Elimelech, *Nat. Rev. Mater.*, 2016, **1**, 119-133.
- 5 N. Misdan, W. J. Lau and A. F. Ismail, *Desalination*, 2012, **287**, 228–237.
- 6 P. S. Goh and A. F. Ismail, *Desalination*, 2018, **434**, 60-80.
- 7 N. L. Le and S. P. Nunes, *Sustain. Mater. Technol.*, 2016, **7**, 1–28.
- 8 B. Jun, Y. A. J. Al-hamadani, A. Son, C. Min and M. Jang, *Sep. Purif. Technol.*, 2020, **247**, 116947.
- 9 D. M. Warsinger, S. Chakraborty, E. W. Tow, M. H. Plumlee, C. Bellona, S. Loutatidou, L. Karimi, A. M. Mikelonis, A. Achilli, A. Ghassemi, L. P. Padhye, S. A. Snyder, S. Curcio, C. D. Vecitis, H. A. Arafat, J. H. L. V and J. H. Lienhard, *Prog. Polym. Sci.*, 2018, **81**, 209–237.
- 10 D. Qadir, H. Mukhtar and L. K. Keong, *Sep. Purif. Rev.*, 2017, **46**, 62–80.
- 11 L. Loske, K. Nakagawa, T. Yoshioka and H. Matsuyama, *Membranes (Basel)*, 2020, **10**, 1–40.
- 12 G. M. Geise, H. Lee, D. J. Miller, B. D. Freeman, J. E. McGrath and D. R. Paul, *J. POLYM. SCI. PART B POLYM. PHYS*, 2010, **48**, 1685–1718.
- 13 J. G. Wijmans and R. W. Baker, *J. Memb. Sci.*, 1995, **107**, 1–21.
- 14 Y. Roy, D. M. Warsinger and J. H. Lienhard, *Desalination*, 2017, **420**, 241–257.
- 15 L. Wang, T. Cao, J. E. Dykstra, S. Porada, P. M. Biesheuvel and M. Elimelech, *Environ. Sci. Technol.*, 2021, **55**, 16665–16675.
- 16 W. Guo, H. H. Ngo and J. Li, *Bioresour. Technol.*, 2012, **122**, 27–34.
- 17 Z. Yang, Y. Zhou, Z. Feng, X. Rui, T. Zhang and Z. Zhang, *Polymers (Basel)*, 2019, **11**, 1–22.
- 18 L. M. Robeson, *J. Memb. Sci.*, 1991, **62**, 165–185.
- 19 G. M. Geise, H. Bum, A. C. Sagle, B. D. Freeman and J. E. Mcgrath, *J. Memb. Sci.*, 2011, **369**, 130–138.
- 20 H. B. Park, J. Kamcev, L. M. Robeson, M. Elimelech and B. D. Freeman, *Science (80-.)*, , 2017, **356**, 1137.
- 21 R. Zhang, J. Tian and B. Van Der Bruggen, *J. Mater. Chem. A*, 2020, **8**, 8831–8847.
- 22 L. G. Peeva, M. Sairam and A. G. Livingston, in *Comprehensive Membrane Science and Engineering*, eds. E. Drioli and L. Giorno, Elsevier, 2010, pp. 91–113.
- 23 K. A. Mahmoud, B. Mansoor, A. Mansour and M. Khraisheh, *Desalination*, 2015, **356**, 208–225.
- 24 M. S. Attia, A. O. Youssef, M. N. Abou-Omar, E. H. Mohamed, R. Boukherroub, A. Khan, T. Altalhi and M. A. Amin, *Chemosphere*, 2022, **292**, 133369.

- 25 J. O. Hsieh, K. J. Balkus, J. P. Ferraris and I. H. Musselman, *Microporous Mesoporous Mater.*, 2014, **196**, 165–174.
- 26 Z. Kang, Y. Peng, Y. Qian, D. Yuan, M. A. Addicoat, T. Heine, Z. Hu, L. Tee, Z. Guo and D. Zhao, *Chem. Mater.*, 2016, **28**, 1277–1285.
- 27 H. Ruan, C. Guo, H. Yu, J. Shen, C. Gao, A. Sotto and B. Van der Bruggen, *Ind. Eng. Chem. Res.*, 2016, **55**, 12099–12110.
- 28 G. S. Lai, W. J. Lau, P. S. Goh, Y. H. Tan, B. C. Ng and A. F. Ismail, *Arab. J. Chem.*, 2019, **12**, 75–87.
- 29 Y. Gong, S. Gao, Y. Tian, Y. Zhu and W. Fang, *J. Memb. Sci.*, 2020, **600**, 117874.
- 30 S. Kitagawa and K. Uemura, *Chem. Soc. Rev.*, 2005, **34**, 109–119.
- 31 R. Robson, *J. Chem. Soc. Dalt. Trans.*, 2000, 3735–3744.
- 32 D. Ma, G. Han, S. B. Peh and S. B. Chen, *Ind. Eng. Chem. Res.*, 2017, **56**, 12773–12782.
- 33 R. Lin, B. Villacorta Hernandez, L. Ge and Z. Zhu, *J. Mater. Chem. A*, 2018, **6**, 293–312.
- 34 R. Zhang, S. Ji, N. Wang, L. Wang, G. Zhang and J. R. Li, *Angew. Chemie - Int. Ed.*, 2014, **53**, 9775–9779.
- 35 K. S. Park, Z. Ni, A. P. Côté, J. Y. Choi, R. Huang, F. J. Uribe-Romo, H. K. Chae, M. O’Keeffe and O. M. Yaghi, *Proc. Natl. Acad. Sci. U. S. A.*, 2006, **103**, 10186–10191.
- 36 J. H. Cavka, S. Jakobsen, U. Olsbye, N. Guillou, C. Lamberti, S. Bordiga and K. P. Lillerud, *J. Am. Chem. Soc.*, 2008, **130**, 13850–13851.
- 37 C. Férey, C. Mellot-Draznieks, C. Serre, F. Millange, J. Dutour, S. Surblé and I. Margiolaki, *Science*, 2005, **309**, 2040–2042.
- 38 D. Ma, G. Han, S. B. Peh and S. B. Chen, *Ind. Eng. Chem. Res.*, 2017, **56**, 12773–12782.
- 39 X. Liu, N. K. Demir, Z. Wu and K. Li, *J. Am. Chem. Soc.*, 2015, **137**, 6999–7002.
- 40 L. Wan, C. Zhou, K. Xu, B. Feng and A. Huang, *Microporous Mesoporous Mater.*, 2017, **252**, 207–213.
- 41 R. Zhang, S. L. Ji, N. X. Wang, L. Wang, G. J. Zhang and J.-R. Li, *Angew. Chem. Int. Ed.*, 2014, **53**, 9775–9779.
- 42 J. Duan, Y. Pan, F. Pacheco, E. Litwiller, Z. Lai and I. Pinnau, *J. Memb. Sci.*, 2016, **476**, 303–310.
- 43 S. Kim, H. Wang and Y. M. Lee, *Angew. Chemie Int. Ed.*, 2019, 17512–17527.
- 44 D. Cohen-tanugi and C. Grossman, *Nano Lett.*, 2012, **12**, 3602–3608.
- 45 F. Perreault, A. Fonseca De Faria and M. Elimelech, *Chem. Soc. Rev.*, 2015, **44**, 5861–5896.
- 46 M. Fathizadeh, W. L. Xu, F. Zhou, Y. Yoon and M. Yu, *Adv. Mater. Interfaces*, 2017, **4**, 1600918.
- 47 M. Hu and B. Mi, *Environ. Sci. Technol.*, 2013, **47**, 3715–3723.
- 48 S. Dervin, D. D. Dionysiou and S. C. Pillai, *Nanoscale*, 2016, **8**, 15115–15131.
- 49 A. Eftekhari, *J. Mater. Chem. A*, 2017, **5**, 18299–18325.
- 50 L. Sun, H. Huang and X. Peng, *Chem. Commun.*, 2013, **49**, 10718–10720.

- 51 M. Naguib, M. Kurtoglu, V. Presser, J. Lu, J. Niu, M. Heon, L. Hultman, Y. Gogotsi and M. W. Barsoum, *Adv. Mater.*, 2011, **23**, 4248–4253.
- 52 C. E. Ren, K. B. Hatzell, M. Alhabeab, Z. Ling, K. A. Mahmoud and Y. Gogotsi, *J. Phys. Chem. Lett.*, 2015, **6**, 4026–4031.
- 53 S. N. S. A. Aziz, M. N. A. Seman and S. M. Saufi, *IOP Conf. Ser. Mater. Sci. Eng.*, 2020, **736**, 052026.
- 54 J. Zhu, N. Guo, Y. Zhang, L. Yu and J. Liu, *J. Memb. Sci.*, 2014, **465**, 91–99.
- 55 A. Lee, J. W. Elam and S. B. Darling, *Environ. Sci. Water Res. Technol.*, 2016, **2**, 17–42.
- 56 R. Singh, in *Membrane Technology and Engineering for Water Purification*, 2015, pp. 1–80.
- 57 J. Wang and X. Liu, *J. Clean. Prod.*, 2021, **280**, 124354.
- 58 A. Ambrosi, N. S. M. Cardozo and I. C. Tessaro, *Food Bioprocess Technol.*, 2014, **7**, 921–936.
- 59 M. Fadel, Y. Wyart and P. Moulin, *Membranes (Basel)*, 2020, **10**, 1–14.
- 60 D. J. Ashworth, A. Cooper, M. Trueman, R. W. M. Al-Saedi, S. D. Liam, A. J. Meijer and J. A. Foster, *Chem. - A Eur. J.*, 2018, **24**, 17986–17996.
- 61 R. Sakamoto, K. Takada, T. Pal, H. Maeda, T. Kambe and H. Nishihara, *Chem. Commun.*, 2017, **53**, 5781–5801.
- 62 J. Nicks, K. Sasitharan, R. R. R. Prasad, D. J. Ashworth and J. A. Foster, *Adv. Funct. Mater.*, 2021, **31**, 2103723.
- 63 D. J. Ashworth and J. A. Foster, *J. Mater. Chem. A*, 2018, **6**, 16292–16307.
- 64 L. G. Qiu, Z. Q. Li, Y. Wu, W. Wang, T. Xu and X. Jiang, *Chem. Commun.*, 2008, 3642–3644.
- 65 Y. Xu, B. Li, S. Zheng, P. Wu, J. Zhan, H. Xue, Q. Xu and H. Pang, *J. Mater. Chem. A*, 2018, **6**, 22070–22076.
- 66 R. Dong, Z. Zheng, D. C. Tranca, J. Zhang, N. Chandrasekhar, S. Liu, X. Zhuang, G. Seifert and X. Feng, *Chem. - A Eur. J.*, 2017, **23**, 2255–2260.
- 67 D. Rodríguez-San-Miguel, P. Amo-Ochoa and F. Zamora, *Chem. Commun.*, 2016, **52**, 4113–4127.
- 68 R. Xu, Z. Cai, G. Lan and W. Lin, *Inorg. Chem.*, 2018, **57**, 10489–10493.
- 69 M. Zhao, Y. Huang, Y. Peng, Z. Huang, Q. Ma and H. Zhang, *Chem. Soc. Rev.*, 2018, **47**, 6267–6295.
- 70 M. Zhao, Y. Wang, Q. Ma, Y. Huang, X. Zhang, J. Ping, Z. Zhang, Q. Lu, Y. Yu, H. Xu, Y. Zhao and H. Zhang, *Adv. Mater.*, 2015, **27**, 7372–7378.
- 71 A. Pustovarenko, M. G. Goesten, S. Sachdeva, M. Shan, Z. Amghouz, Y. Belmabkhout, A. Dikhtiarenko, T. Rodenas, D. Keskin, I. K. Voets, B. M. Weckhuysen, M. Eddaoudi, L. C. P. M. de Smet, E. J. R. Sudhölter, F. Kapteijn, B. Seoane and J. Gascon, *Adv. Mater.*, 2018, **30**, 1–8.
- 72 A. Schaate, P. Roy, A. Godt, J. Lippke, F. Waltz, M. Wiebcke and P. Behrens, *Chem. - A Eur. J.*, , 2011, **17**, 6643–6651.
- 73 M. J. Cliffe, E. Castillo-Martínez, Y. Wu, J. Lee, A. C. Forse, F. C. N. Firth, P. Z. Moghadam, D. Fairen-Jimenez, M. W. Gaultois, J. A. Hill, O. V. Magdysyuk, B. Slater, A. L. Goodwin and C. P.

- Grey, *J. Am. Chem. Soc.*, 2017, **139**, 5397–5404.
- 74 F. C. N. Firth, M. J. Cliffe, D. Vulpe, M. Aragonés-Anglada, P. Z. Moghadam, D. Fairen-Jimenez, B. Slater and C. P. Grey, *J. Mater. Chem. A*, 2019, **7**, 7459–7469.
- 75 R. Makiura, S. Motoyama, Y. Umemura, H. Yamanaka, O. Sakata and H. Kitagawa, *Nat. Mater.*, 2010, **9**, 565–571.
- 76 T. Rodenas, I. Luz, G. Prieto, B. Seoane, H. Miro, A. Corma, F. Kapteijn, F. X. Llabrés I Xamena, J. Gascon, F. X. Llabrés and J. Gascon, *Nat. Mater.*, 2015, **14**, 48–55.
- 77 M. Lee, L. Javier, S. Man, J. Vit, S. Makars, P. G. Steeneken, H. S. J. Van Der Zant, M. Guillermo and E. Coronado, *J. Am. Chem. Soc.*, 2021, **143**, 18502–18510.
- 78 A. Abhervé, S. Mañas-Valero, M. Clemente-León and E. Coronado, *Chem. Sci.*, 2015, **6**, 4665–4673.
- 79 Y. Peng, Y. Li, Y. Ban and W. Yang, *Angew. Chemie - Int. Ed.*, 2017, **56**, 9757–9761.
- 80 H. Liu, Y. Chang, T. Fan and Z. Gu, *Chem. Commun.*, 2016, **2**, 12984–12987.
- 81 W. Song, *Talanta*, 2017, **170**, 74–80.
- 82 H. S. Wang, J. Li, J. Y. Li, K. Wang, Y. Ding and X. H. Xia, *NPG Asia Mater.*, 2017, **9**, 1–9.
- 83 X. Wang, C. Chi, K. Zhang, Y. Qian, K. M. Gupta, Z. Kang, J. Jiang and D. Zhao, *Nat. Commun.*, 2017, **8**, 1–10.
- 84 A. Altomare, C. Cuocci, A. Moliterni and R. Rizzi, in *Inorganic Micro- and Nanomaterials: Synthesis and Characterization*, 2013, pp. 57–92.
- 85 C. E. Housecroft and A. G. Sharpe, *Inorganic Chemistry*, 2012.
- 86 K. D. M. Harris, R. L. Johnston, E. Y. Cheung, G. W. Turner, S. Habershon, D. Albesa-Jove, E. Tedesco and B. M. Kariuki, *CrystEngComm*, 2002, **4**, 356.
- 87 J. C. Tan, P. J. Saines, E. G. Bithell and A. K. Cheetham, *ACS Nano*, 2012, **6**, 615–621.
- 88 F. Cao, M. Zhao, Y. Yu, B. Chen, Y. Huang, J. Yang, X. Cao, Q. Lu, X. Zhang, Z. Zhang, C. Tan and H. Zhang, *J. Am. Chem. Soc.*, 2016, **138**, 6924–6927.
- 89 A. Dhakshinamoorthy, Z. Li and H. Garcia, *Chem. Soc. Rev.*, 2018, **47**, 8134–8172.
- 90 S. Zhao, Y. Wang, J. Dong, C. He, H. Yin, P. An, K. Zhao, X. Zhang, C. Gao, L. Zhang, J. Lv, J. Wang, J. Zhang, A. M. Khattak, N. A. Khan, Z. Wei, J. Zhang, S. Liu and H. Zhao, *Nat. Energy*, 2016, **1**, 1–10.
- 91 L. Cao, Z. Lin, F. Peng, W. Wang, R. Huang, C. Wang, J. Yan, J. Liang, Z. Zhang, T. Zhang, L. Long, J. Sun and W. Lin, *Angew. Chemie - Int. Ed.*, 2016, **55**, 4962–4966.
- 92 P. Ling, C. Qian, F. Gao and J. Lei, *Chem. Commun.*, 2018, **54**, 11176–11179.
- 93 J. Nicks, J. Zhang and J. Foster, *Chem. Commun.*, 2019, **55**, 8788–8791.
- 94 Q. Yang, L. Zhou, Y. X. Wu, K. Zhang, Y. Cao, Y. Zhou, D. Wu, F. Hu and N. Gan, *Anal. Chim. Acta*, 2018, **1020**, 1–8.
- 95 W. Xing, P. Ye, J. Lu, X. Wu, Y. Chen, T. Zhu and A. Peng, *J. Power Sources*, 2018, **401**, 13–19.
- 96 J. Yang, Z. Ma, W. Gao and M. Wei, *Chem. - A Eur. J.*, 2017, **23**, 631–636.

- 97 M. Liu, K. Xie, M. D. Nothling, P. A. Gurr, S. S. L. Tan, Q. Fu, P. A. Webley and G. G. Qiao, *ACS Nano*, 2018, **12**, 11591-11599.
- 98 M. Shete, P. Kumar, J. E. Bachman, X. Ma, Z. P. Smith, W. Xu, K. A. Mkhoyan, J. R. Long and M. Tsapatsis, *J. Memb. Sci.*, 2018, **549**, 312–320.
- 99 Y. Peng, Y. Li, Y. Ban, H. Jin, W. Jiao, X. Liu and W. Yang, *Science*, 2014, **346**, 1356–1359.
- 100 H. Ang and L. Hong, *ACS Appl. Mater. Interfaces*, 2017, **9**, 28079–28088.
- 101 W. Jia, B. Wu, S. Sun and P. Wu, *Nano Res.*, 2020, **13**, 2973–2978.
- 102 M. Jian, R. Qiu, Y. Xia, J. Lu, Y. Chen, Q. Gu, R. Liu, C. Hu, J. Qu, H. Wang and X. Zhang, *Sci. Adv.*, 2020, **6**, 1–10.
- 103 Y. Wen, X. Zhang, X. Li, Z. Wang and C. Y. Tang, *ACS Appl. Nano Mater.*, 2020, **3**, 9238–9248.
- 104 A. Yao, D. Hua, F. Zhao, D. Zheng, J. Pan, Y. Hong, Y. Liu, X. Rao, S. Zhou and G. Zhan, *Sep. Purif. Technol.*, 2022, **282**, 120022.
- 105 R. Dai, X. Zhang, M. Liu, Z. Wu and Z. Wang, *J. Memb. Sci.*, 2019, **573**, 46–54.
- 106 X. Yin, S. Tang, Q. Yong, X. Zhang and J. M. Catchmark, *Sep. Purif. Technol.*, 2021, **276**, 119366.
- 107 M. Bergaoui, M. Khalfaoui, A. Awadallah-F and S. Al-Muhtaseb, *J. Nat. Gas Sci. Eng.*, 2021, **96**, 104289.
- 108 Y. Peng, R. Yao and W. Yang, *Chem. Commun.*, 2019, **55**, 3935–3938.
- 109 T. Li, Y. Ren, D. Wu, W. Zhang, M. Shi, C. Ji, L. Lv, M. Hua and W. Zhang, *Chemosphere*, , 2020, **261**, 127717.
- 110 L. Shu, L. H. Xie, Y. Meng, T. Liu, C. Zhao and J. R. Li, *J. Memb. Sci.*, 2020, **603**, 118049.
- 111 Y. Liang, Y. Zhu, C. Liu, K. R. Lee, W. S. Hung, Z. Wang, Y. Li, M. Elimelech, J. Jin and S. Lin, *Nat. Commun.*, 2020, **11**, 1–9.
- 112 W. J. Lau, S. Gray, T. Matsuura, D. Emadzadeh, J. Paul Chen and A. F. Ismail, *Water Res.*, 2015, **80**, 306–324.

Chapter 2

Defect-mediated synthesis to access
nanosheet phases of UiO family metal-
organic frameworks

2.1. Introduction

An archetypal example of a UiO framework is UiO-66, which has been investigated a number of times for water purification membranes due to its good water stability.¹ UiO-66 is composed of zirconium or hafnium oxide complexes bridged by 1,4-benzenedicarboxylic acid-based ligands.² In its most stable form, UiO-66 has a face-centred-cubic (**fcu**) topology (see Figure 2.1). The strong coordination bonds formed between the carboxylate-based ligands and the Zr^{4+}/Hf^{4+} ions are the key factor in the UiO water stability, a property not held by a large number of metal-organic frameworks (MOFs).^{3,4}

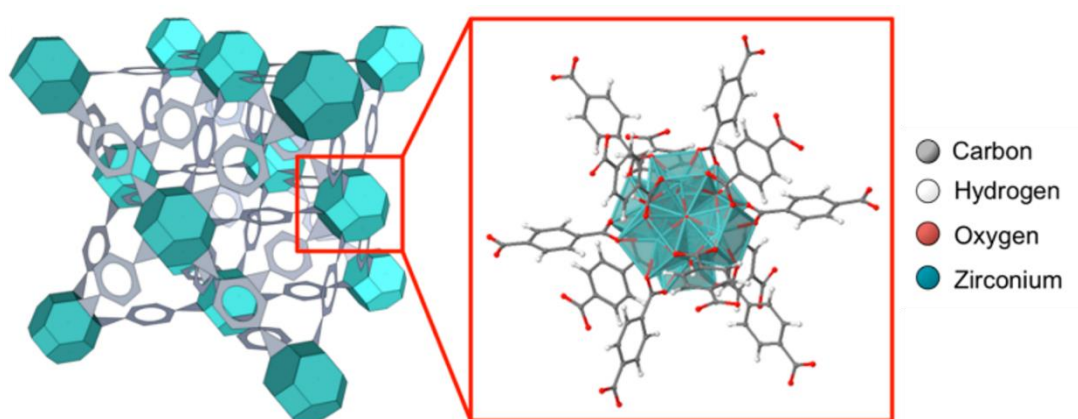


Figure 2.1. Schematic showing the structure of UiO-66. Figure adapted from reference 2.

A detailed analysis of the literature involving MOF membranes for water purification, shows that the family of MOFs with the highest incidence of research papers is the UiO- family (see **Error! Reference source not found.**). UiO-66 (Zr/Hf 1,4-benzenedicarboxylate) and UiO-66-NH₂ (Zr/Hf 2-amino-1,4-benzenedicarboxylate) have both been incorporated into a variety of membranes and used to reject different filtrates; common examples are desalination,^{5,6} antibiotics,^{7,8} organic dyes,^{9,10} and oil/water.^{11,12} The majority of these literature examples exhibit very high rejections of over 90% and a number have stability studies with excellent long term performance.^{5,13,14} Additionally the tunable porous nature of the UiO-system lends them to selectivity control in separation applications.^{5,14,15} For this reason, the UiO-family of MOFs were chosen as the initial focus for this project.

While these 3D UiO-66 MOFs have been shown to be successful in water purification membranes, there is evidence to show that a 2D MON can not only improve the water transport through the

membrane due to reduced thickness, but also enhance compatibility with the membrane itself.^{16,17} While UiO-66 is not a layered MOF that could be easily exfoliated, a defect-mediated approach leading to 2D materials for the synthesis of UiO-67 has been reported by M. Cliffe *et al.* (Figure 2.2) and then further reported for UiO-66 by F. C. N. Firth *et al.*^{18,19} It is from these methods that the synthesis of UiO- MONs in this chapter has been developed.

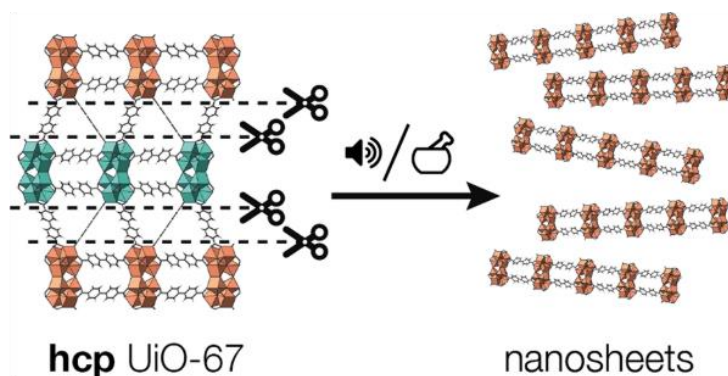


Figure 2.2. Schematic representation of the modulated synthesis of UiO-67 nanosheets. Reproduced from reference 18.

Using the standard method of UiO-66 synthesis, a **fcu** crystal structure is the most stable form, however the use of water and formic acid modulate the formation of this phase and give way to new phases.² In the modulated synthesis of UiO-66(F₄BDC) (F₄BDC = tetrafluoro-1,4-benzenedicarboxylate) reported by F. C. N. Firth *et al.*, during the first two steps the UiO-66(F₄BDC) is in a 3-dimensional layered hexagonal close packed (**hcp**) phase. The formic acid used in the synthesis mixture acts as a modulator, forming defects in the structure. The mechanism for this is explored in another publication looking at the effect of formic acid on Hf₆ clusters in MOFs by L. Cao *et al.*²⁰ The authors hypothesise that the formate groups protect six of the connection sites on the metal cluster. The remaining six sites in the same plane are able to connect to the ligands. In this case it is believed that the binding of the formic acid modulator is more favourable in the (111) plane, leaving defects between the planes of the MOF layers. When the MOF is activated, and the coordinated DMF is removed, UiO-66(F₄BDC) self-exfoliates, forming nanosheets, also referred to as the **hns** phase.¹⁹

Building on the initial studies done by F. C. N. Firth, this chapter looks deeper into the 2D nature of these UiO-66 analogues and extends the series with different linkers.¹⁹ In depth analysis of the tetrafluoro-1,4-benzenedicarboxylate UiO-66 nanosheets was first carried out, followed by the development of modulated synthesis routes for 2D UiO-66 analogues using 1,4-benzenedicarboxylic acid, 2-amino-1,4-benzenedicarboxylic acid and 1-bromo-1,4-benzenedicarboxylic acid.

2.2. Results and discussion

Four different ligands were used in the synthesis of UiO-66 analogues in this chapter; 1,4-benzenedicarboxylate (BDC), tetrafluoro-1,4-benzenedicarboxylate (F₄BDC), 2-amino-1,4-benzenedicarboxylate (NH₂BDC) and 2-bromo-1,4-benzenedicarboxylate (BrBDC). Figure 2.3 shows the chemical structures of these ligands. The formula for UiO-66 analogues is [Zr₆O₄(OH)₄]₂(OH)₆(XBDC)₉ (where X = Br, F₄, and NH₂), throughout this chapter, for ease, it will be referred to as Zr₆(XBDC).

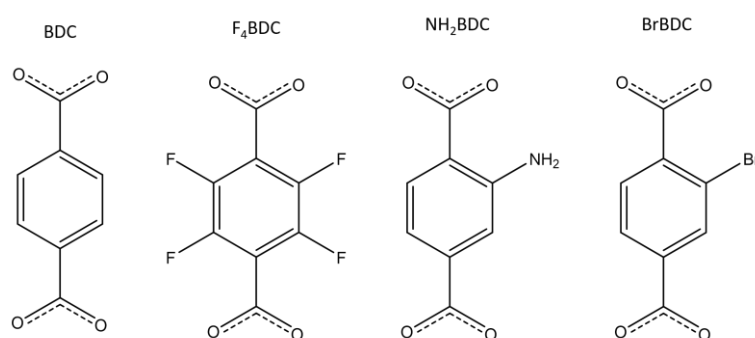


Figure 2.3. Chemical structures of ligands used in the synthesis of UiO-66 analogues in this chapter.

2.2.1. Synthesis and characterisation of Zr₆(F₄BDC)

Defect-mediated Zr₆(F₄BDC) was synthesised according to the procedure reported by F. C. N. Firth *et al.*¹⁹ Zirconium chloride (ZrCl₄) and tetrafluoro terephthalic acid (F₄BDC) were heated in a mixture of water and formic acid at 120 °C for 24 h. The white product was washed at 70 °C with DMF to remove unreacted ligand and activated at 200 °C to remove residual DMF.

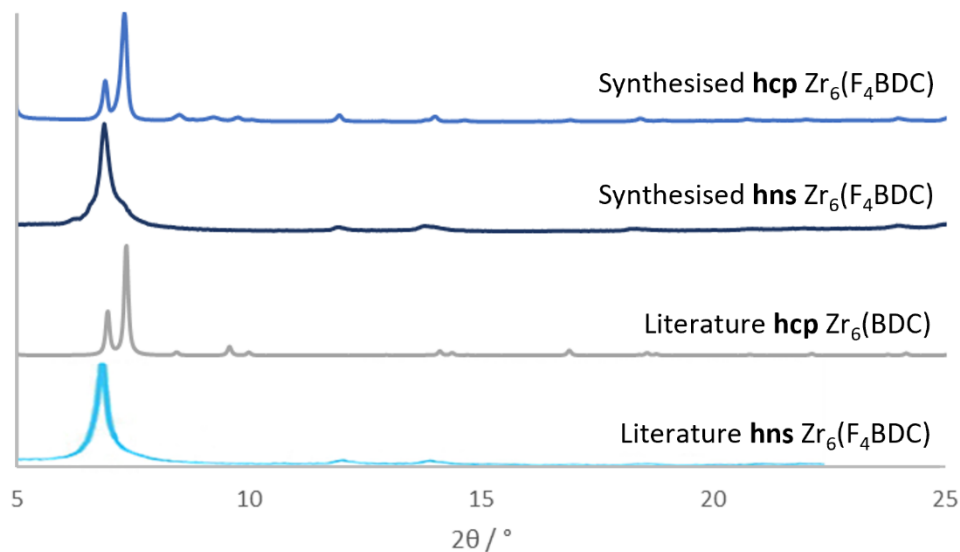


Figure 2.4. Stacked PXRD patterns comparing synthesised **hcp** and **hns** $Zr_6(F_4BDC)$ and literature reported patterns for **hns** $Zr_6(F_4BDC)$ and **hcp** $Zr_6(BDC)$. Literature **hns** $Zr_6(F_4BDC)$ reproduced from reference 19 and literature **hcp** $Zr_6(BDC)$ pattern calculated from single crystal structure in reference 18.

Powder X-ray diffraction (PXRD) was used to identify whether the **hns** phase had formed (Figure 2.4). The PXRD pattern of the as synthesised **hcp** $Zr_6(F_4BDC)$ was compared to a calculated powder pattern taken from the previously reported single crystal structure from supplementary information in reference ¹⁸ for **hcp** $Zr_6(BDC)$, the PXRD patterns have a good match and therefore the synthesis of **hcp** $Zr_6(F_4BDC)$ was successful.¹⁸ There is no CIF file available for the **hns** phase of any reported $Zr_6(XBDC)$ (whereby X can be any functional group on the terephthalic acid ligand), however comparing to the PXRD pattern reported by Firth *et al.* the pattern for the **hns** $Zr_6(F_4BDC)$ is was also successfully synthesised to a phase pure product.¹⁹ As the structure of $Zr_6(F_4BDC)$ transitions from 3D in the **hcp** phase, to 2D in the **hns** phase, it loses a plane of reflection which is observed in the reduction of peaks in the PXRD pattern.

SEM was carried out on the bulk MOF powder, showing a morphology of interpenetrated nanosheets, coming together in ball-like structure (Figure 2.5a), this is comparable to the SEM previously reported for **hcp** $Zr_6(F_4BDC)$.¹⁹

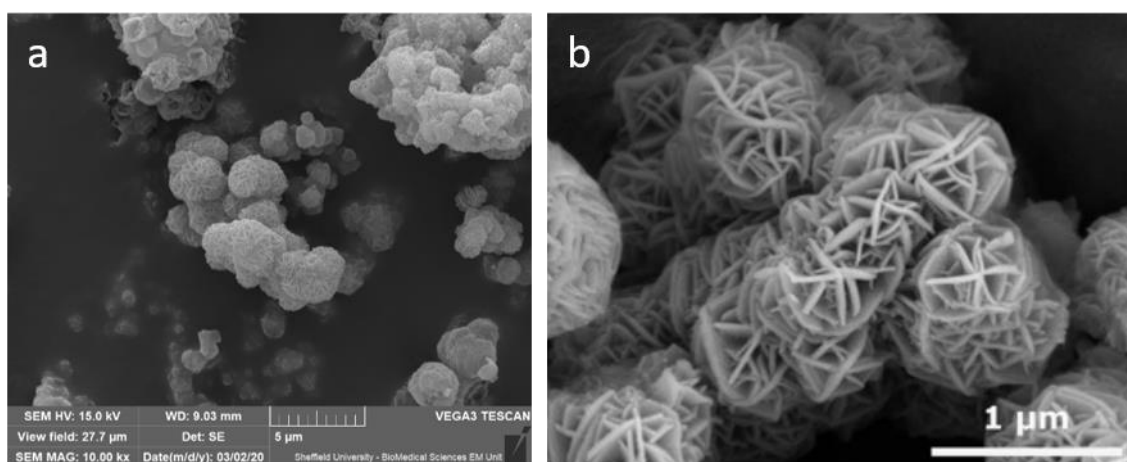


Figure 2.5. SEM images of $Zr_6(F_4BDC)$ bulk MOF (a) this work, (b) reproduced from reference 19.

The interwoven structure of these nanosheets is not ideal for forming a thin active layer on a membrane surface. However, after vigorous shaking to suspend in water, Tyndall scattering is observed, indicating the presence of colloidal material (see Figure 2.6c). AFM analysis was carried out on samples of this suspension to identify if nanosheets were present (Figure 2.6a).

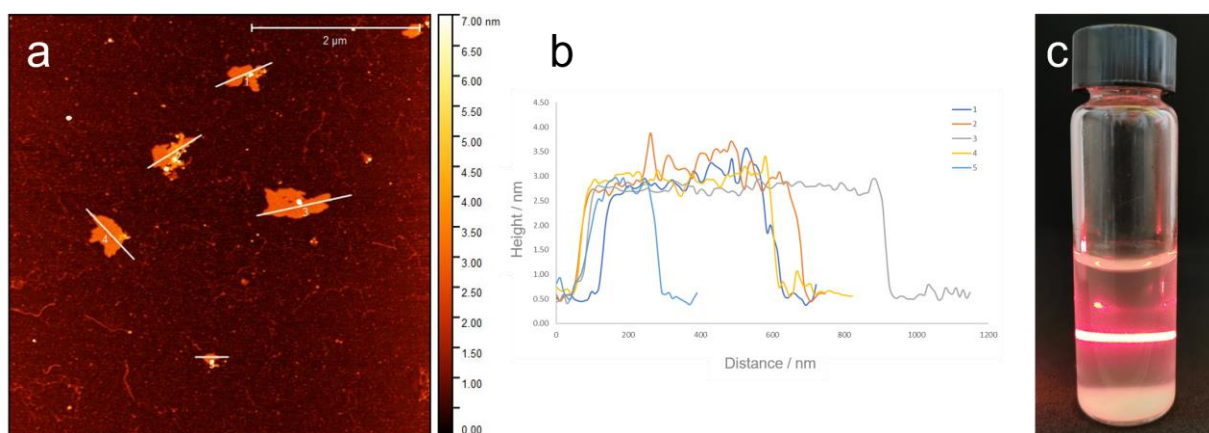


Figure 2.6. (a) AFM topographical profiles $Zr_6(F_4BDC)$ nanosheets, (b) the associated height plots of the indicated vectors on the profiles and (c) photograph of the Tyndall scattering from $Zr_6(F_4BDC)$ suspended in water.

When the $Zr_6(F_4BDC)$ samples were shaken in water to give a suspension of nanosheets, they have an average lateral dimension of 593 nm, with an average thickness of 2.4 nm, as can be seen in Figure 2.6. Based on the calculated size of the Zr_6 clusters from previously reported single crystal structures for **hcp** $Zr_6(BDC)$, 2.4 nm is approaching monolayer thickness (1.7 nm).¹⁸ These have an aspect ratio (thickness: lateral size) of 247. Large, thin nanosheets are ideal for preparing membranes with a continuous thin active layer. $Zr_6(F_4BDC)$ water suspensions were also exfoliated by immersing the

samples in an ultrasonic bath at 37 kHz for 12 h to ascertain if a higher yield of nanosheets could be achieved. Figure 2.7 shows the AFM data from this exfoliated material.

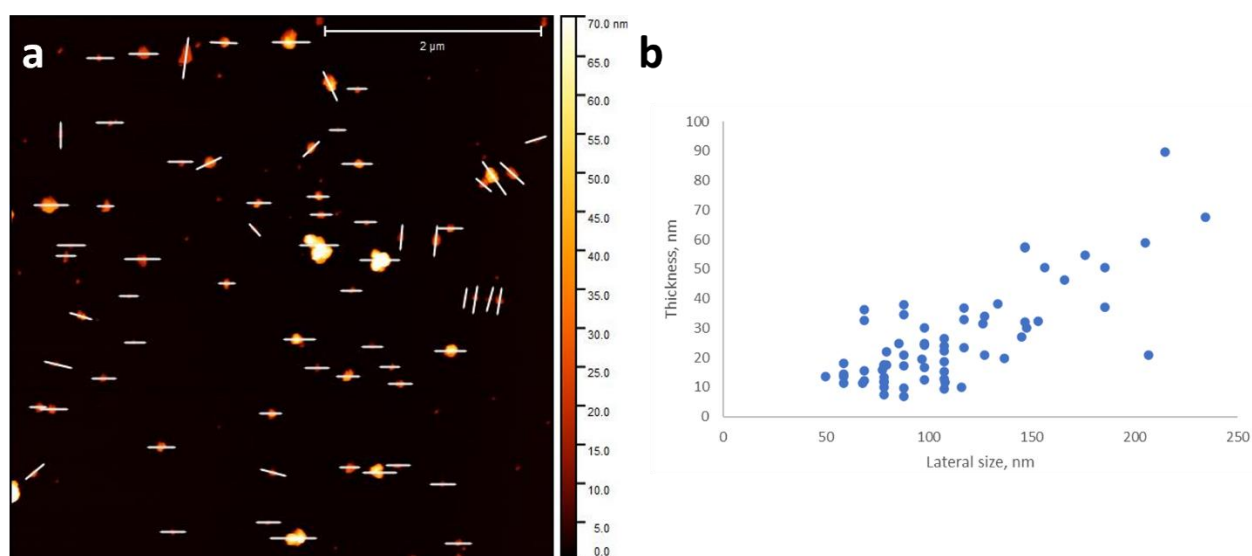


Figure 2.7. (a) AFM topological profile of $Zr_6(F_4BDC)$ after sonication in water for 12 h at 37 kHz, and (b) scatter plot of corresponding height profiles.

The average lateral size for $Zr_6(F_4BDC)$ after exfoliation is 107.9 nm, this is significantly smaller than the lateral sizes seen in the shaken sample (593 nm). The thickness of the material is also different after sonication, changing from an average of 2.4 nm to 32.9 nm. It is likely that this change in dimensions comes from the fragmentation of larger MOF particles rather than the presence of nanosheets. Qualitatively, there appears to be fewer, larger, thinner nanosheets produced when $Zr_6(F_4BDC)$ is shaken in water and a higher concentration of smaller thicker nanosheets when the $Zr_6(F_4BDC)$ is sonicated. In both cases, the nanosheets remain as a stable homogenous suspension for long periods of time.

This fragmentation is also seen in DLS analysis, whereby after sonication the size distribution of the nanosheets is reduced (Figure 2.8). Due to assumption that the particles measured using a DLS machine are spherical, not 2D, the sizes of the nanosheets given by DLS data cannot be directly compared to the size analysis from AFM data. Despite this, the general trend of sonication fragmenting nanosheets into smaller particles can be clearly interpreted from this data.

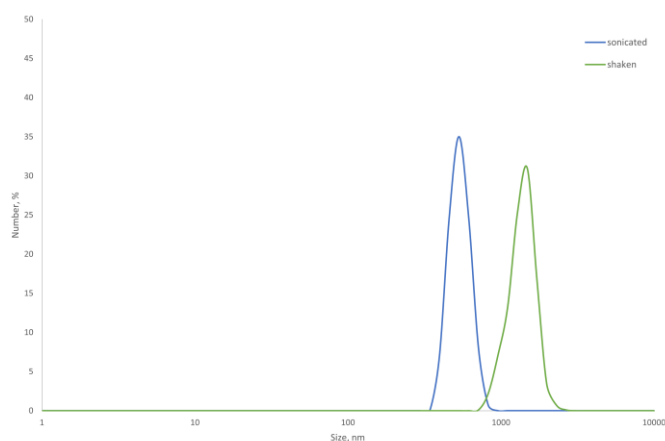


Figure 2.8. DLS number plots for suspensions of Zr₆(F₄BDC) in water after shaking (green) and sonication (37 kHz, 12 h) (blue).

To ensure these MONs produced by shaking the suspensions of Zr₆(F₄BDC) were suitable for the water purification application, a stability study was carried out. Zr₆(F₄BDC) MONs were soaked for one month in distilled water before drying. PXRD was used to determine if the crystal structure of the MONs had degraded over that time. Looking at the PXRD pattern in Figure 2.9, it is clear that the MONs have maintained their crystallinity and structure after being kept in water. From this it can be said with confidence that Zr₆(F₄BDC) MONs are stable in water over the timescale needed for water purification experiments. As can be seen in Figure 2.9, stability in methanol, ethanol and acetonitrile was also tested, with the MONs maintaining their crystallinity in all tested solvents.

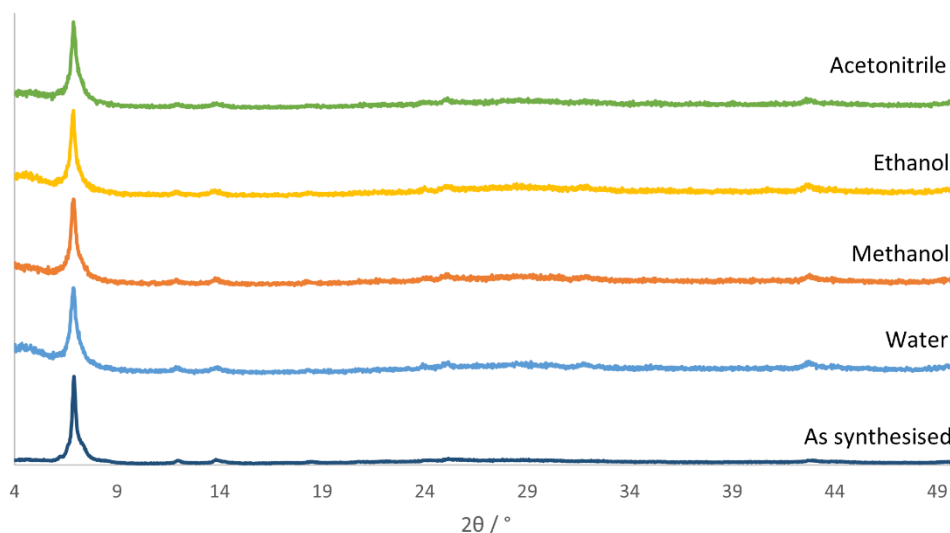


Figure 2.9. PXRD patterns for as-synthesised $Zr_6(F_4BDC)$ MONs (dark blue) and $Zr_6(F_4BDC)$ MONs after soaking in distilled water (light blue), methanol (orange), ethanol (yellow) and acetonitrile (green) for 1 month.

2.2.2. Synthesis and characterisation of $Zr_6(NH_2:F_4BDC)$

Post-synthetic modification allows functionality to be added to a metal-organic materials after they have already been synthesised, often this functionality would have changed the way the supramolecular structure formed.²¹ One of the most accessible functionalities for post-synthetic modification is the amino group, therefore it was targeted when trying to synthesis other analogues of $Zr_6(F_4BDC)$. Additionally, inclusion of amino groups has been shown to improve the wettability of nanosheets.²² The same general synthesis procedure used to synthesise $Zr_6(F_4BDC)$ was adapted for synthesis of $Zr_6(NH_2BDC)$. Zirconium chloride ($ZrCl_4$) and amino terephthalic acid (NH_2BDC) were heated in a mixture of DMF, water and formic acid at 120 °C for 24 h. The product was then washed at 70 °C with DMF to remove unreacted ligand and activated at 200 °C to remove residual DMF.

A range of water and formic acid volumes were used and the PXRD patterns were evaluated to see if the **hcp** phase was present, from which the nanosheet phase (**hns**) is accessible. Figure 2.10 shows the stacked PXRD patterns of $Zr_6(NH_2BDC)$ synthesised with 1.5 mL formic acid and differing amounts of water ranging between 0.4 and 1.5 mL. Materials synthesised with 0.4 mL and 0.8 mL of water showed only the **fcu** phase, however the XRPD patterns showed that when 1.2 mL and 1.5 mL of water is added to the synthesis mixture, the phase of the material changed. The growth of a small peak around 6.8 °

and a shoulder on the left of the main peak indicated the partial formation of the **hcp** phase, something seen in previous publications.¹⁹

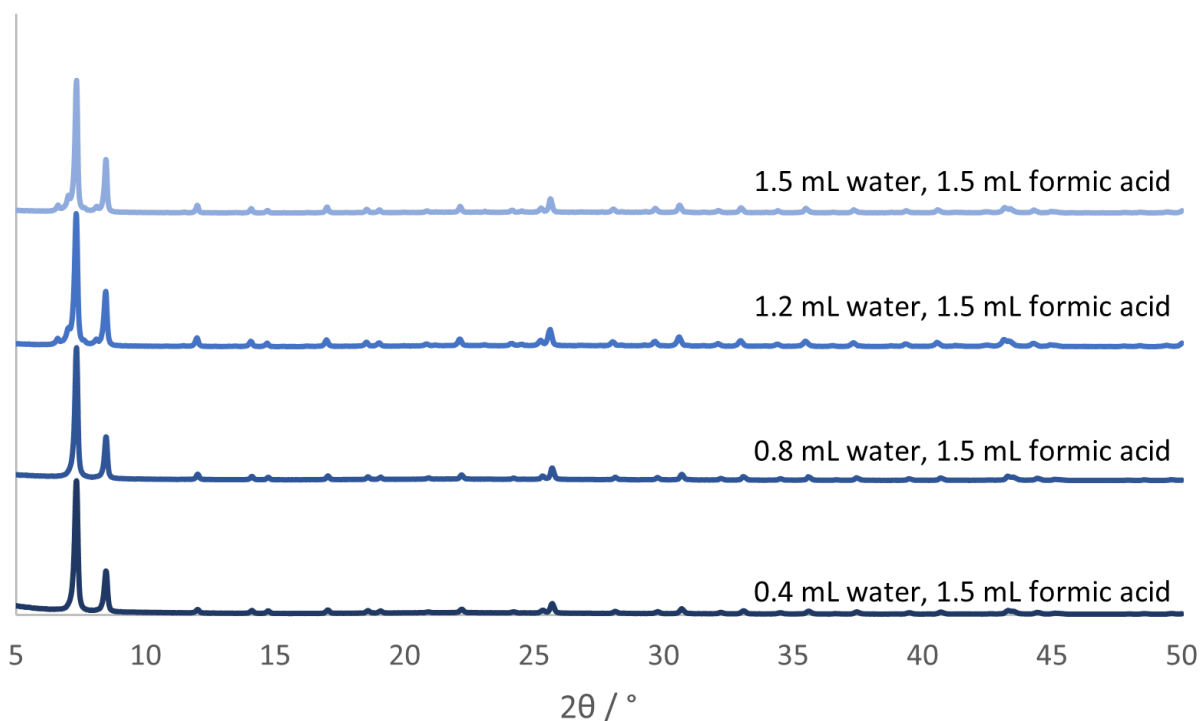


Figure 2.10. Stacked PXRD patterns for $Zr_6(NH_2BDC)$ synthesised with 1.5 mL formic acid and increasing volumes of water.

The same incremental volume increase for water was used when the formic acid volume was increased to 2 mL. Figure 2.11 shows the stacked PXRD patterns of $Zr_6(NH_2BDC)$ synthesised with 1.5 mL formic acid and differing amounts of water. In these patterns, none of the synthesised materials show purely the **fcu** phase. The additional peak at 6.8° is visible in all of the samples prepared with 2 mL of formic acid. The sample prepared with 0.4 mL water and 2 mL formic acid has the most pronounced growth of the additional peak, this sample was taken forward for exfoliation. However, sonication in a variety of solvents and frequencies did not yield any nanosheet material.

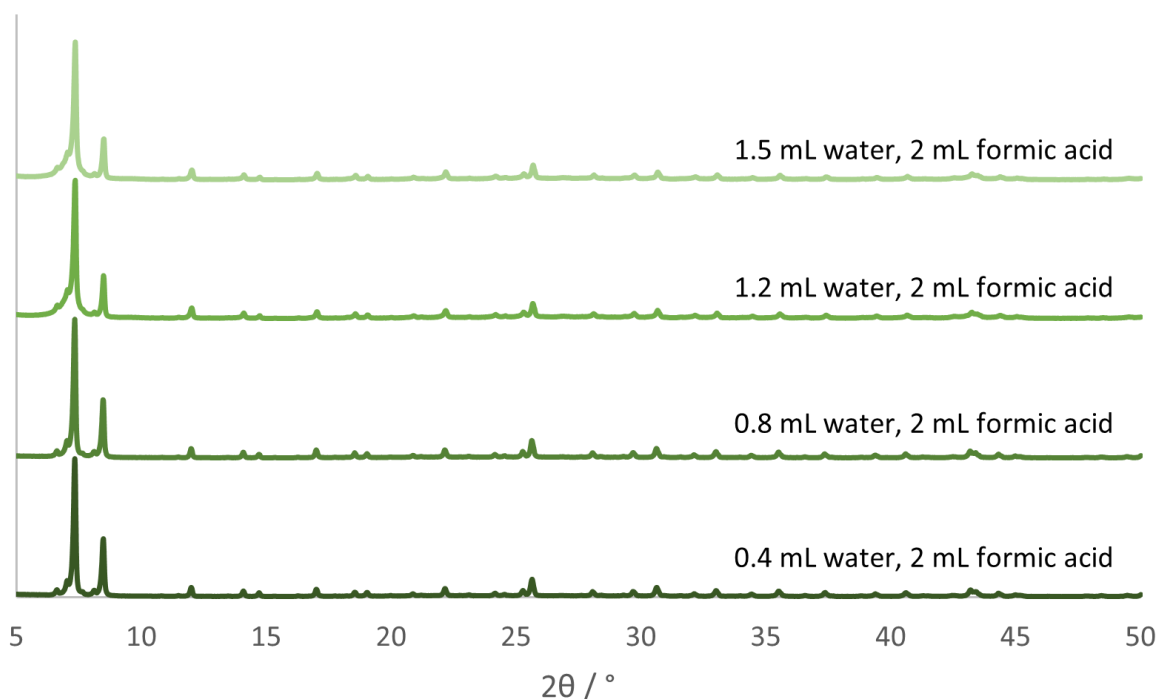


Figure 2.11. Stacked PXRD patterns of $Zr_6(NH_2BDC)$ synthesised with 2 mL formic acid and increasing volumes of water.

After the lack of success with a system using purely NH_2BDC as the linker, a combined approach using F_4BDC and NH_2BDC as co-linkers was applied. Figure 2.12 shows the stacked PXRD patterns of $Zr_6(NH_2:F_4BDC)$ with increasing NH_2BDC linker inclusions. When NH_2BDC is included during synthesis at 10 – 40 % there is minimal change in the PXRD compared to the original **fcu** phase. Once the inclusion percentage of NH_2BDC reaches 50%, there is a clear shift in the PXRD pattern from mostly **fcu** with the small peaks at 6.8° seen in both Figure 2.10 and Figure 2.11, to a mixed phase system. The large peak around 7° is split into two peaks, the right from the original **fcu** phase and the left due to the formation of the **hcp** phase. This synthesis was successfully repeated multiple times to ensure it was not an anomaly. Speculatively this could be explained by the ratio of 50:50 $F_4BDC:NH_2BDC$ creating some ordering during the synthesis that allows the formation of the mixed **fcu-hcp** phase.

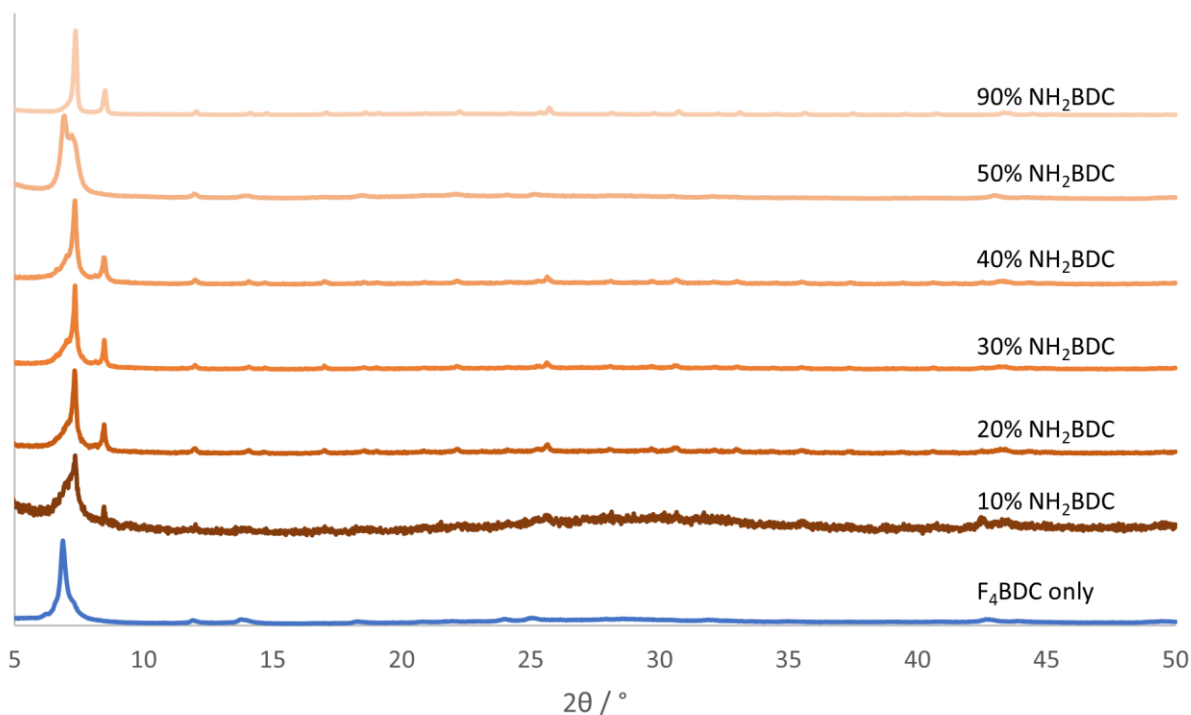


Figure 2.12. Stacked PXRD patterns showing increasing amounts of NH₂BDC included in Zr₆(NH₂:F₄BDC).

The ratios of linkers added into the synthesis can be different from the actual composition of the product therefore proton nuclear magnetic resonance (¹H NMR) spectroscopy was carried out on the 50 % NH₂BDC sample to ascertain the actual linker ratios. As F₄BDC has no protons after the addition of acid required to digest the MOF, a tetramethyl silane (TMS) standard was used to calculate the amount of NH₂BDC present in the structure. Figure 2.13 shows the region of the H¹ NMR spectrum where the amino protons are present, the inset shows the whole spectrum. The TMS standard has been normalised according to the preparation concentration. At 7.51 ppm, the singlet and doublet assigned to DMF and proton H_b are overlapping and therefore integration of this peak does not reflect the concentration of H_b protons present. Peaks at 7.73 ppm and 7.48 ppm correspond to H_a and H_c on the annotated NH₂BDC ligand. Integration of these peaks against the normalised TMS peak shows that NH₂BDC was included in the final product at 64 %.

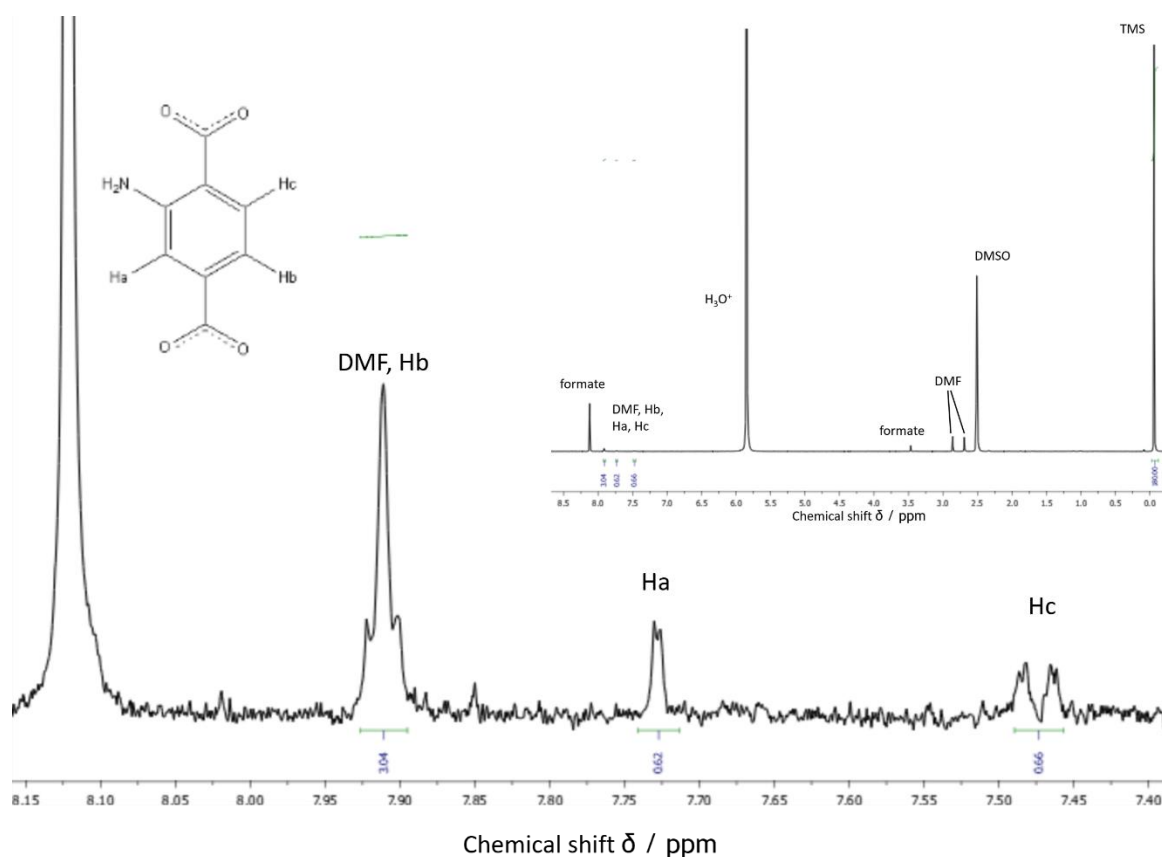


Figure 2.13. Annotated ^1H NMR spectrum of $\text{Zr}_6(\text{F}_4\text{BDC}:\text{NH}_2\text{BDC})$ after acid digestion with 50 μL HCl (35 %).

The sample with 64% inclusion of NH_2BDC was then exfoliated via sonication in a range of solvents, frequencies and for a range time. The ultrasonic bath used for exfoliation can operated at either 37 kHz or 80 kHz, previous studies within the Foster group investigating exfoliation of MONs had found that 80 kHz for 1 h followed by centrifugation at 1500 rpm produced the best results, so this was taken as the starting point.²³

Figure 2.14 shows AFM topological profiles of $\text{Zr}_6(\text{NH}_2:\text{F}_4\text{BDC})$ after exfoliation with ultrasound at 80 Hz for 30 min, 60 min and 12 h in ethanol, acetonitrile, water, and acetone. As seen in Figure 2.14, AFM images of the resulting supernatants produced materials with thicknesses ranging from 65 – 240 nm. At this frequency, none of the conditions shown in Figure 2.14 yielded MONs, indicating that 80 Hz was not providing enough energy to peel apart the layers in the $\text{Zr}_6(\text{NH}_2:\text{F}_4\text{BDC})$ system.

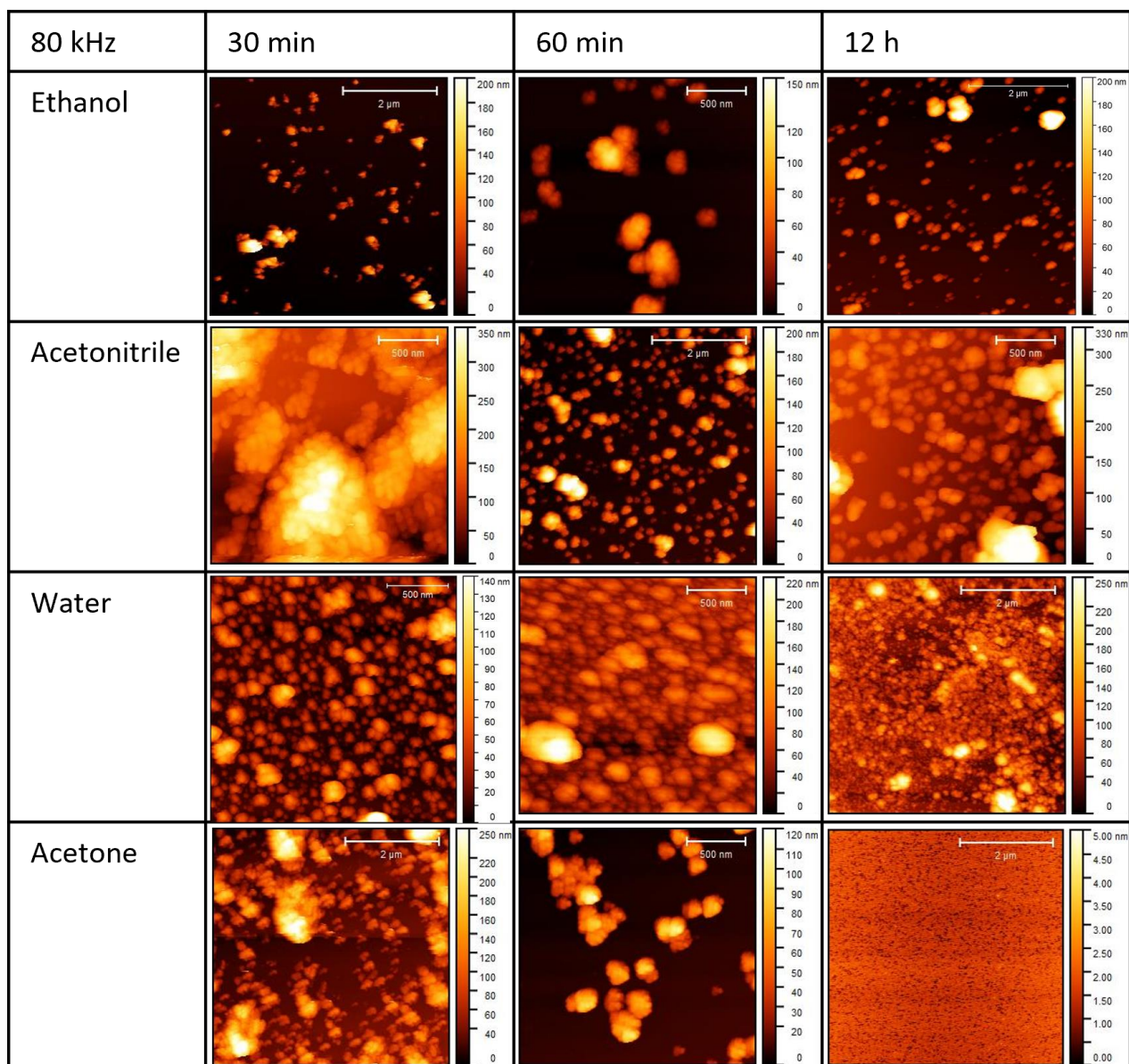


Figure 2.14. AFM topological profiles of $Zr_6(NH_2-F_4BDC)$ sonicated at 80 kHz in ethanol, acetonitrile, water, and acetone for 30 min, 60 min and 12 h.

The same solvent and time variables were then used to sonicate the samples at 37 kHz (see Figure 2.15). This set of experiments showed that $Zr_6(NH_2:F_4BDC)$ yielded monolayer nanosheets when exfoliated at 37 kHz, in ethanol (EtOH) for 12 hours. As no other solvent system tried produced nanosheets, the combination of the solvent interactions between ethanol and $Zr_6(NH_2:F_4BDC)$ and the higher energy provided by the ultrasonic bath at 37 kHz must form the ideal conditions to peel apart the layers in the $Zr_6(NH_2:F_4BDC)$ system. Sonication conditions (37 kHz, 12 h, EtOH) were used for all exfoliations of $Zr_6(NH_2:F_4BDC)$ going forward.

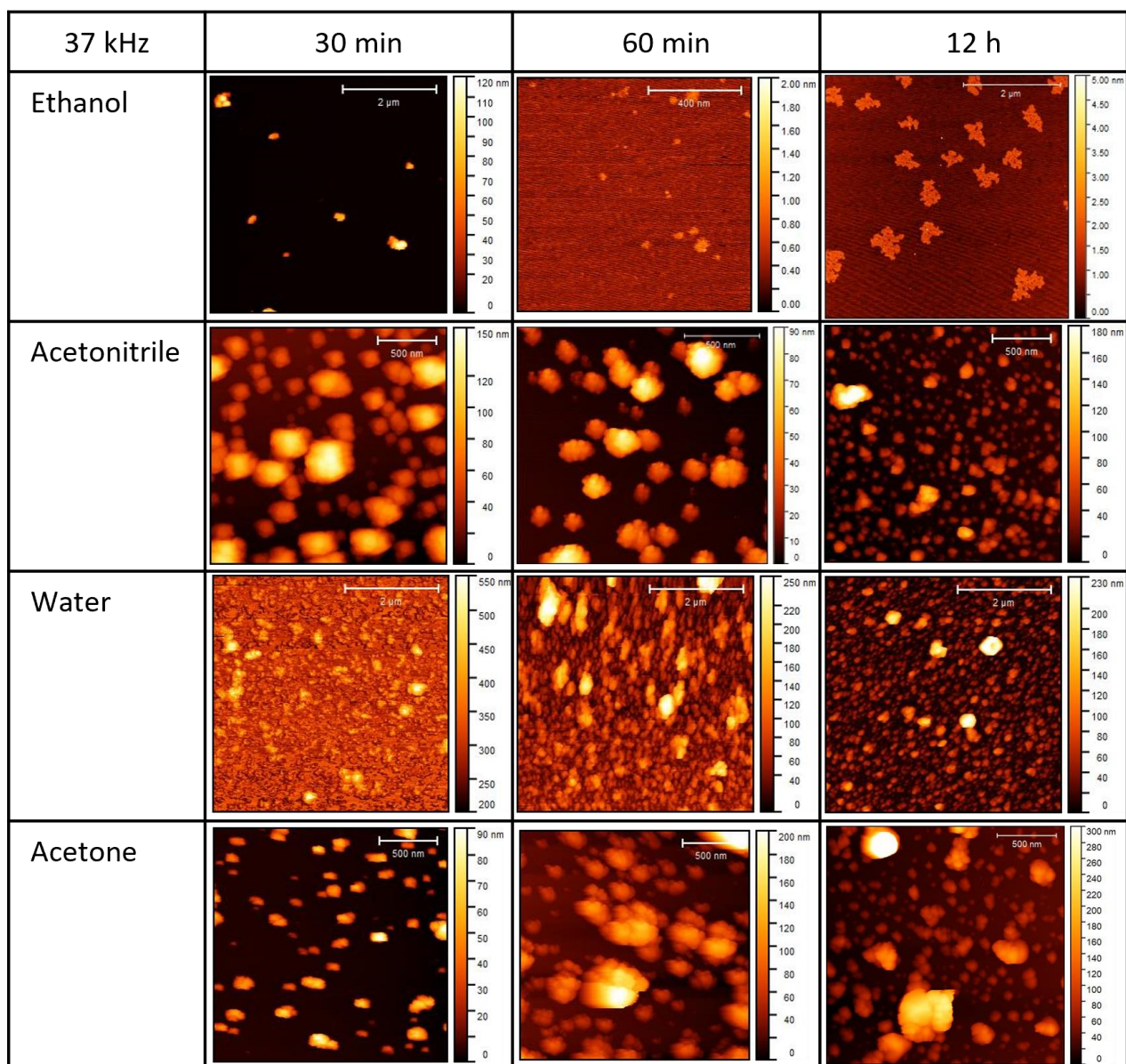


Figure 2.15. AFM topological profiles of $Zr_6(NH_2-F_4BDC)$ sonicated at 37 kHz in ethanol, acetonitrile, water, and acetone for 30 min, 60 min and 12 h.

A closer look at the AFM topological profiles measured for $Zr_6(NH_2:F_4BDC)$ (Figure 2.16), shows that on average, nanosheets are 419 nm in lateral size, and 1.6 nm thick. This is consistent with the expected thickness based on the height of the zirconium cluster in the crystal structure for the $Zr_6(F_4BDC)$ MOF (1.7 nm). Small holes can be seen in the $Zr_6(NH_2:F_4BDC)$ nanosheets, it is likely that these come from the use of a modulating agent (formic acid) in the synthesis. The modulating agent generally creates defects in the formation of the 3D MOF within the (111) plane of the MOF parent, causing the formation of the hexagonal **hcp** structure.¹⁹ It is likely that a combination of the modulator

and harsh exfoliation conditions cause missing linker defects within the plane, resulting in holes in the surface of the nanosheets.

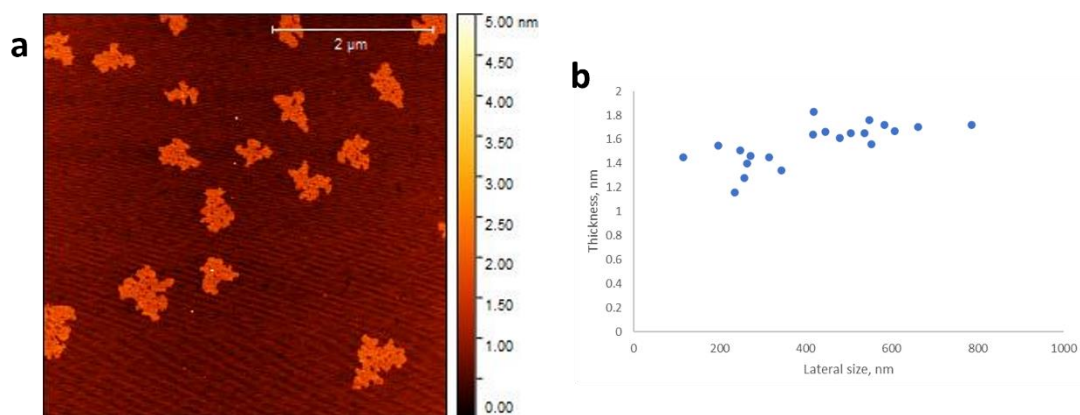


Figure 2.16. (a) AFM topological profiles of $Zr_6(NH_2:F_4BDC)$ sonicated at 37 kHz in ethanol for 12 h and (b) plot of corresponding height profiles.

Comparing these NH_2BDC and F_4BDC mixed linker MONs to the F_4BDC only MONs (see Figure 2.17), overall, the nanosheets for both systems are relatively similar. Both average lateral sizes of 400-600 nm and thicknesses of 1.6-2.4 nm. Both systems have uneven shaped nanosheets, likely owing to the fact they exfoliate from an interpenetrated flower-like structure seen in the SEM images (Figure 2.5), rather than a purely layered material.

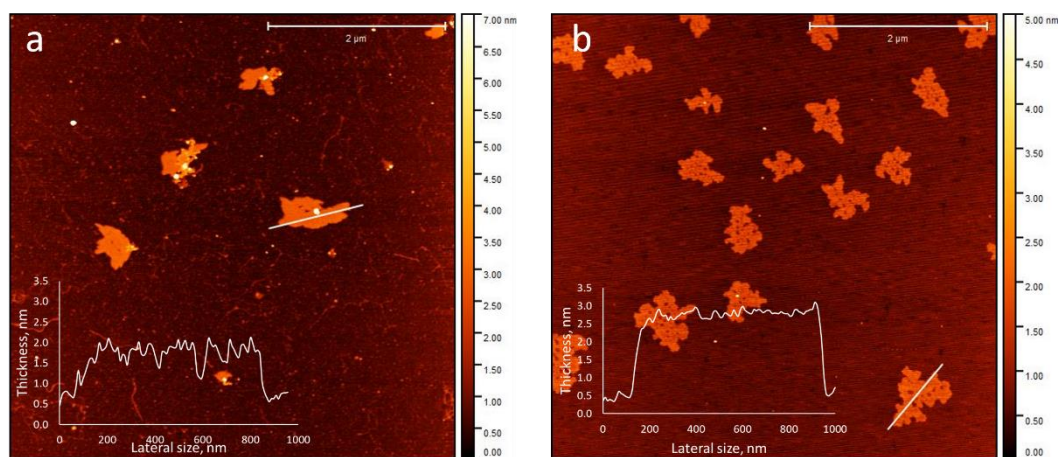


Figure 2.17. AFM topological profiles of (a) $Zr_6(F_4BDC)$ and (b) $Zr_6(NH_2:F_4BDC)$, inset height profiles.

After exfoliation, the sample of $Zr_6(NH_2:F_4BDC)$ nanosheets were dried and analysed by PXRD to evaluate if the sonication step had changed the structure from a mixed phase system to a single phase (Figure 2.18).

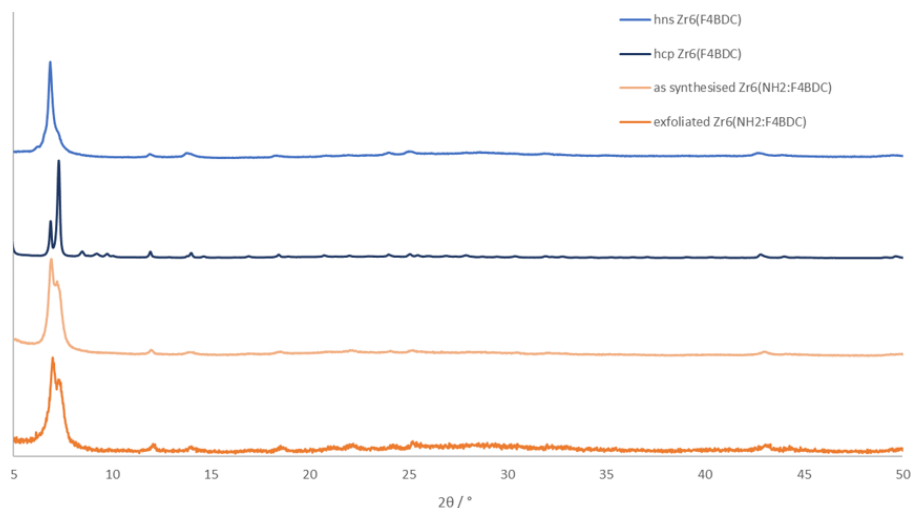


Figure 2.18. PXRD patterns of the nanosheet (hns) phase of $Zr_6(F_4BDC)$ (light blue), hcp phase of $Zr_6(F_4BDC)$ (dark blue), as synthesised $Zr_6(NH_2:F_4BDC)$ (light orange) and $Zr_6(NH_2:F_4BDC)$ after exfoliation via ultrasound at 37 Hz in ethanol for 12 h (dark orange).

As Figure 2.18 shows, the phase of the material did not change with sonication, despite there being clear evidence in the AFM analysis that there were nanosheets present in the suspension. It is likely that, even after sonication there was still some **hcp** phase present, additionally some stacking of the nanosheets is likely to have occurred during the drying process which will add to the presence of this mixed phase in the PXRD pattern.

When looking at DLS analysis of sonicated $Zr_6(NH_2:F_4BDC)$ (Figure 2.19), measurements taken of the whole suspension (bulk) have a single peak with a distinct “hump” on the side (orange). Samples of exfoliated $Zr_6(NH_2:F_4BDC)$ were centrifuged (1500 rpm, 20 min) do not exhibit this “hump”. Centrifugation removes particles by mass rather than lateral size, therefore it is likely that the “hump” removed in the centrifuged MONs only sample is due to small dense particles of **hcp** $Zr_6(NH_2:F_4BDC)$. The MON only peak corroborated the size analysis from the AFM data, that show that the average size of these $Zr_6(NH_2:F_4BDC)$ MONs was approximately 418 nm (Figure 2.16).

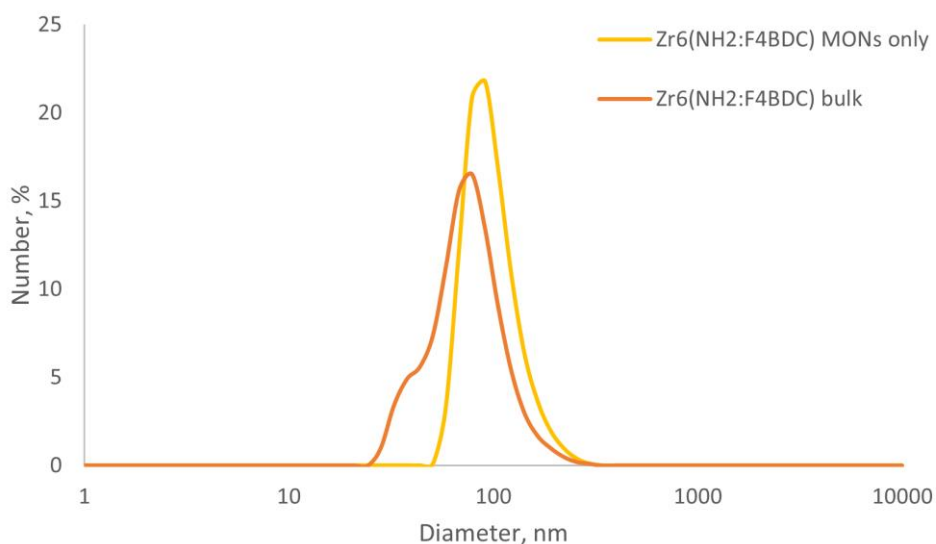


Figure 2.19. DLS number plots for suspensions of $Zr_6(NH_2:F_4BDC)$ bulk material (orange), and $Zr_6(NH_2:F_4BDC)$ after centrifugation to give MONs only (yellow).

2.2.3. Synthesis and characterisation of $Zr_6(BDC)$ and $Zr_6(BrBDC)$

The original synthesis for UiO-66 reported by F. C. N. Firth *et al.* used terephthalic acid (H_2BDC) and yielded a 3D MOF.^{1,19} By applying the defect mediated approach used to synthesise $Zr_6(F_4BDC)$ and $Zr_6(NH_2:F_4BDC)$ MONs, it was hoped to access the **hcp** phase of $Zr_6(BDC)$ and exfoliate this system into 2D nanosheets. Additionally, 1-bromo terephthalic acid ($BrBDC$) was readily available, so the defect mediated synthesis of $Zr_6(BDC)$ and $Zr_6(BrBDC)$ MONs was also attempted. The use of different ligands could affect the topology, dimensions or surface properties of the MONs and could open up the systems for different applications.

The same general synthesis procedure used to synthesise $Zr_6(F_4BDC)$ was followed in attempts to synthesise $Zr_6(BDC)$ and $Zr_6(BrBDC)$. $ZrCl_4$ and either H_2BDC or $BrBDC$ were added in equimolar ratios to a mixture of DMF, water and formic acid. This was then heated to 120 °C for 24 h before washing with DMF and activation at 200 °C.

As with the initial synthesis screening experiments for $Zr_6(NH_2BDC)$, varying amounts of formic acid and water were included in the synthesis to try achieve the **hcp** phase for both $Zr_6(BDC)$ and $Zr_6(BrBDC)$. Figure 2.20 shows the stacked PXRD patterns recorded for $Zr_6(BDC)$ synthesis with varying water and formic acid inclusions. Samples synthesised with 1.5 mL formic acid and 0.4, 1.2 and 1.5 mL

water, and with 2.0 mL formic acid and 0.4 mL water mostly present the **fcu** phase. Samples synthesised using 2.0 mL formic acid and 0.8, 1.2 and 1.5 mL of water are clearly mixed phase, the peak broadening and lack of definition suggests these samples are amorphous. The sample synthesised using 1.5 mL formic acid and 0.8 mL water shows a clear phase change.

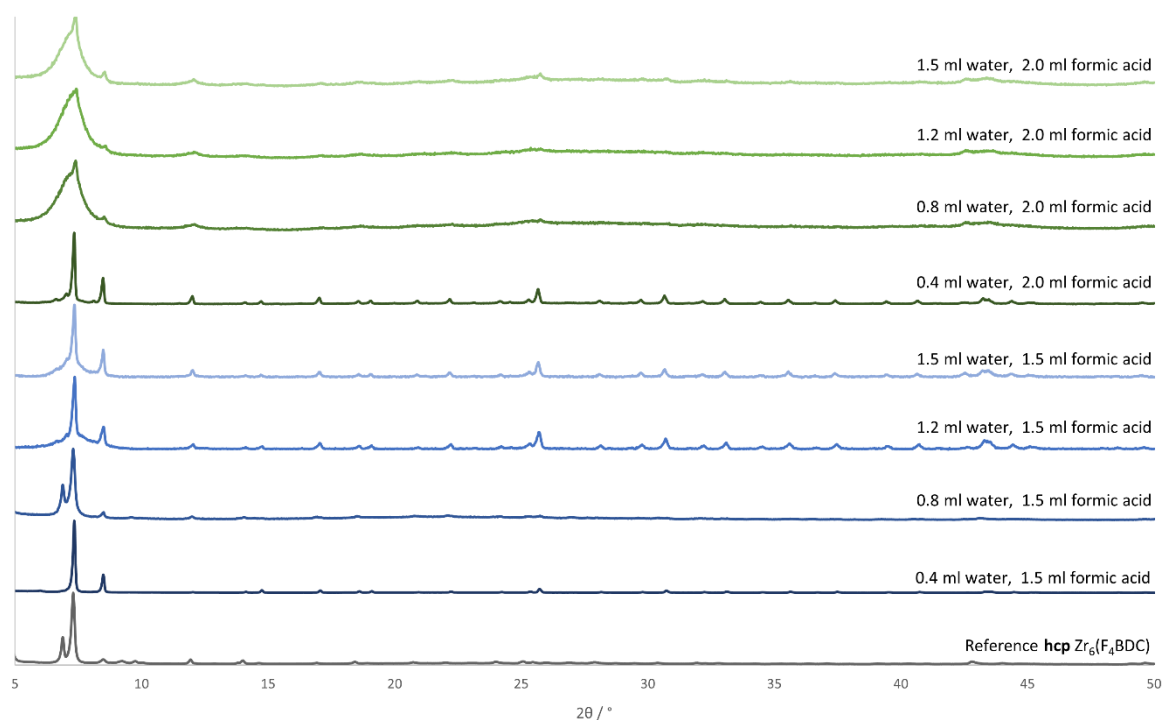


Figure 2.20. Stacked PXRD patterns showing varying amounts of water and formic acid included in the synthesis of $Zr_6(BDC)$.

When 0.8 ml water and 1.5 ml formic acid were added to the synthesis of $Zr_6(BDC)$ the formation of the **hcp** phase at 6.8° can be clearly seen. This indicates the likelihood of being able to access the **hns** phase and exfoliate this sample into nanosheets. Following the successful exfoliation of $Zr_6(NH_2:F_4BDC)$ in ethanol at 37 kHz for 12 hours, the same conditions were used to exfoliate the sample of $Zr_6(BDC)$ prepared using 0.8 ml water and 1.5 ml formic acid. However, no nanosheets were observed when AFM analysis was carried out. SEM images (Figure 2.21) do not show the interpenetrated ball-like structure seen in the **hcp** phase of $Zr_6(F_4BDC)$, but instead agglomerated flat particles with rounded edges.

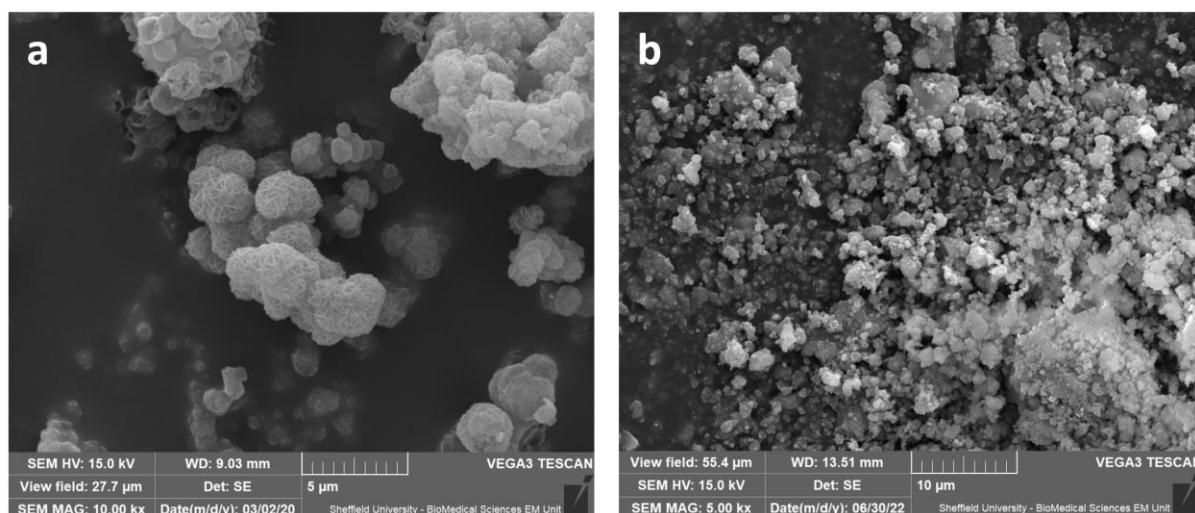


Figure 2.21. SEM image of (a) $Zr_6(F_4BDC)$ and (b) $Zr_6(BDC)$.

Figure 2.22 shows the stacked PXRD patterns recorded for the synthesis of $Zr_6(BrBDC)$ with varying quantities of water and formic acid.

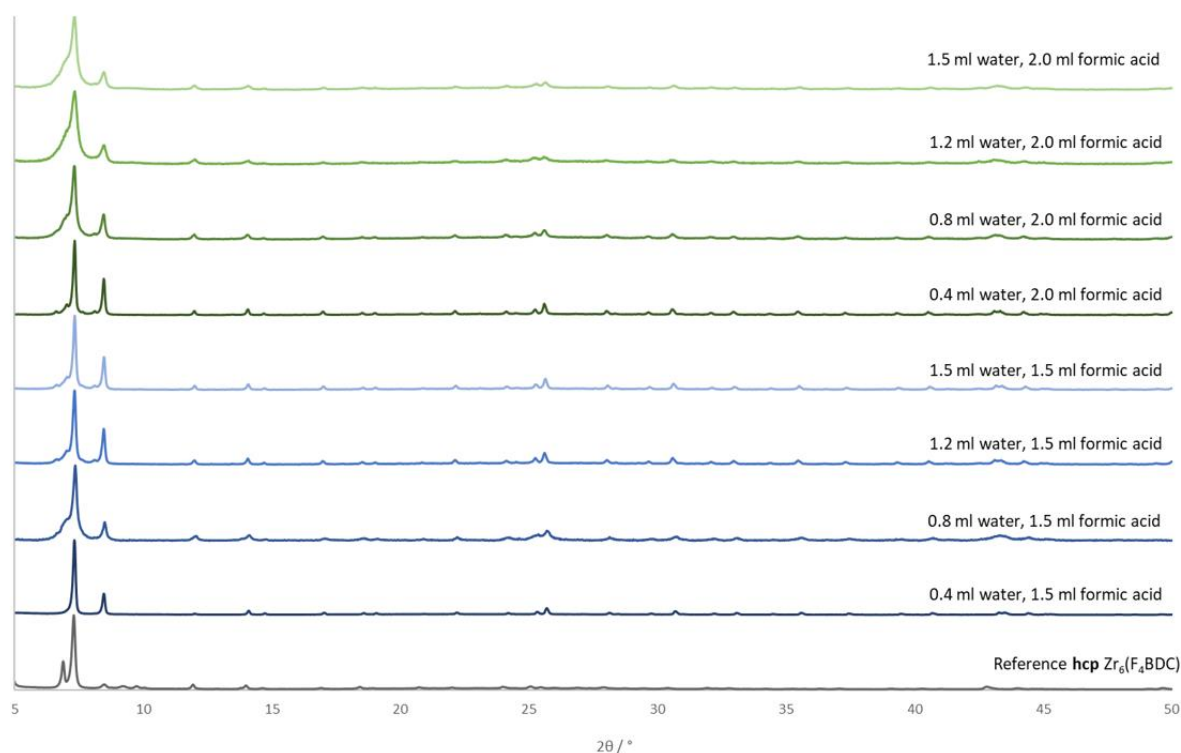


Figure 2.22. Stacked PXRD patterns showing varying amounts of water and formic acid included in the synthesis of $Zr_6(BrBDC)$.

With the exception of the sample synthesised with 0.4 mL water and 1.5 mL formic acid, all of the PXRD patterns show some **hcp** characteristics in the shoulder on the left-hand side of the main peak at 7.3° . The emerging peak around 6.8° that indicates the formation of the **hcp** phase can be seen

most predominantly in the samples prepared with 0.4 ml water and 2.0 ml formic acid, therefore this sample was taken forward for exfoliation (ethanol, 37 kHz, 12 h). Figure 2.23 shows the AFM topological profile and associated height plots for sonicated $Zr_6(BDC)$. As can be seen, the particles of $Zr_6(BDC)$ are between 74 – 234 nm thick and 485 – 791 nm laterally. This is too thick for these particles to be considered nanosheets.

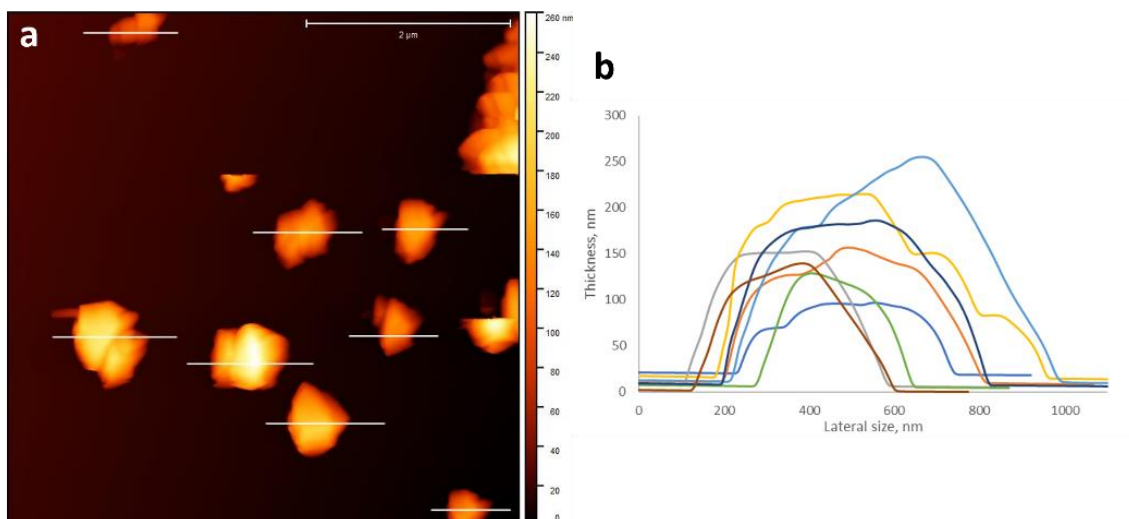


Figure 2.23. (a) AFM topological profile of $Zr_6(BDC)$ and (b) the associated height plots.

As neither the Zr_6BrBDC or Zr_6H_2BDC showed the formation of the **hcp** phase in the PXRD patterns (Figure 2.20 and Figure 2.22), and sonication did not yield nanosheets, these systems were not pursued further.

2.3. Conclusions

In this chapter the synthesis of four MONs based on analogues of UiO-66 were attempted, one already reported and three novel systems. Synthesis of $Zr_6(F_4BDC)$ was successfully repeated and a more in-depth characterisation of the nanosheets than previously reported was undertaken. Due to the observed stability of these nanosheets in water, these MONs were taken forward for the use in water purification membranes, discussed in **Chapter 3**.

Systematic studies of the defect-mediated synthesis of $Zr_6(NH_2BDC)$, $Zr_6(BDC)$ and $Zr_6(BrBDC)$ were performed, changing the quantities of water and formic acid as modulating agents with limited success

in producing **hcp** phase material and nanosheets. While these synthesis routes did not yield the desired crystal phase, there are many other factors in the synthesis method that could be considered, such as temperature and pH for future research.

Mixed-ligand synthesis of $Zr_6(NH_2:F_4BDC)$ was successfully carried out. A 50:50 mixture of NH_2BDC and F_4BDC was found to be the ideal conditions to synthesise mixed-phase **hcp** $Zr_6(NH_2:F_4BDC)$, with inclusion at 64 % found in the final product. A systematic study of exfoliation conditions showed that 12 h in ethanol at 37 Hz yielded monolayer nanosheets comparable to the original $Zr_6(F_4BDC)$ nanosheets investigated from the reported synthesis. This is a promising result as the inclusion of amino functionality opens up these MONs for potential post-synthetic functionalisation experiments, whereby an even wider range of functional groups can be introduced into the structure. The mixed linker system is also a synthetic route that could be investigated with for the previously discussed ligands. The mixed ligand composition and the monolayer structure of these $Zr_6(NH_2:F_4BDC)$ MONs could lead to their suitability for a wide range of applications such as tandem catalysis and separation membranes.

Overall, this chapter introduced the ability to use modulators in defect-mediated synthesis to develop new MONs with traditionally non-layered MOFs. The synthesis and characterisation of $Zr_6(F_4BDC)$ MONs was successfully carried out, with these MONs being taken forward for investigation in water purification membranes (**Chapter 3**). This chapter also demonstrated the utility of mixed linker synthesis with the creation of novel monolayer nanosheets of $Zr_6(NH_2:F_4BDC)$. Further research into synthesising phase pure **hcp** UiO-66 analogues using ligands discussed above and other functionalised benzene dicarboxylic acid ligands is needed. Additionally further work on mixed ligand UiO-66 analogues and the affect this has on the structures is required to fully understand the full potential of the 2D analogues of UiO-66 frameworks. The extensive range of benzene dicarboxylic acid based linkers available, and the post-synthetic functionalisation techniques could lead to a wide range of 2D

UiO-66 materials. Which, combined with their inherent stability could be used for a vast array of applications.

2.4. References

- 1 J. H. Cavka, S. Jakobsen, U. Olsbye, N. Guillou, C. Lamberti, S. Bordiga and K. P. Lillerud, *J. Am. Chem. Soc.*, 2008, **130**, 13850–13851.
- 2 J. Winarta, B. Shan, S. M. McIntyre, L. Ye, C. Wang, J. Liu and B. Mu, *Cryst. Growth Des.*, 2020, **20**, 1347–1362.
- 3 M. Ding, X. Cai and H. L. Jiang, *Chem. Sci.*, 2019, **10**, 10209–10230.
- 4 A. J. Howarth, Y. Liu, P. Li, Z. Li, T. C. Wang, J. T. Hupp and O. K. Farha, *Nat. Rev. Mater.*, 2016, **1**, 1–15.
- 5 D. Ma, G. Han, S. B. Peh and S. B. Chen, *Ind. Eng. Chem. Res.*, 2017, **56**, 12773–12782.
- 6 D. L. Zhao, W. S. Yeung, Q. Zhao and T. S. Chung, *J. Memb. Sci.*, 2020, **604**, 118039.
- 7 T. Mu, Y. Zhang, W. Shi, G. Chen, Y. Liu and M. Huang, *Chemosphere*, 2021, **269**, 128686.
- 8 S. Y. Fang, P. Zhang, J. L. Gong, L. Tang, G. M. Zeng, B. Song, W. C. Cao, J. Li and J. Ye, *Chem. Eng. J.*, 2020, **385**, 123400.
- 9 F. Xiao, M. Cao, R. Chu, X. Hu, W. Shi and Y. Chen, *J. Colloid Interface Sci.*, 2022, **610**, 671–686.
- 10 Y. Liu, D. Gan, M. Chen, L. Ma, B. Yang, L. Li, M. Zhu and W. Tu, *Sep. Purif. Technol.*, 2020, **253**, 117552.
- 11 H. Li, Y. Yin, L. Zhu, Y. Xiong, X. Li, T. Guo, W. Xing and Q. Xue, *J. Hazard. Mater.*, 2019, **373**, 725–732.
- 12 X. Zhu, Z. Yu, H. Zen, X. Feng, Y. Liu, K. Cao, X. Li and R. Long, *J. Appl. Polym. Sci.*, 2021, **138**, 50765.
- 13 X. Wang, L. Zhai, Y. Wang, R. Li, X. Gu, Y. Di Yuan, Y. Qian, Z. Hu and D. Zhao, *ACS Appl. Mater. Interfaces*, 2017, **9**, 37848–37855.
- 14 X. Liu, N. K. Demir, Z. Wu and K. Li, *J. Am. Chem. Soc.*, 2015, **137**, 6999–7002.
- 15 L. Wan, C. Zhou, K. Xu, B. Feng and A. Huang, *Microporous Mesoporous Mater.*, 2017, **252**, 207–213.
- 16 Y. Yang, K. Goh, R. Wang and T. H. Bae, *Chem. Commun.*, 2017, **53**, 4254–4257.
- 17 E. M. Dias and C. Petit, *J. Mater. Chem. A*, 2015, **3**, 22484–22506.
- 18 M. J. Cliffe, E. Castillo-Martínez, Y. Wu, J. Lee, A. C. Forse, F. C. N. Firth, P. Z. Moghadam, D. Fairen-Jimenez, M. W. Gaultois, J. A. Hill, O. V. Magdysyuk, B. Slater, A. L. Goodwin and C. P. Grey, *J. Am. Chem. Soc.*, 2017, **139**, 5397–5404.
- 19 F. C. N. Firth, M. J. Cliffe, D. Vulpe, M. Aragonés-Anglada, P. Z. Moghadam, D. Fairen-Jimenez, B. Slater and C. P. Grey, *J. Mater. Chem. A*, 2019, **7**, 7459–7469.
- 20 L. Cao, Z. Lin, F. Peng, W. Wang, R. Huang, C. Wang, J. Yan, J. Liang, Z. Zhang, T. Zhang, L. Long, J. Sun and W. Lin, *Angew. Chemie - Int. Ed.*, 2016, **55**, 4962–4966.
- 21 S. Mandal, S. Natarajan, P. Mani and A. Pankajakshan, *Adv. Funct. Mater.*, 2021, **31**, 2006291.
- 22 J. López-Cabrelles, S. Mañas-Valero, I. J. Vitorica-Yrezábal, P. J. Bereciartua, J. A. Rodríguez-Velamazán, J. C. Waerenborgh, B. J. C. Vieira, D. Davidovikj, P. G. Steeneken, H. S. J. van der Zant, G. Mínguez Espallargas and E. Coronado, *Nat. Chem.*, 2018, **10**, 1001–1007.

- 23 D. J. Ashworth, A. Cooper, M. Trueman, R. W. M. M. Al-Saedi, L. D. Smith, A. J. H. M. Meijer, J. A. Foster, S. D. Liam, A. J. H. M. Meijer and J. A. Foster, *Chem. - A Eur. J.*, 2018, **24**, 17986–17996.

Chapter 3

Preparation and water purification performance of $Zr_6(F_4BDC)$ membranes

3.1. Introduction

The UiO-series of MOFs have been repeatedly shown to have exceptional water stability.¹ The strong Zr-O bond accounts for this high stability, with studies showing that the carbon-carbon bonds within the ligand break down before the coordination bond.^{2,3} It is likely that it is for this reason that UiO MOFs have the highest incidence of research papers reporting MOF membranes for water purification (Figure 1.7).

UiO-66 and UiO-66-NH₂ have both been incorporated into a variety of membranes using a range of preparation techniques. The majority of the UiO- membrane papers report the use of polymeric supports, including but not limited to; polysulfone, polyvinylidene fluoride and cellulose based membranes.⁴⁻⁷ There are also a number of examples of the use of polyamide membranes, which are prepared using interfacial polymerisation, a technique whereby the MOF is added to a monomer solution in order to incorporate it into the fabrication of the polymer.⁸⁻¹⁰ The two other most prevalent preparation techniques for MOF-membranes are vacuum filtration and casting. The former being the method used in this work, where a MOF is deposited on the surface of the membrane via the filtration of a suspension.¹¹ Casting is a process where the MOF suspension is spread over the support membrane using a knife or bar.¹² Figure 3.1 shows schematic illustrations and SEM images of a range of UiO-based membranes prepared using different methods.

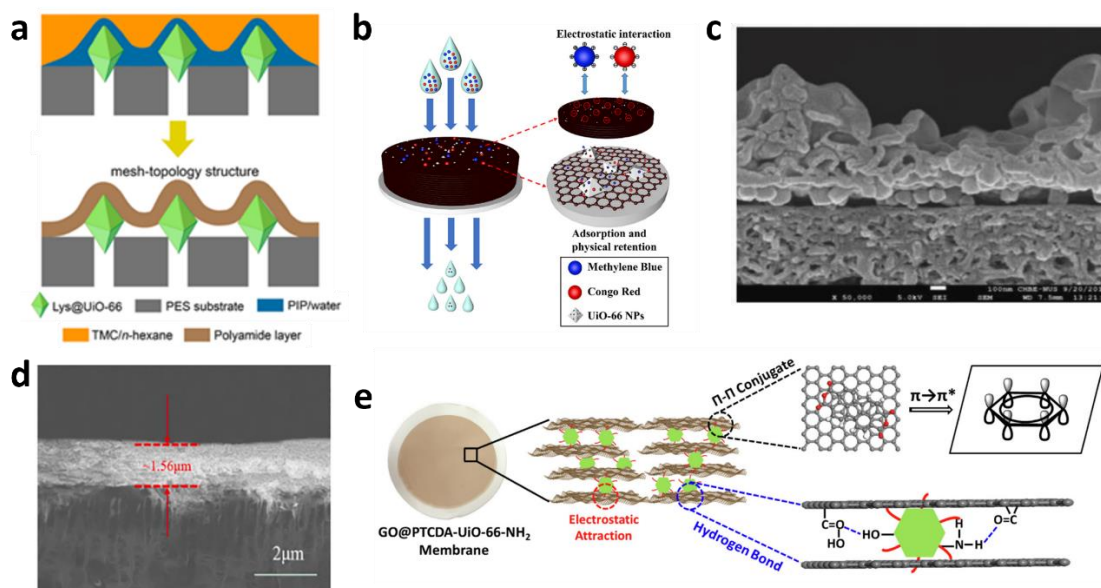


Figure 3.1. (a) schematic showing the mesh-topology structure when lysine modified UiO-66 is incorporated into polyamide membranes, (b) schematic showing the mechanism of separation in graphene oxide-UiO-66 composite membranes, (c) cross-sectional SEM image of UiO-66-NH₂ incorporated into a polyamide composite, (d) cross-sectional SEM image of UiO-66 deposited on the surface of a polyacrylonitrile membrane and (e) schematic showing the formation mechanism of a graphene oxide- perylene-3, 4, 9, 10-tetracarboxylic dianhydride(PTCDA)-UiO-66-NH₂ composite membrane. Figures reproduced from references 13, 11, 9, 14 and 6 respectively.

In general, UiO-membranes prepared with polyamides are used for desalination applications, this is likely due to the dense, non-porous structure of polyamides that allows the removal of salt ions via a solution diffusion mechanism.^{10,15} The addition of lysine modified UiO-66 into a polyamide membrane has been shown to enhance the permeability by 55 % while maintaining the high salt rejection (98 %).¹³ For UiO- membranes prepared with other, more porous polymers, a wide range of different filtrates have been tested, for example antibiotics,^{4,14} organic dyes,^{6,11} and oil/water.^{16,17} The majority of these literature examples exhibit very high rejections of over 90% and a number have stability studies showing excellent long term performance.^{5,18,19} Both permeance and selectivity enhancement upon UiO- MOF addition have been reported.^{11,19} Additionally the tunable porous nature of the UiO-system offers the potential for selectivity control in separation applications.^{5,18,20}

While these 3D UiO-66 MOFs have been shown to be successful in water purification membranes, there is evidence to show that 2D MONs can not only improve the water transport through the membrane due to reduced thickness, but also enhance compatibility with the membrane itself.^{21,22} 2D MONs offer atomic thickness, flexibility and tunable surface chemistries to membrane technology that

their 3D counterparts cannot. **Chapter 2** reported the synthesis of two-dimensional $Zr_6(F_4BDC)$ nanosheets and other novel UiO-analogues gave motive for using 2D UiO- based MONs in initial membrane preparation and testing experiments.

In **Chapter 2**, a series of 2D UiO-66 analogues were synthesised, of which UiO-66(F_4BDC) ($Zr_6(F_4BDC)$) formed the most promising nanosheets with average thickness and lateral dimensions of 2.4 nm and 593 nm respectively. The following work explores the use $Zr_6(F_4BDC)$ MONs deposited on commercial polyethersulfone (PES) membranes for water purification. The chapter investigates the affect that polymer additives and different loadings of MON and additive have on the ability of the membranes to remove organic dyes from water. Additionally, different PES supports and the removal of bulk material from the MON suspension prior to membrane preparation are tested to see if they improve performance of the MON-membrane system. A key focus of this chapter is development of the method for MON-membrane preparation and testing as these techniques had not previously been used in the Foster group. Although the ultimate performance of the membranes was below what was aimed for, a lot of useful lessons about membrane loading, the role of additives and reproducibility in membrane testing were learnt, which are then applied in later chapters.

3.2. Results and discussion

3.2.1. Pristine PES membrane

Polyether sulfone (PES) membranes (47 mm, 30 nm pore size) purchased from Sterlitech were used as a support for the vacuum deposition of MONs in the preparation of MON-membranes. As a reference for the performance of MON-membranes, pristine PES was tested with a solution of brilliant blue G dye (10 mg L^{-1}). PES reference membranes were tested in a stirred dead-end cell. Three repeats were carried out. Figure 3.2 shows the average percentage rejection and permeance data (and associated standard deviation error) for the pristine PES membranes. The PES membranes show an average rejection of 16 % and permeance of $6446 \text{ L m}^{-2} \text{ h}^{-1} \text{ bar}^{-1}$ (LMHB) over the duration of the test.

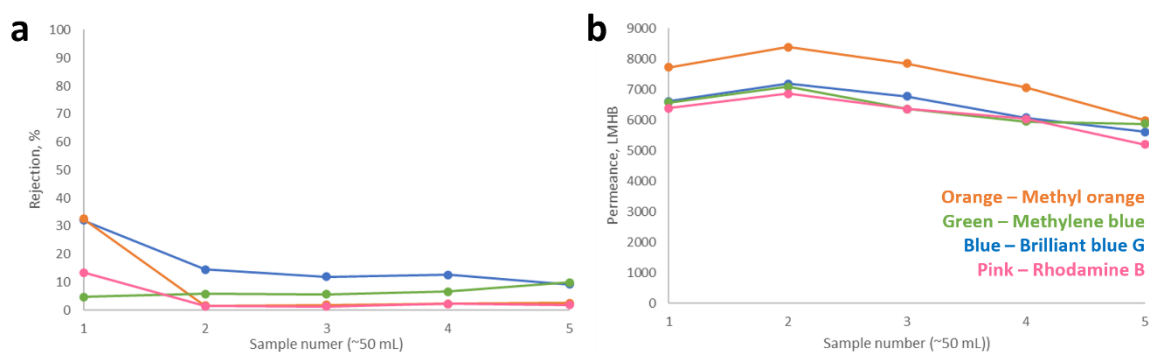


Figure 3.2. (a) Percentage rejection and (b) permeance data for pristine PES membranes tested with brilliant blue G dye.

3.2.2. $Zr_6(F_4BDC)$ membranes on PES supports

In order to evaluate the water purification ability of $Zr_6(F_4BDC)$ nanosheets developed in **Chapter 2**, $Zr_6(F_4BDC)$ MONs were deposited onto polyethersulfone (PES) support membranes. A method outlined in the first reported instance of metal-organic nanosheets in water purification membranes was used as the basis for the preparation of $Zr_6(F_4BDC)$ membranes.²³ Commercial PES membranes were suggested as the support membrane by industrial partners Evove. Suspensions of $Zr_6(F_4BDC)$ (1 mg ml^{-1}), in water, were further diluted with 70 mL water before depositing on PES support membranes via vacuum filtration. Previously, vigorous shaking of $Zr_6(F_4BDC)$ in water gave evidence of nanosheets, so no additional exfoliation was used (**Chapter 2 Section 2.2.1**). PES supports (47 mm diameter) with an average pore size of $0.2 \mu\text{m}$ were used unless otherwise stated. These membranes are referred to as $Zr_6(F_4BDC)$ membranes throughout this chapter.

Membranes were assembled into a Sterlitech HP4750 Stirred Cell for dead-end cell filtration testing. The test was carried out using a N_2 stream at 1 bar. Samples were taken at approximately 50 mL intervals for the duration of the test (approx. 250 mL) to understand the progression of the rejection and permeance. The concentration of the filtrate was measured using a UV-Vis spectrometer. Organic dye solutions of methyl orange and brilliant blue G were initially used as the feed to test the membranes. Dyes were prepared at least one day in advance of testing to ensure they were fully dissolved at a concentration of 10 mg L^{-1} (a standard concentration used by colleagues at Evove). Each

membrane was repeated three times to assess variability. Membrane permeance is reported as litres per metre squared per hour per bar (LMHB).

Firstly, membranes were prepared with 1.7 mg of $Zr_6(F_4BDC)$ deposited onto the PES support. This equates to a mass loading of 1000 mg m^{-2} , this loading was chosen as a similar to the loading used to achieve a 100 nm thick active layer by Jia *et al.*²⁴ These membranes were tested with methyl orange. Each membrane was prepared three times for repeat tests to assess the repeatability. Figure 3.3 shows the percentage rejection and permeance results for these membranes. There is negligible rejection of the methyl orange dye at this MON loading. The permeance is very high at an average of 6445 LMHB.

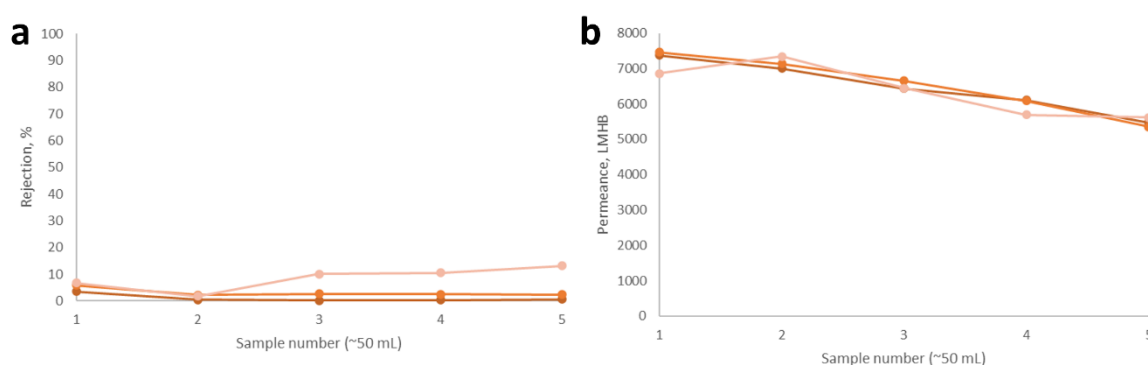


Figure 3.3. (a) Percentage rejection and (b) permeance data for membranes prepared with 1.7 mg $Zr_6(F_4BDC)$ tested with methyl orange dye. Each data series represents a repeat experiment.

Membranes prepared with 1.7 mg $Zr_6(F_4BDC)$ were then tested with brilliant blue G dye. Figure 3.4 shows the percentage rejection and permeance results for these membranes. The rejection starts at a good average of 68 %, however this decreases over the course of the experiment. The permeance also has a general downward trend over the experiment. The variation in the permeance results is very large, with final results ranging from 223 to 4822 LMHB.

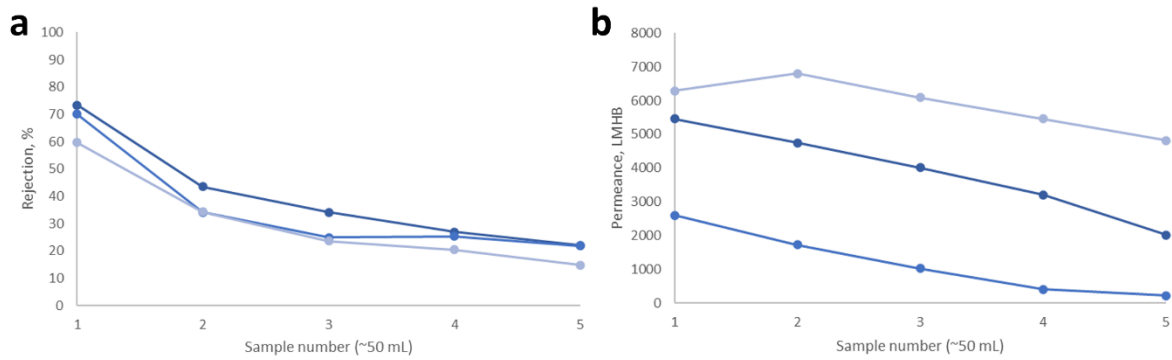


Figure 3.4. (a) Percentage rejection and (b) permeance data for membranes prepared with 1.7 mg $Zr_6(F_4BDC)$, tested with brilliant blue G dye. Each data series represents a repeat experiment.

The rejection drop as the test progressed indicated an adsorptive effect, whereby once active sites on the MON and PES are full of adsorbed dye molecules, the membrane allows more dye to pass through and rejection decreases.²⁵ This is corroborated by the permeance results, as the test progresses, and more dye adsorbs to the membrane, blocking pores, the permeance decreases as the flow of the water is obstructed. Unfortunately, at this mass loading, $Zr_6(F_4BDC)$ only membranes perform poorly.

3.2.3. $Zr_6(F_4BDC)$ /PDDA membranes on PES supports

Ang and Hong reported the use of polydiallyldimethylammonium chloride (PPDA) as a cross-linking agent in MON-membranes.²⁶ They reported significant improvements to rejection when PDDA was incorporated into the membrane. For this reason, PDDA was included in $Zr_6(F_4BDC)$ membranes.

$Zr_6(F_4BDC)$ /PDDA membranes were prepared using a similar method to the $Zr_6(F_4BDC)$ only membranes. MONs were dispersed in 200 mL distilled water, to this suspension a 0.1 wt% aqueous solution of PDDA was also added and briefly mixed. The MON/PDDA mixture was deposited onto the PES support membrane. Both the $Zr_6(F_4BDC)$ and PDDA loadings were varied to identify the optimum membrane composition. Loadings of 0.1, 0.5, and 2 mg of MONs and 0.3, 0.6, 1.5, 10 and 20 mL PDDA solution (0.1 wt%) were chosen for the study to match those used by Jia *et al.* and Ang and Hong.^{23,24} Each membrane was tested with brilliant blue G (10 mg L^{-1}) and repeated three times to evaluate repeatability. To aid clarity, averages rather than individual runs are reported along with

corresponding standard deviation error bars. Figure 3.5 shows the percentage rejection (left) and permeance (right) results for membranes prepared with these $Zr_6(F_4BDC)$ and PDDA loading variations.

Legend: PDDA volumes

Orange – 0.3 mL Yellow – 0.6 mL

Green – 1.5 mL Blue – 10 mL

Purple – 20 mL

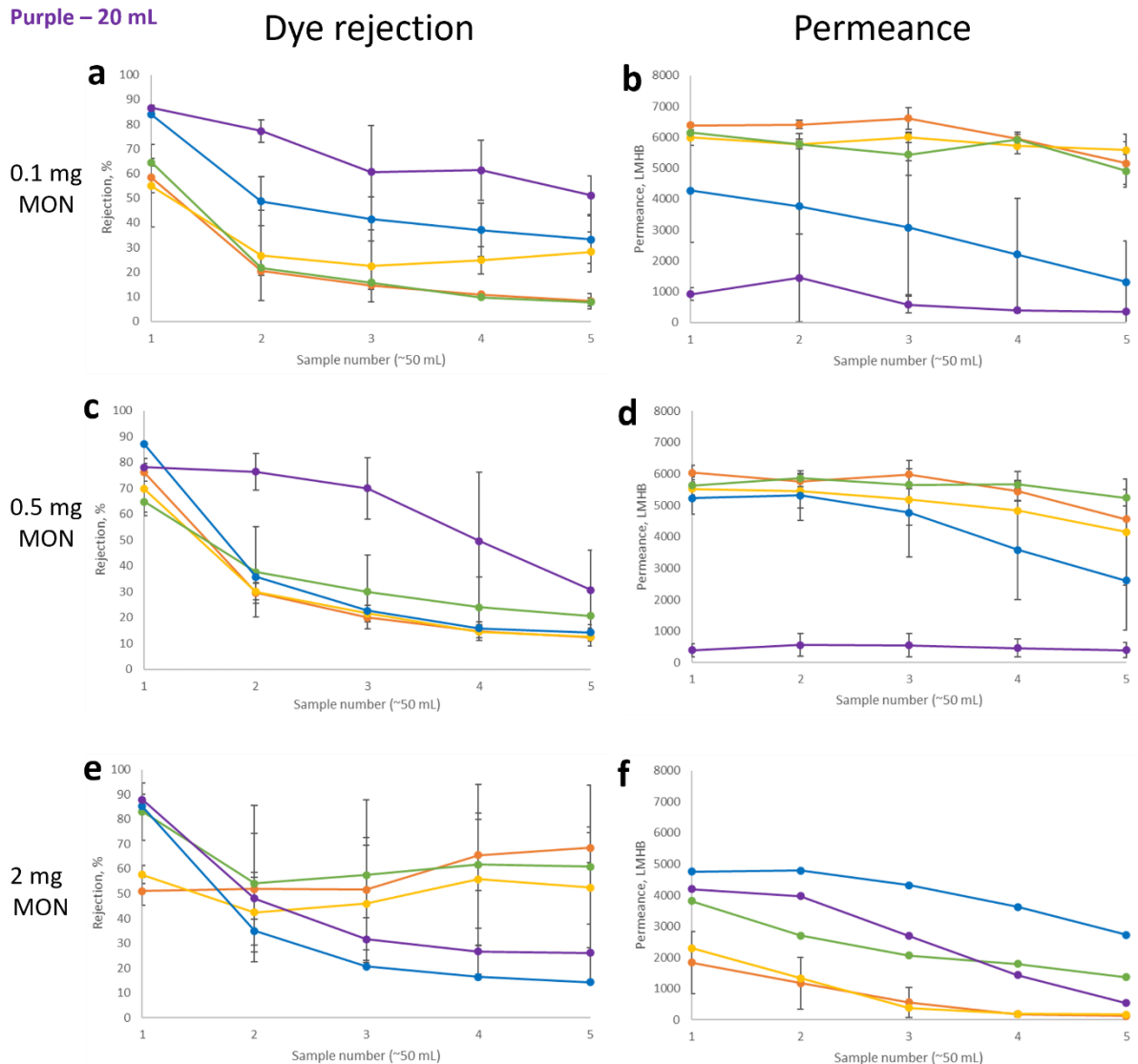


Figure 3.5. Average (a, c, e) percentage rejection and (b, d, f) permeance data, with associated errors, for membranes prepared with $Zr_6(F_4BDC)$ (amounts stated on the left) and PDDA (see legend in top right), tested with brilliant blue G dye. Volumes of PDDA in the legend refer to volumes of the 0.1 wt% solution of PDDA added to the MON suspension during membrane preparation.

For the membranes formed with 0.1 mg mL^{-1} loading of MONs shown in Figure 3.5a, increasing amounts of PDDA resulted in improved dye rejection compared to those prepared with lower amounts of PDDA. However, as shown in Figure 3.5b, membranes prepared with higher amounts of PDDA have lower permeance, and vice versa for lower amounts of PDDA. The percentage rejection for all

membranes decreased over the duration of the experiment. however, the permeance remained relatively constant.

For membranes prepared with 0.5 mg of $Zr_6(F_4BDC)$, the effect of PDDA loading appears to be negligible below 20 mL, with 0.3 – 10 mL membranes following the same downward trend. Figure 3.5c shows improved rejection for membranes prepared with 0.5 mg MON and 20 mL PDDA, this still follows a downward trend, with the rejection dropping off at the end of the experiment. There is also a difference in permeance between the 0.3 – 10 mL PDDA membranes and the 20 mL PDDA membrane (Figure 3.5d), with the 20 mL PDDA membrane giving a much lower permeance.

Finally, membranes prepared with 2 mg of $Zr_6(F_4BDC)$ show a different trend in PDDA loading affect. In Figure 3.5e, membranes prepared with 10 and 20 mL PDDA show lower rejection than membranes prepared with 0.3, 0.6 and 1.5 mL PDDA. The membranes prepared with 2 mg MON and 1.5 mL PDDA shows the most stable rejection over the course of the experiment, ending on an average rejection of 60.9 %. When looking at the permeance (Figure 3.5f), again these membranes show different trends to those seen in Figure 3.5b and Figure 3.5d, with membranes prepared with 10 and 20 mL of PDDA having higher permeance than those prepared with lower PDDA loadings. These membranes have a very small error in the measurements, hence the majority of error bars not being visible. The membrane prepared with 2 mg $Zr_6(F_4BDC)$ and 1.5 mL PDDA shows the most stable permeance over the duration of the test, ending on an average of 1360 LMHB, a comparable figure to literature examples.²⁴

In membranes prepared with 0.1 and 0.5 mg $Zr_6(F_4BDC)$, 20 mL PDDA yielded the highest rejection of brilliant blue G, giving average rejections of 67.3 and 64.5 % respectively. It is likely this is because the active rejecting layer of the membrane becomes thicker with increasing amounts of PDDA. However, the same trend is not seen when 2 mg $Zr_6(F_4BDC)$ is added to the PES support, when 20 mL PDDA is added, the rejection is lower for smaller PDDA loadings (averaging at 44.1 %). This could be due to increased mass loadings of the MON interrupting the film formation of the membrane active layer and

the MONs playing a larger role in the rejection of the dye. In the majority of the membranes, the rejection decreases with time, indicating an adsorptive mechanism is in play.

The permeance has an inverse relationship to the rejection, whereby the more PDDA present, the lower the permeance. For 0.1 and 0.5 mg $Zr_6(F_4BDC)$, the permeance decreases steadily with time, it is likely this is due to the membrane pores getting blocked by adsorbed dye molecules. When 2 mg of $Zr_6(F_4BDC)$ is used, the permeance does not decrease with increasing PDDA loading. As hypothesised with the rejection results above, the increased mass loadings at 2 mg MON and 20 mL PDDA could be disrupting the film formation on top of the PES support, allowing the feed solution to pass through the membrane more quickly.

Membranes prepared with 2 mg $Zr_6(F_4BDC)$ and 0.3, 0.6 and 1.5 mL PDDA have a more stable rejection, indicating the rejection is due to size exclusion rather than absorption.²⁵ This is a positive result as the longer a membrane can maintain rejection the better. As the membrane prepared with 2 mg $Zr_6(F_4BDC)$ and 1.5 mL PDDA showed the most consistent rejection (average 63.5 %) and permeance (average 2000 LMHB) results during the course of the experiment, this membrane was chosen for further dye testing.

Overall, a five times increase of MON loading has no significant effect on the membrane performance. There are still significant drops in rejection when going from 0.1 to 0.5 mg of MON. The permeance exhibits less significant drops, however it is still not stable over the course of the test. A twenty time increase of MON loading exhibits more significant effects. At 20 mg of MON permeance and rejection decrease, however rejection is more consistent over the experiment duration. The higher PDDA loadings have improved permeance, showing that, at high loadings, MONs can improve the permeance of membranes with high PDDA loadings. An additional factor that may influence the variability of the membranes is the amount of MON and PDDA that passes through the membrane during the deposition process. The expected mass loadings and actual mass loadings could be very

different, however for these experiments the difference between these amounts was not investigated.

A range of dyes with different charges and sizes were chosen, to further understand the mechanism of the rejection of these membranes. Brilliant blue G is a very large negatively charged dye, to understand if the negative charge was playing a part in the rejection mechanism, a smaller negative dye was chosen for testing (methyl orange). Methylene blue, a smaller positively charged dye was used as the opposite of brilliant blue G. Lastly, rhodamine B, a neutral dye, larger than methyl orange and methylene blue, was used to evaluate if the size of brilliant blue G was causing the rejection. Unfortunately, we were unable to source an organic dye as large as brilliant blue G to fully assess if size exclusion was causing the rejection. All dyes were prepared at 10 mg L⁻¹ and were prepared at least one day in advance of testing to ensure complete dissolution. Table 3.1 shows the structures, molecular weights and formal charges associated with these dyes.

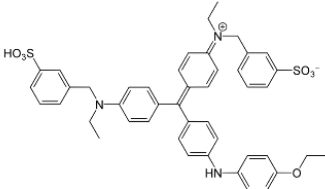
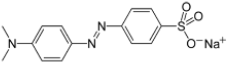
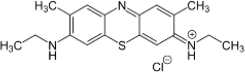
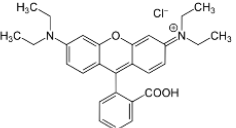
Name	Structure	Molecular Weight /g mol ⁻¹	Formal Charge
Brilliant Blue G		831.03	-1
Methyl Orange		304.31	-1
Methylene Blue		284.40	+1
Rhodamine B		479.02	0

Table 3.1. Structure, molecular weight, and formal charges associated with brilliant blue G, methyl orange, methylene blue and rhodamine B dyes used for water purification testing.

Figure 3.6 shows the percentage rejection (left) and permeance (right) results for optimised $Zr_6(F_4BDC)/PDDA$ membranes.

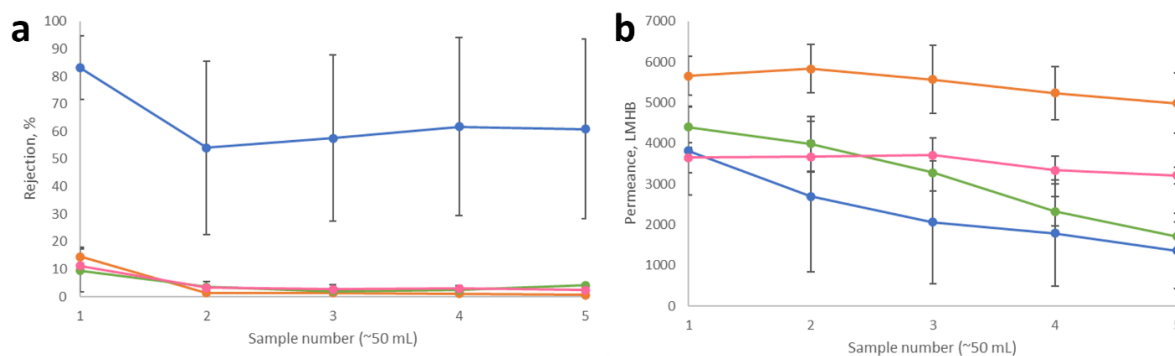


Figure 3.6. Average (a) percentage rejection and (b) permeance data, and associated errors, for membranes prepared with 2 mg $Zr_6(F_4BDC)$ and 1.5 mL PDDA (0.1 wt%), tested with brilliant blue G (blue), methyl orange (orange), methylene blue (green) and rhodamine B (pink) dyes.

Other than brilliant blue G, the rejection for all the dyes was poor to start with ($\leq 26\%$) and decreased over the duration of the test to near zero. This indicates that there is a size exclusion effect taking place as smaller dye molecules of the same charge (methyl orange and rhodamine B) do not show the same rejection performance as the larger brilliant blue G dye. Again, the inverse is seen in the permeance, whereby smaller dye molecules (brilliant blue G is the largest of this dye selection) pass through the membrane much faster.

3.2.4. PDDA effect on absorbance measurements

Colleagues at Evove suggested that PDDA was highly water soluble, which could affect the absorbance spectra of the permeate solution. In order to understand if the PDDA was affecting the permeance results UV-vis studies were undertaken looking at the effect PDDA has on the absorption spectra of brilliant blue G. Figure 3.7 shows the UV-Vis spectra of brilliant blue G dye when increasing amounts of PDDA.

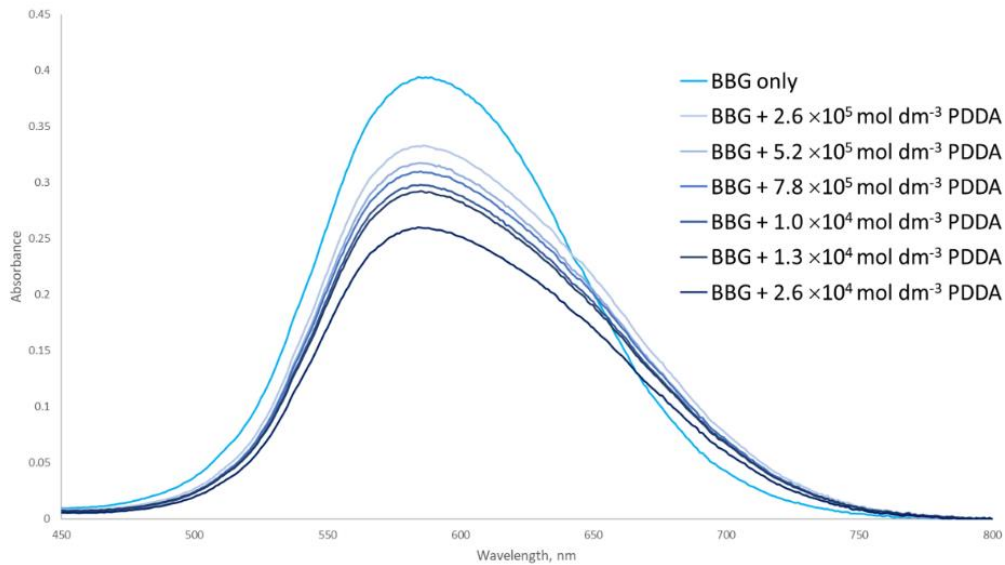


Figure 3.7. UV-Vis spectra of brilliant blue G (BBG) dye when combined with PDDA (0.1 wt%).

When PDDA is added to a brilliant blue G solution, the absorbance curve clearly does not have a Gaussian shape, a broad shoulder is appearing with a red shifted maximum. When the data from the brilliant blue G solution with $2.6 \times 10^4 \text{ mol dm}^{-3}$ PDDA is deconvoluted, the two peaks can be seen clearly (Figure 3.8).

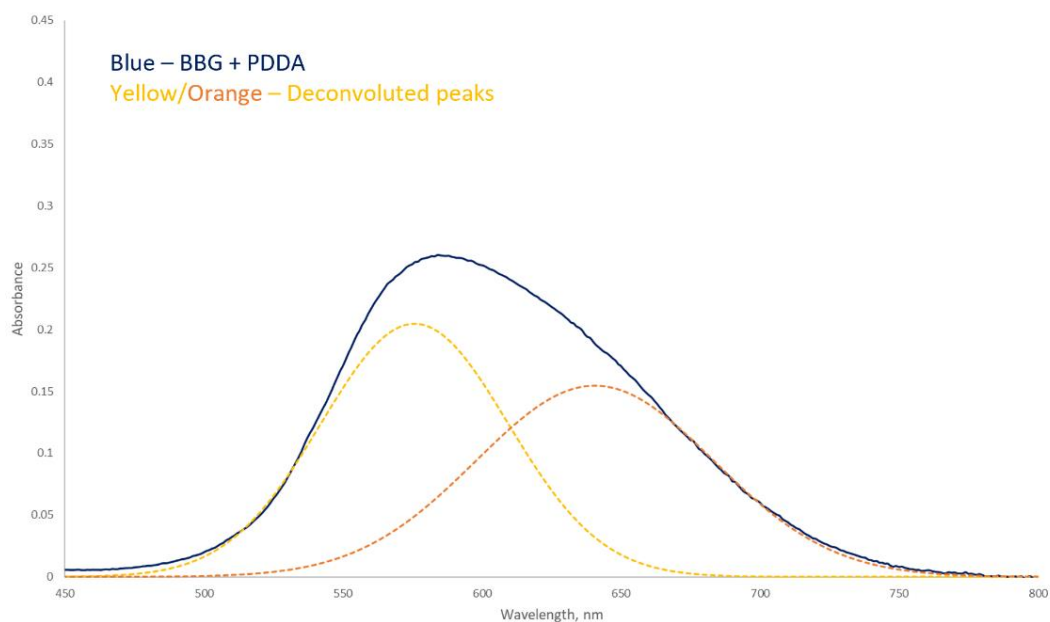


Figure 3.8. UV-Vis spectra of brilliant blue G dye combined with $2.6 \times 10^4 \text{ mol dm}^{-3}$ PDDA (blue) and the calculated deconvolution peaks (yellow and orange).

The UV-Vis spectra of all organic dyes used to test $Zr_6(F_4BDC)/PDDA$ membranes, with and without $2.6 \times 10^4 \text{ mol dm}^{-3}$ PDDA, were recorded (Figure 3.9). Methylene blue and rhodamine B (Figure 3.9a and b) display no changes in absorbance with the addition of PDDA. However, in Figure 3.9c, methyl orange exhibits a different UV-Vis curve upon the addition of PDDA.

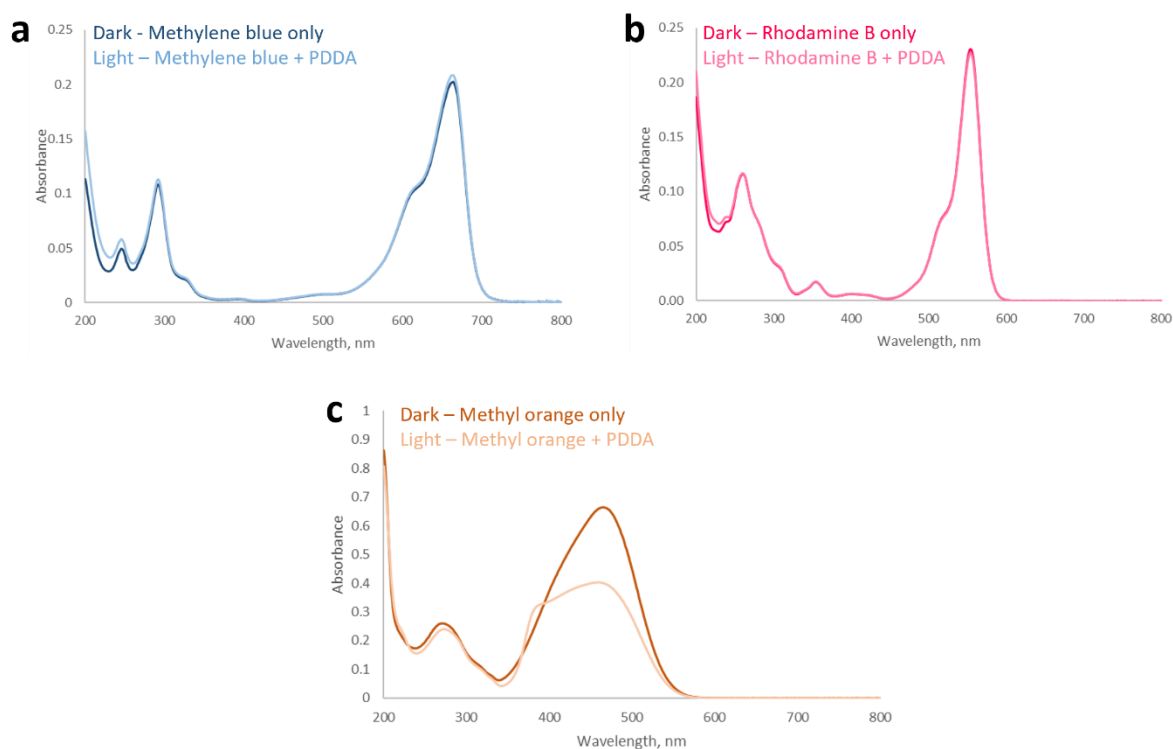


Figure 3.9. UV-vis spectra of (a) methylene blue, (b) rhodamine B and (c) methyl orange with and without the addition of PDDA (0.1 wt%). In each graph, the darker colour represents the dye alone and the lighter colour represents the dye with PDDA.

If the PDDA on the $Zr_6(F_4BDC)/PDDA$ membrane surface is redissolving into solution in the dead-end cell, and then passing through the membrane, this would affect the absorbance of the collected samples, in turn affecting the calculated rejection for the membranes. Additionally, with PDDA coming off the membrane surface, the $Zr_6(F_4BDC)/PDDA$ mixed matrix membrane is degrading, which will have a negative impact on the membrane performance.

Ang and Hong report excellent stability of their MON/PDDA membranes, with no mention of the PDDA solubility or effect of PDDA on the UV-Vis spectra of brilliant blue G and methyl orange dyes.²³ While it is not reported in the paper, Ang and Hong may have used additional steps in their membrane

preparation or the nanosheets they use (Zn (Fe(III)) meso-tetra(4-carboxyphenyl)porphine chloride (Zn-TCP(Fe))) may interact and cross-link with the PDDA in different ways to $Zr_6(F_4BDC)$.

3.2.5. $Zr_6(F_4BDC)$ /PDDA membranes on different pore size PES supports

AFM analysis undertaken in **Chapter 2 Section 2.2.1** showed an average nanosheet lateral size and thickness of 593 nm and 2.4 nm. The optimised system investigated so far (2 mg $Zr_6(F_4BDC)$, 1.5 mL PDDA (0.1 wt%)) was deposited onto a PES membrane with a 0.2 μm average pore size. Whilst the average lateral size is greater than that of the pores, it is possible that many of the $Zr_6(F_4BDC)$ MONs are falling through the larger pores in the PES support and not forming a good active layer on the surface.

A PES support with an average pore size of 0.03 μm was therefore investigated as a support with smaller pores could alleviate the problem of the nanosheets falling through the membrane and form a better active layer. Dye rejection and permeance performance of $Zr_6(F_4BDC)$ /PDDA membranes prepared with the 0.03 μm pore size PES were tested using brilliant blue G and compared with the optimised system made with 0.2 μm pore size PES supports (Figure 3.10).

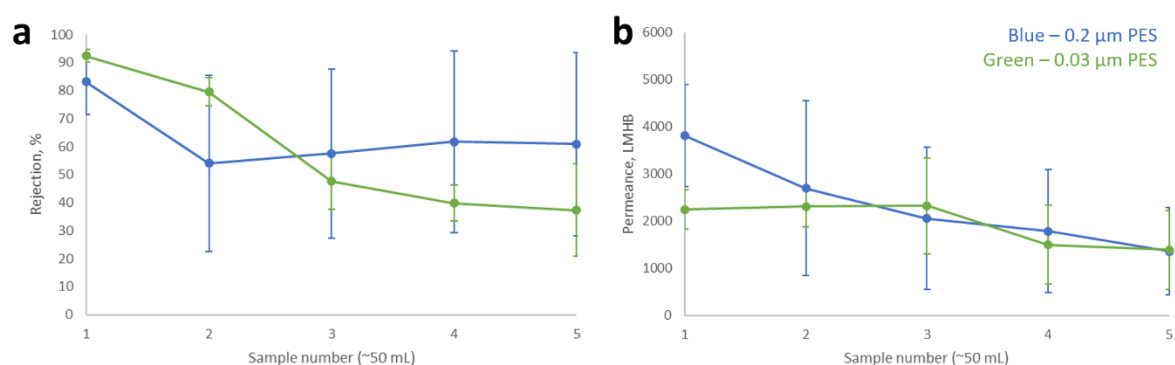


Figure 3.10. Brilliant blue G rejections from $Zr_6(F_4BDC)$ -PDDA membranes prepared using PES with 0.2 μm (dark blue) and 0.03 μm (light blue) pore sizes.

The membranes prepared using 0.03 μm pore size PES initially have a marginally improved rejection compared to the 0.2 μm pore size PES membranes (92.4 % vs 83.2 %). The initial permeance in the 0.03 μm system is lower, as expected from a membrane with smaller pores, this also decreases over

time. For both the rejection and the permeance results, the membranes prepared with 0.2 μm PES have a much larger variation than the membranes with 0.03 μm PES.

The rejection and permeance decreases in the 0.03 μm PES membranes indicate an adsorptive effect, whereby once all the adsorption sites are occupied, more dye molecules are being let through and the blocked sites slow down the flow of the feed solution.

To understand the surface topology of the $\text{Zr}_6(\text{F}_4\text{BDC})/\text{PDDA}$ membranes SEM analysis was carried out. Figure 3.11 shows SEM images $\text{Zr}_6(\text{F}_4\text{BDC})$ and all vacuum deposited onto PES supports).²³ The SEM images of the $\text{Zr}_6(\text{F}_4\text{BDC})/\text{PDDA}$ membranes do not show a continuous thin film over the top of the PES support. The $\text{Zr}_6(\text{F}_4\text{BDC})$ particles have an interpenetrated ball-like structure seen in the bulk MOF SEM images in **Chapter 2 Section 2.2.1**. The poor rejection of the $\text{Zr}_6(\text{F}_4\text{BDC})/\text{PDDA}$ membranes can be attributed to the lack of a continuous thin film active layer on top of the PES support.

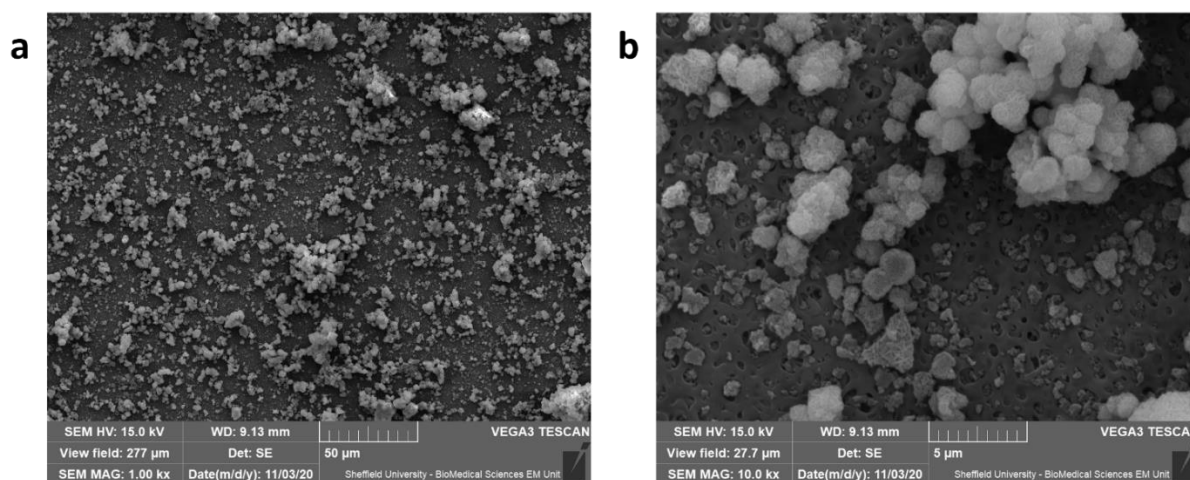


Figure 3.11. SEM images of optimised $\text{Zr}_6(\text{F}_4\text{BDC})/\text{PDDA}$ membranes on 0.3 μm pore size PES.

Looking at AFM images previously analysed in detail in **Chapter 2 Section 2.2.1**, there are large, monolayer nanosheets present when $\text{Zr}_6(\text{F}_4\text{BDC})$ is suspended in water (Figure 3.12a). Due to the nature of AFM and SEM imaging techniques, there is a discrepancy between the particles seen. AFM focusses on smaller particles, so larger particles are often missed. While the opposite is seen in SEM,

the limitations of the technique make thinner, smaller nanosheets difficult to image using SEM machines.

Additionally, as is fully characterised in **Chapter 2 Section 2.2.1**, the powder x-ray diffraction (PXRD) pattern for nanosheet (**hns**) phase $Zr_6(F_4BDC)$ is phase pure, and fully undergoes the transition from the hexagonal close packed (**hcp**) phase to the nanosheet phase. This PXRD analysis is in line with the literature reported PXRD analysis by F. C. N. Firth *et al.*²⁷ These SEM images (Figure 3.11), combined with the AFM and PXRD data (Figure 3.12) show that not all of the material in the hns phase auto-exfoliates, leaving a mixture of interpenetrated ball-like structures as well as monolayer nanosheets.

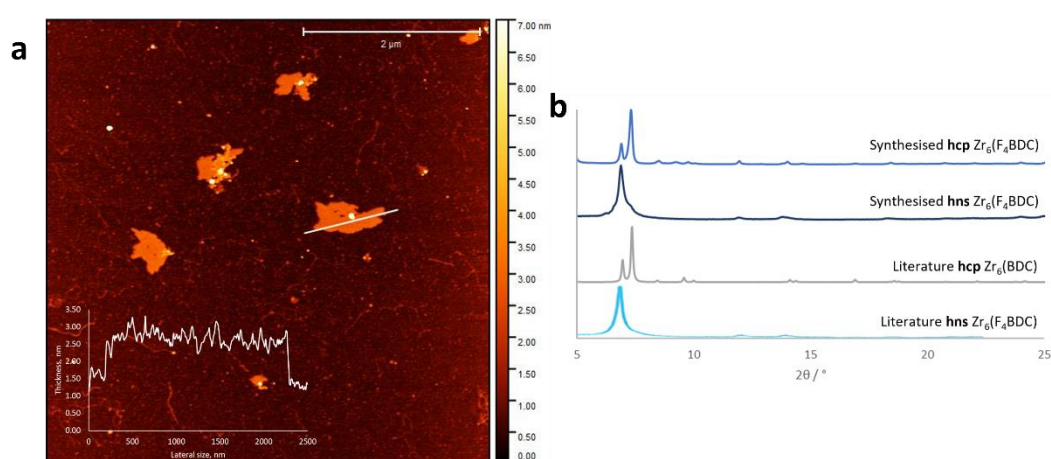


Figure 3.12. (a) AFM topological profile with height profile inset of $Zr_6(F_4BDC)$ and (b) stacked plot of PXRD patterns for $Zr_6(F_4BDC)$ in the nanosheet (hns) phase, the bulk (hcp) phase and a literature reported bulk (hcp) phase.²⁷

Any of the larger MOF material present in the suspension when preparing the MON-membranes can skew the membrane loading calculation, leading to calculated membrane loadings for the nanosheets being inaccurate and under representative. Using centrifugation techniques, larger MOF particles can be removed from suspensions to give MON only suspensions, which may allow for membranes with a thin continuous film of MONs on the surface to be prepared.

3.2.6. $Zr_6(F_4BDC)$ “MON-only” membranes

To attempt the preparation of membranes with only $Zr_6(F_4BDC)$ MONs present, the $Zr_6(F_4BDC)$ suspension (1 mg mL^{-1}) was subjected to centrifugation at 1500 rpm for 20 minutes and the top 90% of the supernatant was removed. The nanosheet yield after centrifugation was 47 %, therefore the

membrane mass loadings were calculated using a 0.467 mg mL^{-1} concentration. Membranes were then prepared to have the same mass loading as the optimum $\text{Zr}_6(\text{F}_4\text{BDC})/\text{PDDA}$ membrane loading, 2 mg. Figure 3.13 shows the percentage rejection and permeance results for these membranes prepared with centrifugation when tested with brilliant blue G dye solution (10 mg L^{-1}).

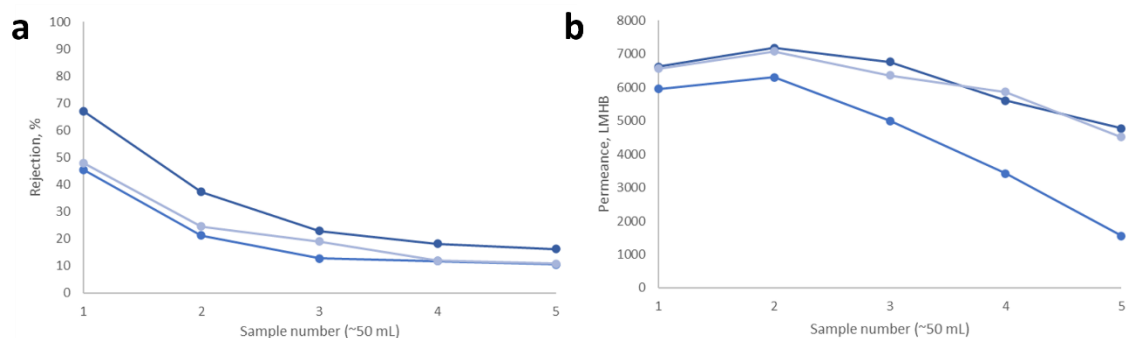


Figure 3.13. (a) Percentage rejection and (b) permeance data for membranes prepared with $\text{Zr}_6(\text{F}_4\text{BDC})$ after centrifugation, tested with brilliant blue G dye. Each data series represents a repeat experiment.

The rejection seen in Figure 3.13a starts at an average of 54 % and drops down to an average of 13 %. The permeance also has a downward trend, going from 6376 to 3613 LMHB. Figure 3.14 shows SEM images of this membrane with additional centrifugation in the preparation (a), compared to $\text{Zr}_6(\text{F}_4\text{BDC})/\text{PDDA}$ membranes prepared without any additional centrifugation. In the membrane prepared with centrifugation, there are more small thin particles, as well as the large, interpenetrated ball-like structures. There is still no continuous active layer on the PES surface which accounts for the poor rejection performance. The decline in both rejection and permeance is likely due to adsorption sites being filled, preventing more dye from being removed from the feed and blocking the membrane pores, slowing the permeance of the membrane.

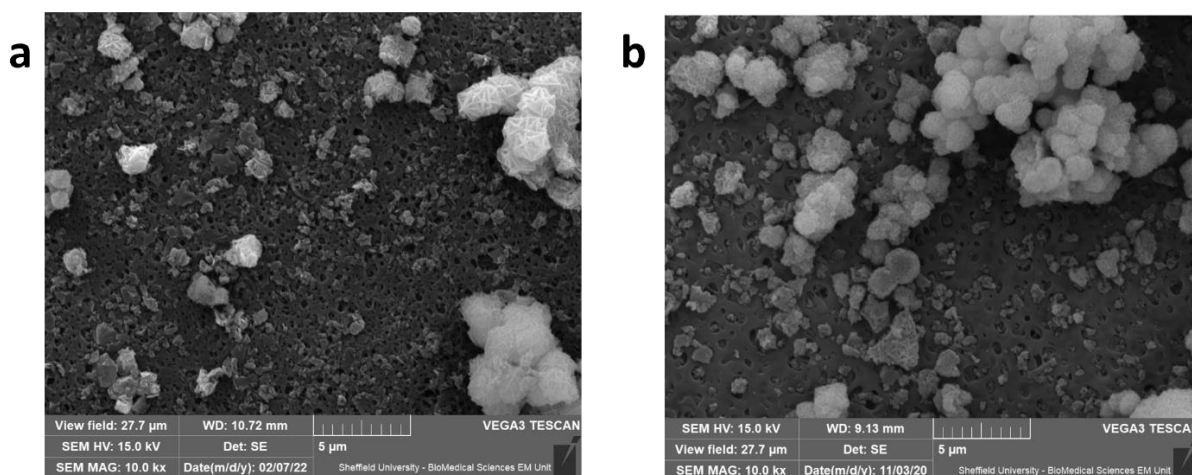


Figure 3.14. SEM images of (a) $Zr_4(F_4BDC)$ membrane prepared with centrifugation and (b) $Zr_6(F_4BDC)/PDDA$ membrane.

3.3. Conclusions

From the SEM images of the $Zr_6(F_4BDC)$ membranes, it is clear that a continuous thin-film is not being formed by the MONs on the surface of the PES support. PDDA polymer was used as an additive to help the formation of this continuous thin-film, however SEM images show the presence of $Zr_6(F_4BDC)$ interpenetrated ball-like structures. While the previous AFM images collected show the presence of monolayer nanosheets (Figure 3.12), it is clear that $Zr_6(F_4BDC)$ does not undergo complete self-exfoliation upon suspension in water and there is a mixture of nanosheet and bulk interpenetrated structures. While centrifugation appears to lead to an increase in nanosheet material in the SEM images (Figure 3.14), bulk material is still present, and a continuous thin film is not formed. This disparity in material seen in AFM and SEM is due to the type of technique used. In AFM, there is an inherent bias for small, thin material so bulk particles are often missed. SEM mainly images the bulk particles, with the thin nanosheets often being on the edges of the instrument resolution.

PDDA is a water-soluble polymer, and thus, during the water purification experiments with the dead-end cell, the PDDA is most likely coming off the membrane and solubilising into the feed solution. It has been shown that this affects the absorption of the dye when UV-Vis spectra are observed (Figure 3.7), leading to false retentate results and potentially false rejection results. Additionally, the PDDA

coming off the membrane is a form of membrane degradation which will negatively impact the membrane performance.

The $Zr_6(F_4BDC)$ particles do not form a good active layer on top of the membrane, especially with the polymer additive (PDDA) intended to help form a continuous thin film and secure the MONs to the support being so soluble in water. If large, thin nanosheets cannot be obtained, having the particles better incorporated within the mixed matrix membrane would allow the MOF/MONs to have a more direct impact on the performance of the membrane.

Despite the limited water purification performance success of the $Zr_6(F_4BDC)$ membranes, this work was still valuable as a means of developing a method previously unknown to the Foster group. Learning the processes of membrane preparation, optimisation and water purification testing was useful and lay the groundwork for future MON-membrane chapters.

3.4. References

- 1 T. Devic and C. Serre, *Chem. Soc. Rev.*, 2014, **43**, 6097–6115.
- 2 J. H. Cavka, S. Jakobsen, U. Olsbye, N. Guillou, C. Lamberti, S. Bordiga and K. P. Lillerud, *J. Am. Chem. Soc.*, 2008, **130**, 13850–13851.
- 3 J. Winarta, B. Shan, S. M. McIntyre, L. Ye, C. Wang, J. Liu and B. Mu, *Cryst. Growth Des.*, 2020, **20**, 1347–1362.
- 4 T. Mu, Y. Zhang, W. Shi, G. Chen, Y. Liu and M. Huang, *Chemosphere*, 2021, **269**, 128686.
- 5 D. Ma, G. Han, S. B. Peh and S. B. Chen, *Ind. Eng. Chem. Res.*, 2017, **56**, 12773–12782.
- 6 F. Xiao, M. Cao, R. Chu, X. Hu, W. Shi and Y. Chen, *J. Colloid Interface Sci.*, 2022, **610**, 671–686.
- 7 P. Wan, M. Yuan, X. Yu, Z. Zhang and B. Deng, *Chem. Eng. J.*, 2020, **382**, 122921.
- 8 Q. Li, Z. Liao, J. Xie, L. Ni, C. Wang, J. Qi, X. Sun, L. Wang and J. Li, *Environ. Res.*, 2020, **191**, 110215.
- 9 D. L. Zhao, W. S. Yeung, Q. Zhao and T. S. Chung, *J. Memb. Sci.*, 2020, **604**, 118039.
- 10 Y. Zhao, Y. Liu, X. Wang, X. Huang and Y. F. Xie, , DOI:10.1021/acsami.9b01923.
- 11 Y. Liu, D. Gan, M. Chen, L. Ma, B. Yang, L. Li, M. Zhu and W. Tu, *Sep. Purif. Technol.*, 2020, **253**, 117552.
- 12 Z. Huang, H. M. Guan, W. L. Tan, X. Y. Qiao and S. Kulprathipanja, *J. Memb. Sci.*, 2006, **276**, 260–271.
- 13 Z. Gu, S. Yu, J. Zhu, P. Li, X. Gao and R. Zhang, *Desalination*, 2020, **493**, 114661.
- 14 S. Y. Fang, P. Zhang, J. L. Gong, L. Tang, G. M. Zeng, B. Song, W. C. Cao, J. Li and J. Ye, *Chem. Eng. J.*, 2020, **385**, 123400.
- 15 L. E. Peng, Z. Yang, L. Long, S. Zhou, H. Guo and C. Y. Tang, *J. Memb. Sci.*, 2022, **641**, 119871.
- 16 H. Li, Y. Yin, L. Zhu, Y. Xiong, X. Li, T. Guo, W. Xing and Q. Xue, *J. Hazard. Mater.*, 2019, **373**, 725–732.
- 17 X. Zhu, Z. Yu, H. Zen, X. Feng, Y. Liu, K. Cao, X. Li and R. Long, *J. Appl. Polym. Sci.*, 2021, **138**, 50765.
- 18 X. Liu, N. K. Demir, Z. Wu and K. Li, *J. Am. Chem. Soc.*, 2015, **137**, 6999–7002.
- 19 X. Wang, L. Zhai, Y. Wang, R. Li, X. Gu, Y. Di Yuan, Y. Qian, Z. Hu and D. Zhao, *ACS Appl. Mater. Interfaces*, 2017, **9**, 37848–37855.
- 20 L. Wan, C. Zhou, K. Xu, B. Feng and A. Huang, *Microporous Mesoporous Mater.*, 2017, **242**, 207–213.
- 21 Y. Yang, K. Goh, R. Wang and T. H. Bae, *Chem. Commun.*, 2017, **53**, 4254–4257.
- 22 E. M. Dias and C. Petit, *J. Mater. Chem. A*, 2015, **3**, 22484–22506.
- 23 H. Ang and L. Hong, *ACS Appl. Mater. Interfaces*, 2017, **9**, 28079–28088.
- 24 W. Jia, B. Wu, S. Sun and P. Wu, *Nano Res.*, 2020, **13**, 2973–2978.

- 25 D. M. Warsinger, S. Chakraborty, E. W. Tow, M. H. Plumlee, C. Bellona, S. Loutatidou, L. Karimi, A. M. Mikelonis, A. Achilli, A. Ghassemi, L. P. Padhye, S. A. Snyder, S. Curcio, C. D. Vecitis, H. A. Arafat, J. H. L. V and J. H. Lienhard, *Prog. Polym. Sci.*, 2018, **81**, 209–237.
- 26 H. Ang and L. Hong, *ACS Appl. Mater. Interfaces*, 2017, **9**, 28079–28088.
- 27 F. C. N. Firth, M. J. Cliffe, D. Vulpe, M. Aragonés-Anglada, P. Z. Moghadam, D. Fairen-Jimenez, B. Slater and C. P. Grey, *J. Mater. Chem. A*, 2019, **7**, 7459–7469.

Chapter 4

Preliminary testing of metal-organic nanosheets for the use in water purification membranes

4.1. Introduction

In the previous chapter, the 2D analogue of UiO-66(F₄BDC) was used as a model system in order to develop a method of both membrane preparation and water purification testing. MONs have key advantages that make them suitable for water purification membranes, including ultrathin thickness, diverse chemistry and a tunable nature.¹ In this chapter a range of MON systems are screened to evaluate their suitability for use in water purification membranes. The range of MONs used were chosen based on prior synthesis experience and availability within the Foster group. Additionally, the chosen systems demonstrate how tunable the MON systems are and how changing the combination of metal centre and linker affects water purification ability.

Five different MONs were used in this work; CuBDC (copper 1,4-benzenedicarboxylate), NH₂-MIL-53(Al) (aluminium 2-amino-1,4-benzenedicarboxylate, MIL= Matériaux de l'Institut Lavoisier), ZIF-7 (zinc benzimidazolate, ZIF = zeolitic imidazolate framework), Zr-BTB (zirconium 1,3,5-Tris(4-carboxyphenyl)benzoate) and Zr-PTB (zirconium 2,4,6-pyridinetriyltris(4-benzoate)). This chapter systematically examines each system, individually introducing the structure and background of the MONs before discussing the MON synthesis, membrane preparation and water purification results. The MON synthesis and exfoliation routes are mainly discussed for context and the MON-membrane testing is the main focus of this chapter. The overall aim of this chapter was to identify a candidate MON-membrane system for optimisation experiments in **Chapter 5**.

4.2. Results and discussion

4.2.1. Pristine PES membrane

Polyether sulfone (PES) membranes (47 mm, 30 nm pore size) purchased from Sterlitech were used as a support for the vacuum deposition of MONs in the preparation of MON-membranes. As a reference for the performance of MON-membranes, pristine PES was tested with a solution of brilliant blue G dye (10 mg L⁻¹). PES reference membranes were tested in a stirred dead-end cell. And three repeats were carried out. The concentration of the dye solutions, before and after filtration tests, were

measured using ultraviolet-visible (UV-Vis) spectroscopy. Figure 4.1 shows the average percentage rejection and permeance data (and associated standard deviation error) for the pristine PES membranes. The PES membranes show an average rejection of 16 % and permeance of 6446 L m⁻² h⁻¹ bar⁻¹ (LMHB) over the duration of the test.

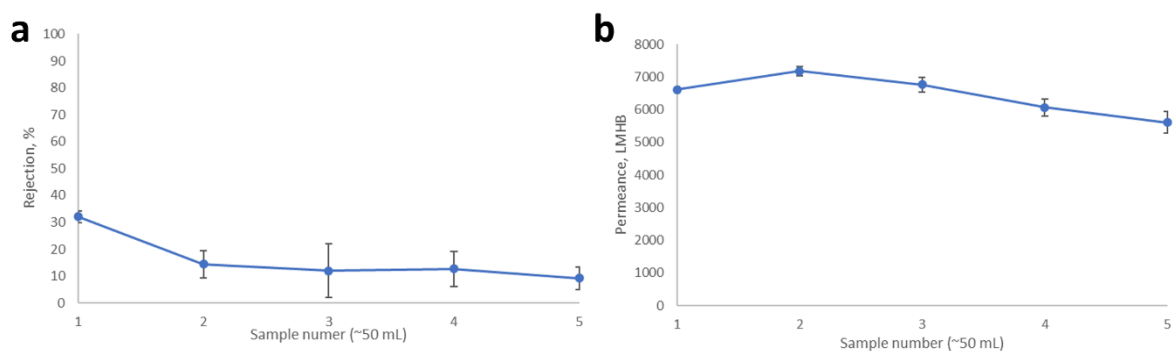


Figure 4.1. (a) Percentage rejection and (b) permeance data for pristine PES membranes tested with brilliant blue G dye.

4.2.2. CuBDC

CuBDC is a layered MOF with a paddlewheel structure, synthesised using 1,4-benzenedicarboxylic acid and a copper centre.² The layered structure of this MOF (Figure 4.2) allows for exfoliation of the layers into two-dimensional (2D) nanosheets.

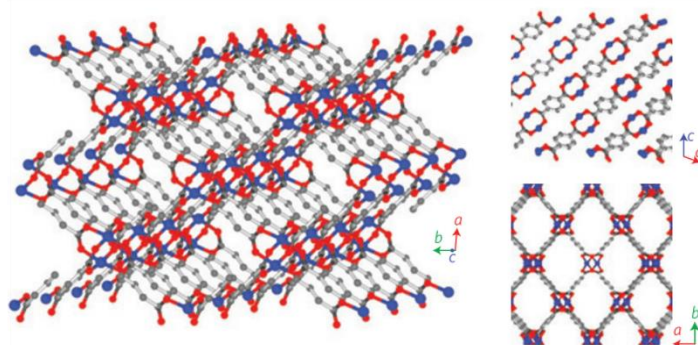


Figure 4.2. Crystal structure of CuBDC. Figure adapted from reference 2.

CuBDC nanosheets have already been utilised in MON-membranes for water purification by R. Dai *et al.*³ CuBDC MONs were incorporated into polyamide membranes for forward osmosis applications whereby they improved water permeability and membrane antifouling. The inclusion of CuBDC nanosheet improved the water flux and reverse solute flux in the forward osmosis process by 50%.³

Additionally, there is prior expertise within the Foster group of the synthesis and exfoliation of copper-paddlewheel MONs.^{4,5}

CuBDC was synthesised by a solvothermal method first outlined by C. G. Carson *et al.* in 2009.⁶ Equimolar quantities of copper nitrate trihydrate ($\text{Cu}(\text{NO}_3)_2 \cdot 3\text{H}_2\text{O}$) and terephthalic acid (BDC) were dissolved in dimethyl formamide (DMF) and heated to 110 °C for 36 h. The product was washed with both DMF and diethyl ether before drying in air. Samples were analysed by powder x-ray diffraction (PXRD) and compared to a simulated PXRD pattern from reported single-crystal x-ray diffraction data (Figure 4.3).^{6,7} CuBDC yielded a blue powder product.

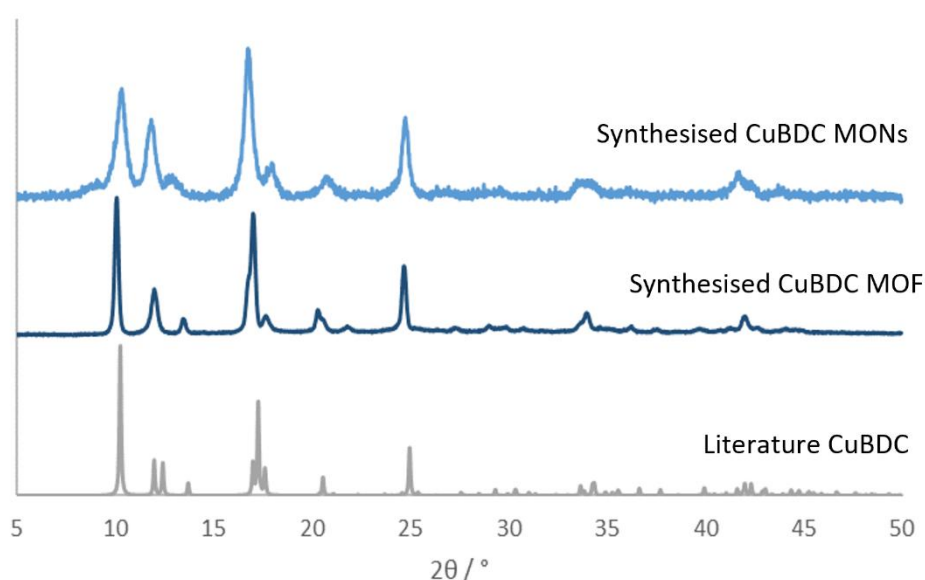


Figure 4.3. PXRD patterns comparing literature reported CuBDC (grey), synthesised CuBDC bulk MOF (dark blue) and CuBDC MONs (pale blue).

The PXRD pattern for CuBDC MOF shown in Figure 4.3 matches the literature reported pattern. Samples were then exfoliated via sonication at 80 kHz for 12 h in acetonitrile. These conditions are based on previous studies within the Foster group investigating exfoliation of Cu-paddlewheel based MONs.^{4,5} The PXRD pattern (Figure 4.3) for the exfoliated material shows it retained the same crystal structure as the bulk material. Some peak broadening was observed which is expected as the material transitions from three dimensional (3D) to two dimensional (2D) (Figure 4.3). AFM analysis was carried out on the suspensions after hot-drop coating onto freshly cleaved mica. Figure 4.4 shows the AFM

images and associated height profiles of CuBDC nanosheets. CuBDC nanosheets have an average lateral size and height of 236 and 63 nm respectively.

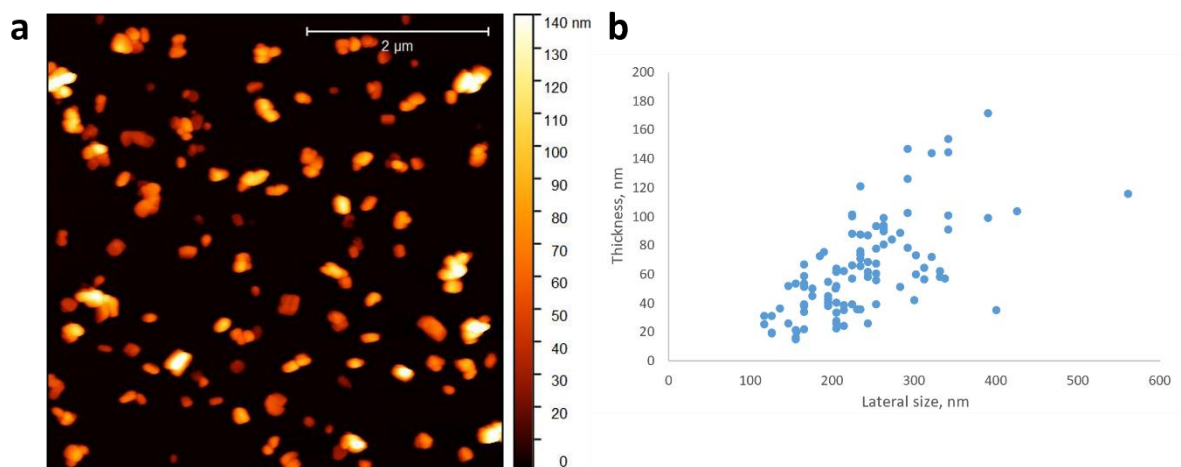


Figure 4.4. AFM topological profiles of (a) CuBDC nanosheets and (b) a scatter plot of associated height profiles.

CuBDC membranes were prepared and tested using the following method which was developed in **Chapter 3**. Suspensions of exfoliated nanosheets in acetonitrile were diluted with water before they were deposited onto a PES support membrane via vacuum filtration to give a nanosheet mass loading of 400 mg m⁻². PES supports (47 mm diameter) with pores sizes of 30 nm were used. All membranes were tested using a Sterlitech HP4750 stirred dead-end cell. Each membrane was prepared three times to carry out three repeat water purification tests.

Figure 4.5 shows the percentage rejection and permeance data for CuBDC membranes when tested with a 10 mg L⁻¹ solution of brilliant blue G dye in water. As the test progresses, the percentage rejection of dye and the permeance of the membrane both decreases.

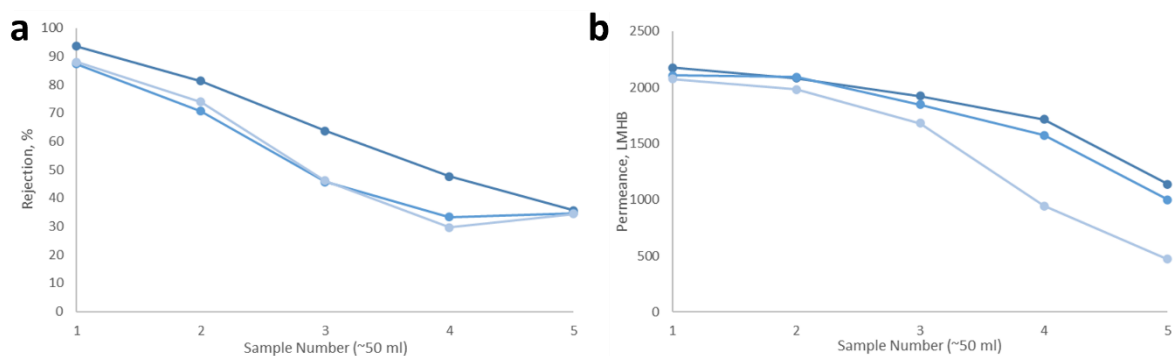


Figure 4.5. (a) Dye rejection and (b) permeance data for CuBDC membranes tested with brilliant blue G dye. Each line of data points represents a repeat experiment.

The initial high rejection of 90 % (average) is likely due to adsorption of dye molecules to CuBDC nanosheets and to the PES membrane itself. Once all of the adsorption sites have been filled, more dye molecules are able to pass through the membrane, accounting for the reduced percentage rejection. The adsorption blocks some of the membrane pores with dye molecules which in turn slows the permeance of the membrane. This decrease in rejection and permeance means that these CuBDC membranes were not subject to further optimisation experiments.

4.2.3. NH₂-MIL-53(Al)

MIL-53 is a well-known MOF composed of metal-centres (V, Cr, Al, Fe, In, Co, Ga, Mn, Sc, Ni) and 1,4-benzenedicarboxylate linkers (Figure 4.6). MIL-53 is known for its stability in water and has been used in a number of membranes for water purification.⁸⁻¹⁰ Additionally, NH₂-MIL-53 (Al 2-amino-1,4-benzenedicarboxylate) has examples of use in water purification membranes, where it is incorporated into polyamides, polyethersulfone and polyvinylidene fluoride based membranes and used for desalination and removal of heavy metals and dyes.¹¹⁻¹⁴ While the MIL-53 systems reported in the described water purification membranes are not layered, synthesis of 2D NH₂-MIL-53 has been reported using urea as a modulating agent, it is these NH₂-MIL-53 MONs that are used in this chapter for screening.¹⁵

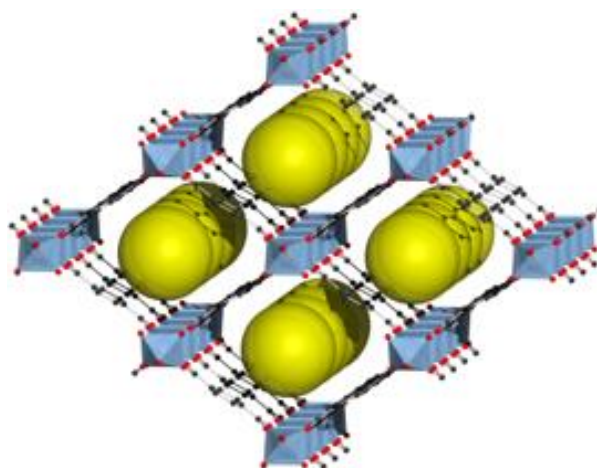


Figure 4.6. Crystal structure of MIL-53. Figure reproduced from reference 16.

Due to their stability in water, MOFs from the MIL- family have been widely used in water purification membranes¹⁷. NH₂-MIL-53 MOFs were incorporated into polyvinylidene fluoride (PVDF) membranes using a solvothermal method, this lead to a > 92 % rejection of various organic dyes and a permeances of more than 500 L⁻¹m⁻²h⁻¹MPa⁻¹. This was a 478 % permeance increase compared to traditional membranes whilst maintaining rejection performance.¹³

2D NH₂-MIL-53(Al) (Al(OH)[H₂N-BDC], where BDC = 1,4-benzenedicarboxylate) was synthesised solvothermally using a method outlined by Z. Li *et al.*¹⁵ 2-Amino-1,4-benzenedicarboxylic acid, aluminium chloride (AlCl₃·6H₂O) and urea (modulating agent) were dissolved in distilled water before heating at 150 °C for 5 hours. After removal from the oven, the product was washed with distilled water, removed via centrifugation, and dried to a powder.

Samples were analysed by powder x-ray diffraction (PXRD) and compared to a simulated PXRD pattern from reported single-crystal x-ray diffraction data to determine if the synthesis was successful (Figure 4.7).

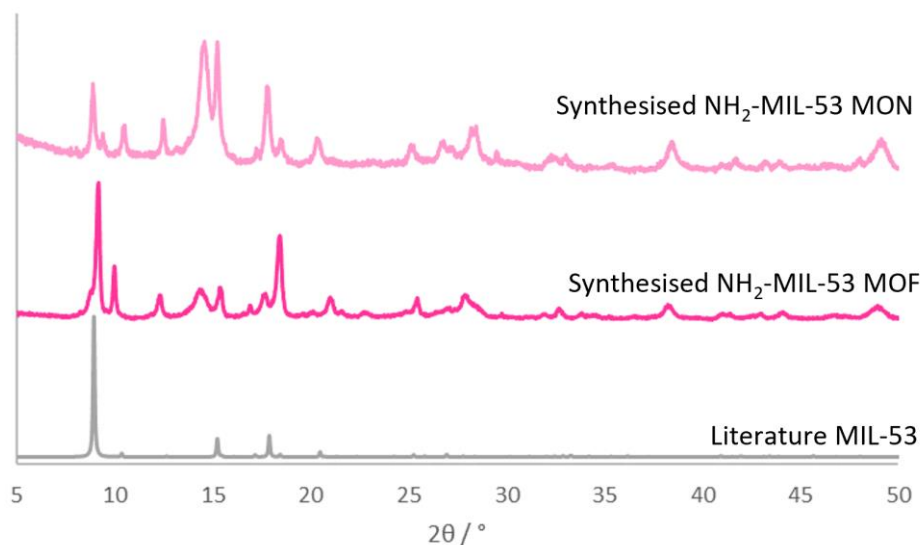


Figure 4.7. PXRD patterns comparing literature reported $\text{NH}_2\text{-MIL-53}$ (grey), synthesised $\text{NH}_2\text{-MIL-53}$ bulk MOF (dark pink) and $\text{NH}_2\text{-MIL-53}$ MONs (pale pink).¹⁵

While there are some additional peaks in the synthesised $\text{NH}_2\text{-MIL-53}$ MOF, the pattern mostly matches the literature reported pattern well. The additional peaks are likely due to a mixed phase. MIL-53 can undergo structural changes, exhibiting pore opening and closing in a “wine rack” behaviour.¹⁸ Partial opening or closing of the pores can cause a mixed phase to be present, which would account for additional peaks in the PXRD. This mixed phase is unimportant for this water purification screening experiment as it is a preliminary test to gain insight into whether the $\text{NH}_2\text{-MIL-53(Al)}$ system is worth pursuing for further optimisation.

$\text{NH}_2\text{-MIL-53}$ MOFs were then exfoliated into nanosheets via sonication at 37 kHz for 12 h in acetonitrile before centrifugation at 1500 rpm for 1 h to remove any remaining bulk material. PXRD analysis was carried out on dried MONs to determine if the same phase as the bulk MOF was maintained. Figure 4.7 shows the PXRD of the $\text{NH}_2\text{-MIL-53}$ MONs compared to the bulk MOF. The peaks in both patterns match, however there is disparity in peak intensities. It is likely that the peaks at 14.5, 15.4, 26.8, 28.4, 38.5 and 49.1 ° are due to the presence of a mixed phase discussed above.

MONs were analysed via AFM after hot-drop coating onto freshly cleaved mica. Figure 4.8 shows an example AFM topological profile and the associated height profiles in a scatter plot. The majority of $\text{NH}_2\text{-MIL-53}$ nanosheets are under 35 nm in height and typically between 50 – 100 nm in lateral size.

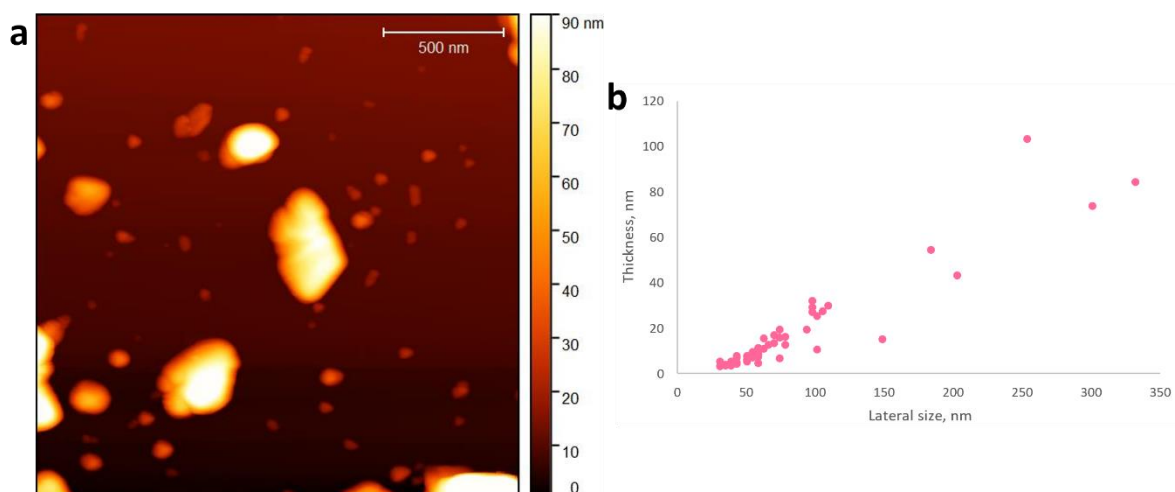


Figure 4.8. (a) AFM topological profile of $\text{NH}_2\text{-MIL-53}$ and (b) a scatter plot of the associated height profiles.

400 mg m^{-2} of $\text{NH}_2\text{-MIL-53}$ was deposited onto a PES membrane via a vacuum deposition technique. Three repeat membranes were prepared and tested using an aqueous brilliant blue G dye solution (10 mg L^{-1}) in a dead-end cell.

Figure 4.9 shows the percentage rejection and permeance data for $\text{NH}_2\text{-MIL-53}$ membranes tested with a 10 mg L^{-1} solution of brilliant blue G dye in water. As the experiment progresses, the rejection halves (from an average of 81 to 39 %). This is likely due to an adsorptive effect at the beginning of the test, dye molecules adsorb to the MONs and the PES membrane. As with the CuBDC example, once these adsorption sites are filled the rejection and permeance decrease.

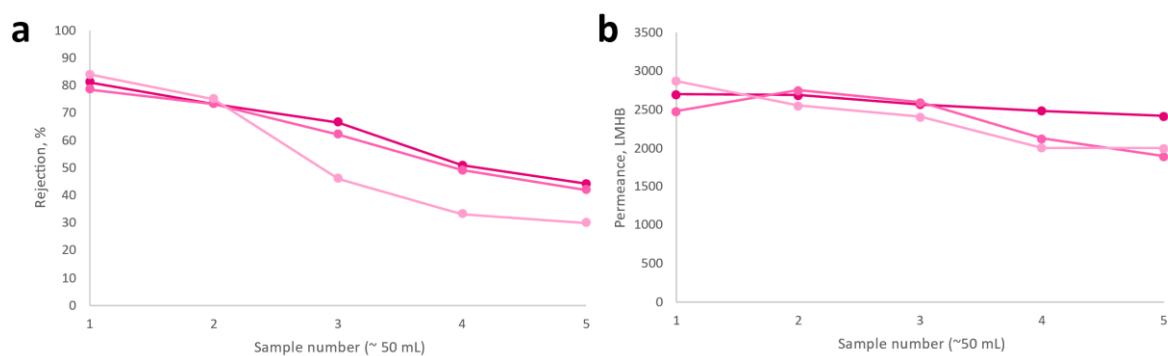


Figure 4.9. (a) Dye rejection and (b) permeance data for NH₂-MIL-53 membranes tested with brilliant blue G dye. Each line of data points represents a repeat experiment.

The decline in the percentage rejection meant that these NH₂-MIL-53 membranes were not taken forward for further optimisation at this stage. However, the stability of the permeance over the course of the experiment is a promising result, and these MON-membranes could be investigated in future research.

4.2.4. ZIF-7

ZIF-7 was also chosen for screening due to its water stability, ability to synthesise a 2D analogue and the benzimidazole linker provides a very different pore structure to the 1,4-benzenedicarboxylic acid-based MONs mentioned above. ZIF-7 is synthesised from benzimidazole ligands and zinc ions. There are three different forms of ZIF-7, each of which can be accessed through structural transitions caused by desolvation and dehydration.¹⁹ Figure 4.10 shows the phase transitions of ZIF-7. There are a number of examples of ZIFs being used in water purification membranes for separation of oil/water²⁰⁻²², organic dyes²³⁻²⁵ and desalination.²⁶

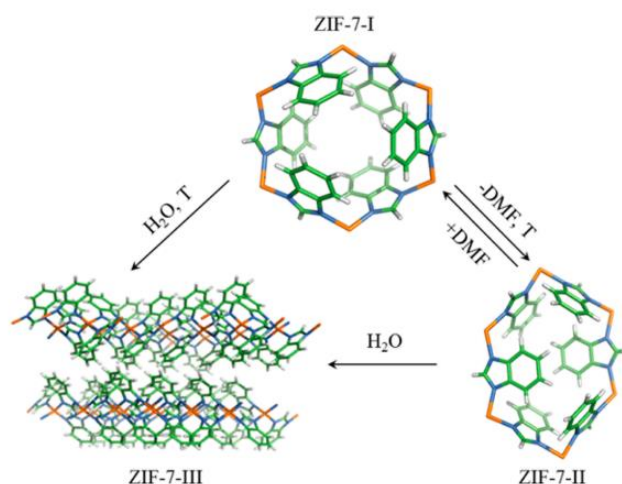


Figure 4.10. Schematic illustrating the phase transitions of ZIF-7. Reproduced from reference 19.

ZIF-7 was first synthesised in nanosheet form by Y. Peng *et al.* in a paper where the ZIF-7 nanosheets were deposited into an α -Al₂O₃ disk to form molecular sieving membranes for gas separation.²⁷ Building on that paper, H. Lui *et al.* reported an adapted synthesis for ZIF-7 nanosheets.²⁸ There is also an example of a ZIF MON-membrane being used for the filtration of an organic dye, with improved rejection and good water flux.²⁹

Zinc nitrate (Zn(NO₃)-6H₂O) and an excess of benzimidazole (bim) were dissolved in DMF and kept room temperature for a minimum of 72 h. The purple powder product was removed from the suspension by centrifugation and washed with methanol before drying at 80 °C in a vacuum oven. After synthesis, the ZIF-7-I powder was refluxed in water for 24 h to initiate a phase change from ZIF-7-I to ZIF-7-III, the layered phase of ZIF-7 (see Figure 4.10).

Both the refluxed ZIF-7-III bulk and sonicated ZIF-7-III nanosheets were analysed by PXRD to ensure the phase change was successful and was maintained after sonication. Figure 4.11 shows the stacked PXRD patterns of ZIF-7-I and ZIF-7-III compared to a patterns calculated from CSD single crystal data.^{19,30} It is clear that the refluxed ZIF-7-I sample transitions to the ZIF-7-III phase and that this phase is retained after sonication.

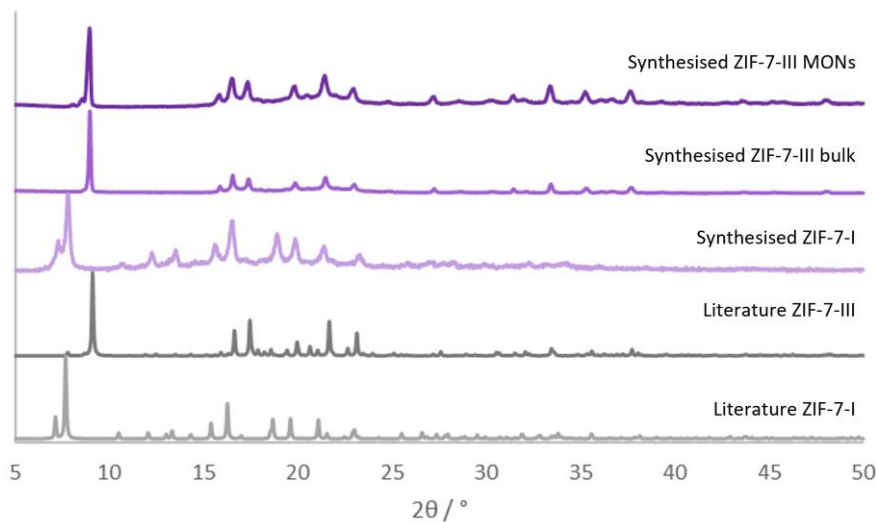


Figure 4.11. Stacked PXRD patterns comparing literature reported ZIF-7-I and ZIF-7-III (grey) and synthesised ZIF-7-I, bulk ZIF-7-III and ZIF-7-III after exfoliation into MONs (purple).^{19,30}

Samples were then exfoliated via sonication for 2 h at 80 kHz in a 50:50 mixture of methanol and n-propanol. AFM analysis was carried out on the suspensions after hot-drop coating onto freshly cleaved mica. Figure 4.12 shows an AFM topological profile of ZIF-7-III and the associated height profiles in a scatter plot. ZIF-7-III MONs were all 100 – 250 nm in lateral size and an average of 0.89 nm in thickness. This ultrathin thickness is in agreement with the layer thickness calculated from single crystal structure, indicating these are monolayer nanosheets.²⁸

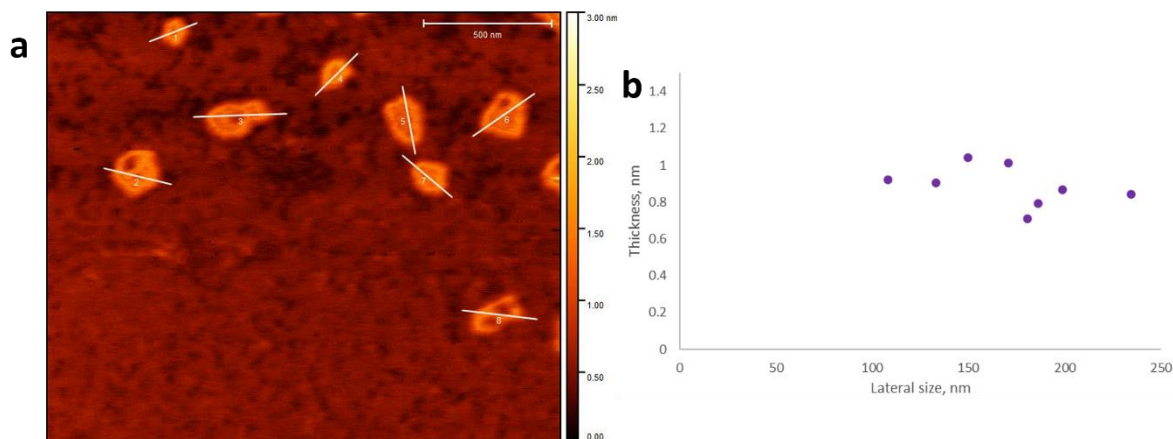


Figure 4.12. (a) AFM topological profile of exfoliated ZIF-7-III and (b) a scatter plot of the associated height profiles.

Membranes were prepared by depositing 400 mg m^{-2} of ZIF-7-III onto a PES membrane via a vacuum deposition technique. Three repeat membranes were prepared and tested using an aqueous brilliant blue G dye solution (10 mg L^{-1}) in a dead-end cell.

Figure 4.13 shows the percentage rejection and permeance results for ZIF-7-III membranes tested with brilliant blue G.

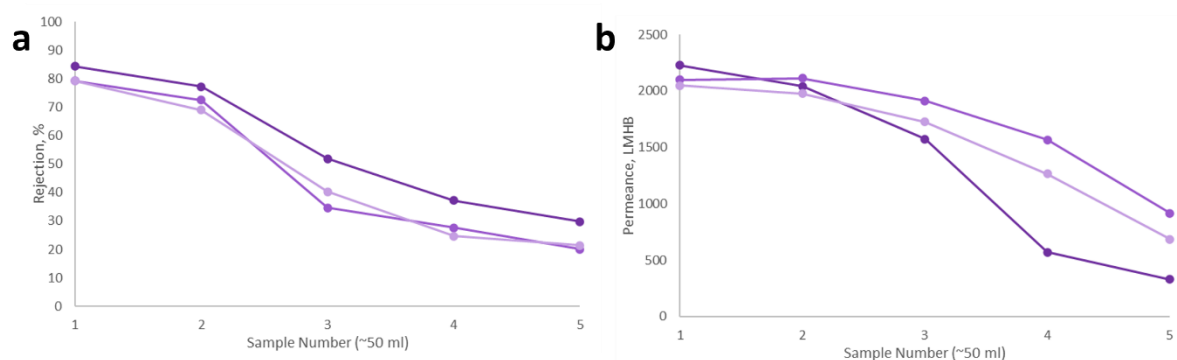


Figure 4.13. (a) Percentage rejection and (b) permeance data for ZIF-7-III membranes tested with brilliant blue G dye. Each line of data points represents a repeat experiment.

Similarly, to results seen with CuBDC membranes (Figure 4.5), with ZIF-7-III membranes there is initially high percentage rejection of the dye (80 %), however this decreases with time due to adsorption sites filling up. The same trend is seen in the permeance data, whereby the filling of adsorption sites slows the water permeance during the course of the experiment. Due to this performance decline, these ZIF-7-III membranes were not taken forward for optimisation.

4.2.5. Zr-tricarboxylates

Finally, a MON system with tricarboxylate ligands was chosen for screening in water purification membranes. Zr-BTB and isorecticular Zr-PTB were chosen due to their similarities to the previously used UiO-66 MOFs (**Chapter 2**) and the availability of the ligands. Figure 4.14 shows the crystal structure of both Zr-BTB and Zr-PTB. While, to our knowledge, there has never been a report of Zr-BTB or Zr-PTB being used for water purification, Zr-BTB has been reported in several publications from the W. Lin research group for catalysis and energy transfer applications,^{31–34} and Zr-PTB has recently been reported by Y. Xu *et al.* for the use as an ultrasensitive pH probe.³⁵ The use of Zr-BTB in mixed

matrix membranes has been reported, enhancing the CO₂ gas separation performance of the membranes.³⁶

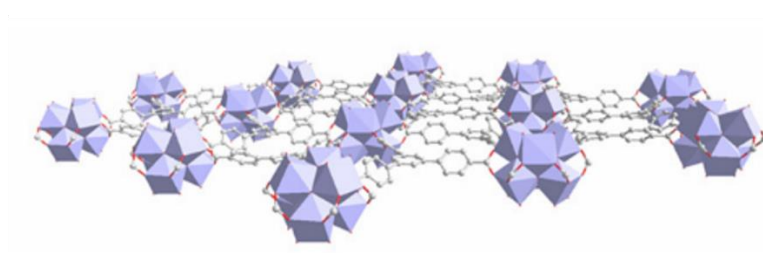


Figure 4.14. Crystal structure of Zr-BTB and Zr-PTB. Figure reproduced from reference 33.

Synthesis of zirconium tricarboxylate based nanosheets was based on reported syntheses of the Hf-BTB MOF commonly known as NUS-8.^{36,37} Both 1,3,5-benzenetricarboxylic acid (H₃BTB) and 4''-(pyridine-2,4,6-triyl)tricarboxylic acid (H₃PTB) were used with zirconium chloride to prepare Zr-tricarboxylate MONs. Zirconium chloride (ZrCl₄) and either H₃BTB or H₃PTB were dissolved in a mixture of DMF, water and formic acid before heating to 120 °C for 48 h. The resultant white powder was washed firstly with DMF to remove unreacted ligand then with ethanol to remove residual DMF. Samples were analysed by PXRD to ensure synthesis was successful (Figure 4.15). The Zr-BTB and Zr-PTB PXRD patterns have a good match with the reference pattern produced within the Foster group, so the synthesis was successful. The PXRD patterns are also in line with literature analysis (Figure 4.15b).

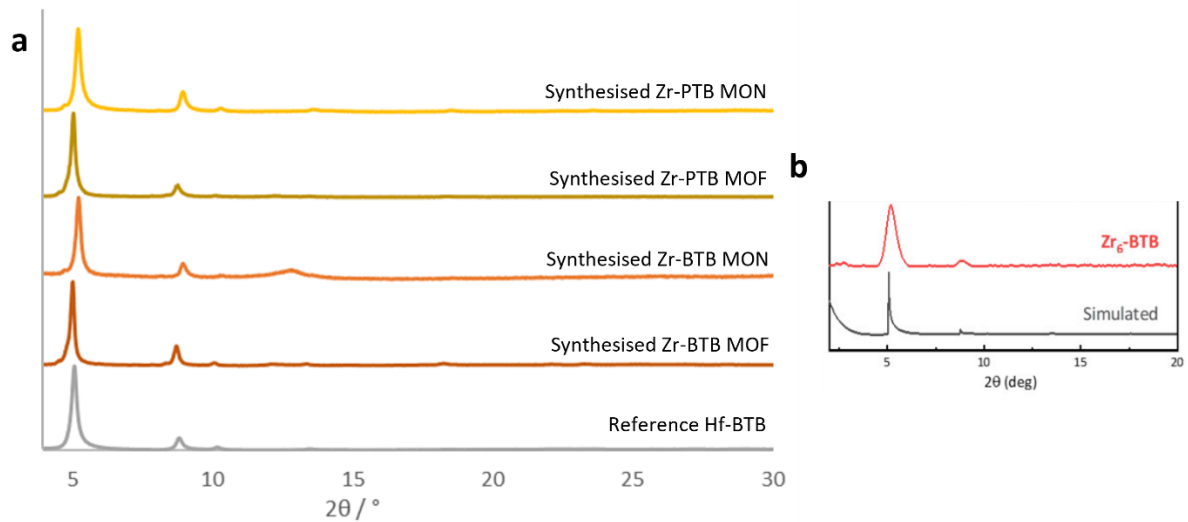


Figure 4.15. Stacked PXRD patterns comparing (a) reference Hf-BTB (grey), synthesised Zr-BTB MOF and MON (orange) and synthesised Zr-PTB MOF and MON (yellow) (b) and literature reported data. Figure adapted from reference 33.

Samples were then exfoliated via sonication in acetonitrile at 37 kHz for 12 h. After sonication samples were analysed by AFM. Figure 4.16 shows the AFM profiles (a, c), and scatter plots of the associated height profiles (c, d).

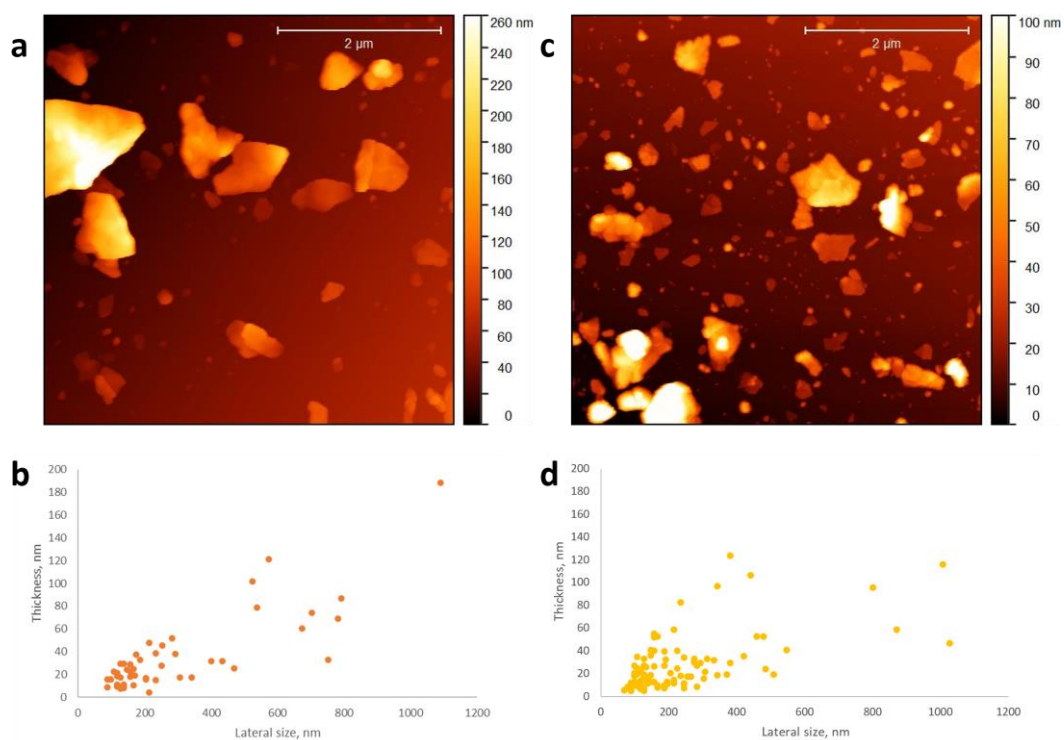


Figure 4.16. AFM topological profiles and scatter plots of associated height profiles of (a, b) Zr-BTB and (c, d) Zr-PTB.

Both Zr-BTB and Zr-PTB have a high density of nanosheets between 100 – 300 nm in lateral size, however, Zr-PTB (yellow) has more nanosheets under 20 nm in thickness compared to Zr-BTB (orange).

Membranes were prepared by depositing 400 mg m^{-2} of Zr-BTB or Zr-PTB onto a PES membrane via a vacuum deposition technique. Three repeat membranes were prepared and tested using an aqueous brilliant blue G dye solution (10 mg L^{-1}) in a dead-end cell.

Figure 4.17 shows the percentage rejection and permeance results of Zr-BTB membranes tested with brilliant blue G dye.

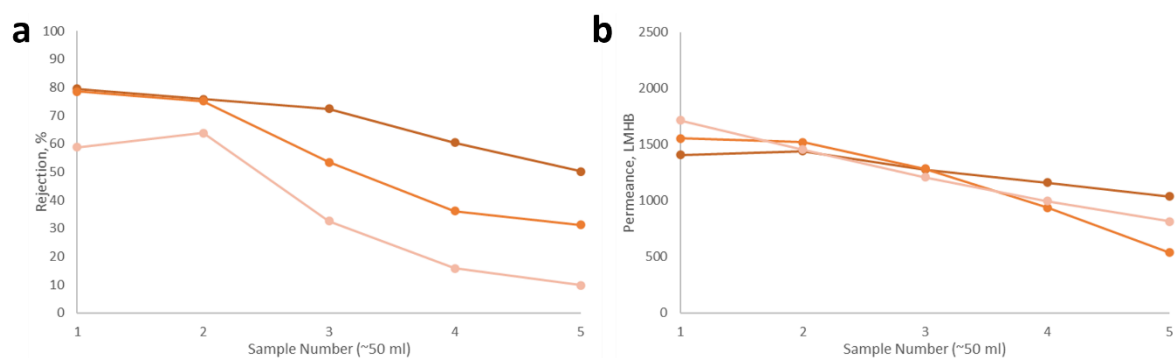


Figure 4.17. (a) Percentage rejection and (b) permeance data for Zr-BTB membranes tested with brilliant blue G dye. Each line of data points represents a repeat experiment.

There is a high degree of variability in the rejection data for this membrane system, this could be due to an inhomogeneous MOF-MON mixture present in the suspension of Zr-BTB after exfoliation. When an aliquot is removed from the exfoliation suspension and added to the volume of water for membrane preparation, the proportion of MOF and MON in this mixture is unknown. Despite the variability, the general trend of decreasing rejection and permeance is seen once again, leading to these Zr-BTB membranes not being selected for further optimisation studies.

Figure 4.18 shows the percentage rejection and permeance data for Zr-PTB dye rejection experiments using brilliant blue G. The rejection results for Zr-PTB membranes has a different profile compared to previous experiments with other MONs.

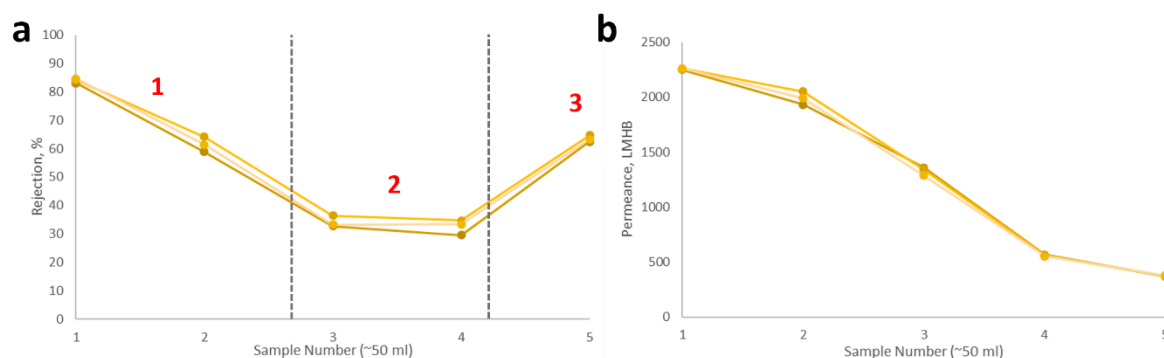


Figure 4.18. (a) Percentage rejection and (b) permeance data for Zr-PTB membranes tested with brilliant blue G dye. Each line of data points represents a repeat experiment. Points 1, 2 and 3, on (a) refer to adsorption, compression, and size exclusion respectively.

The data can be split into three rough sections, marked on Figure 4.18a as 1, 2 and 3. At section 1, the initial average rejection was 84 %, this drops to an average low of 33 % in section 2 and then increases again in section 3 to an average of 63 %. We hypothesise that the initial high rejection in section 1 is due to the adsorptive effect of the MONs and the membrane. The rejection decreases and the dye molecules and water flow between the layers of MONs on the membrane surface. The pressure from the feed flowing through the membrane compressed the Zr-PTB MONs on the surface during section 2. Finally, after the MONs have been compressed onto the surface, section 3 shows the size exclusion mechanism where the compressed layer of Zr-PTB are rejecting the brilliant blue G dye molecules based on size. While the detailed percentage rejection and permeance data was not published, Y. Peng *et al.* reported the use of compression in their membrane preparation.²⁹ The report concluded that before the compression, the large interlayer spacing between nanosheets enables large amounts of water molecules to transport through the membrane while having poor impurity rejection. The compaction step was introduced to their $Zn_2(bim)_3$ based nanosheets to facilitate more constrictive interlayer channels.²⁹

Due to this increase at the end of the ~250 mL experiment, the Zr-PTB system was explored further as a MON-membrane candidate. **Chapter 5** explores the use of an additional compression step in the membrane preparation to skip straight to section 3 for size exclusion-based rejection. Prolonged testing, MON loading optimisation and the use of additives are also explored in **Chapter 5**.

4.3. Conclusions

This chapter looks at the synthesis of six different MON systems; NH₂-MIL-53, CuBDC, ZIF-7, Zr-BTB and Zr-PTB. The synthesis and subsequent exfoliation into nanosheets of each of these systems was successful and all yielded MONs of differing quality, from monolayer ZIF-7 to wider ranging CuBDC.

Each MON system was deposited onto membranes and tested for water purification using brilliant blue G dye. With the exception of Zr-PTB, all systems displayed a decrease in both percentage rejection and permeance over time, we hypothesise that this is due to an initial adsorptive affect giving rise to perceived high rejection, this drops away as the adsorption sites fill and the dye molecules pass through unhindered. The permeance also decreases over time, likely due to blocking of the pores as adsorption sites.

Zr-PTB showed a different rejection profile, whereby there was an initial adsorptive affect, followed by a nanosheet compression stage and finally size exclusion takes over, an effect as reported previously by Y. Peng *et al.*²⁹ Due to this increase in rejection at the end of the Zr-PTB water purification experiment, this system was taken forward for prolonged testing and membrane water purification in **Chapter 5**.

While all of the different systems performed in slightly different ways, there is currently no suggestions as to the cause of these differences. With this small sample size, no trends can be drawn based on for example pore size, linker usage or MON size. A larger study is needed to unpick the affects different MON qualities have on membrane performance. Overall, this chapter demonstrates the variety of MON properties that can affect membrane performance, and highlights Zr-PTB MONs as a promising MON-membrane candidate.

4.4. References

- 1 J. Nicks, K. Sasitharan, R. R. R. Prasad, D. J. Ashworth and J. A. Foster, *Adv. Funct. Mater.*, 2021, **31**, 2103723.
- 2 T. Rodenas, I. Luz, G. Prieto, B. Seoane, H. Miro, A. Corma, F. Kapteijn, F. X. Llabrés I Xamena, J. Gascon, F. X. Llabrés and J. Gascon, *Nat. Mater.*, 2015, **14**, 48–55.
- 3 R. Dai, X. Zhang, M. Liu, Z. Wu and Z. Wang, *J. Memb. Sci.*, 2019, **573**, 46–54.
- 4 D. J. Ashworth, T. M. Roseveare, A. Schneemann, M. Flint, I. D. Bernáldes, P. Vervoorts, R. A. Fischer, L. Brammer and J. A. Foster, *Inorg. Chem.*, 2019, **58**, 10837–10845.
- 5 J. Nicks, J. Zhang and J. A. Foster, *Chem. Commun.*, 2019, **55**, 8788–8791.
- 6 C. G. Carson, K. Hardcastle, J. Schwartz, X. Liu, C. Hoffmann, R. A. Gerhardt and R. Tannenbaum, *Eur. J. Inorg. Chem.*, 2009, **2009**, 2338–2343.
- 7 M. E. Braun, C. D. Steffek, J. Kim, P. G. Rasmussen and O. M. Yaghi, *Chem. Commun.*, 2001, **1**, 2532–2533.
- 8 X. Wang, X. Ba, N. Cui, Z. Ma, L. Wang and Z. Wang, *J. Memb. Sci.*, 2019, **590**, 117057.
- 9 H. Mahdavi, M. Karami, A. A. Heidari and P. Khodaei, *Sep. Purif. Technol.*, 2021, **274**, 119033.
- 10 H. Ruan, C. Guo, H. Yu, J. Shen, C. Gao, A. Sotto and B. Van Der Bruggen, *Ind. Eng. Chem. Res.*, 2016, **55**, 12099–12110.
- 11 S. Liu, Z. Low, H. M. Hegab, Z. Xie, R. Ou, S. Mohammed, G. P. Simon, X. Zhang, L. Zhang and H. Wang, *ACS Appl. Polym. Mater.*, 2021, **3**, 1070–1077.
- 12 A. Bayrami, M. Bagherzadeh, H. Navi and M. Chegeni, *Desalination*, 2022, **521**, 115386.
- 13 X. Lu, Y. Geng, Z. Jia, Y. Yang, H. Huang, Y. Men and L. An, *Sep. Purif. Technol.*, 2021, **269**, 118760.
- 14 B. Forouzesh, R. Hossein, M. Mahsa, F. Rad and M. Baghdadi, *J. Polym. Environ.*, 2022, **30**, 3875–3889.
- 15 Z. Li, D. Zhan, A. Saeed, N. Zhao, J. Wang, W. Xu and J. Liu, *Dalt. Trans.*, 2021, **50**, 8540–8548.
- 16 F. Millange, C. Serre and G. Férey, *Chem. Commun.*, 2002, **8**, 822–823.
- 17 B. M. Jun, Y. A. J. Al-Hamadani, A. Son, C. M. Park, M. Jang, A. Jang, N. C. Kim and Y. Yoon, *Sep. Purif. Technol.*, 2020, **247**, 116947.
- 18 W. Li, S. Henke and A. K. Cheetham, *APL Mater.*, 2014, **2**, 123902.
- 19 P. Zhao, G. I. Lampronti, G. O. Lloyd, M. T. Wharmby, A. K. Cheetham and S. A. T. Redfern, *Chem. Mater.*, 2014, **26**, 1767–1769.
- 20 Y. Cai, D. Chen, N. Li, Q. Xu, H. Li, J. He and J. Lu, *ACS Sustain. Chem. Eng.*, 2019, **7**, 2709–2717.
- 21 W. Li, J. Shi, Y. Zhao, Q. Huo, Y. Sun, Y. Wu, Y. Tian and Z. Jiang, *ACS Sustain. Chem. Eng.*, 2020, **8**, 1831–1839.
- 22 C. Ma, Y. Li, P. Nian, H. Liu, J. Qiu and X. Zhang, *Sep. Purif. Technol.*, 2019, **229**, 115835.
- 23 Y. Song, J. Y. Seo, H. Kim and K. Y. Beak, *Carbohydr. Polym.*, 2019, **222**, 115018.

- 24 R. Zhang, S. Ji, N. Wang, L. Wang, G. Zhang and J. R. Li, *Angew. Chemie - Int. Ed.*, 2014, **53**, 9775–9779.
- 25 W. Wu, M. Jia, J. Su, Z. Li and W. Li, *AIChE J.*, 2020, **66**, 16238.
- 26 Y. Zhao, Y. Liu, X. Wang, X. Huang and Y. F. Xie, 2019, **11**, 13724–13734.
- 27 Y. Peng, Y. Li, Y. Ban, H. Jin, W. Jiao, X. Liu and W. Yang, *Science*, 2014, **346**, 1356–1359.
- 28 H. Liu, Y. Chang, T. Fan and Z. Gu, *Chem. Commun.*, 2016, **2**, 12984–12987.
- 29 Y. Peng, R. Yao and W. Yang, *Chem. Commun.*, 2019, **55**, 3935–3938.
- 30 K. S. Park, Z. Ni, A. P. Côté, J. Y. Choi, R. Huang, F. J. Uribe-Romo, H. K. Chae, M. O’Keeffe and O. M. Yaghi, *Proc. Natl. Acad. Sci. U. S. A.*, 2006, **103**, 10186–10191.
- 31 L. Cao, Z. Lin, W. Shi, Z. Wang, C. Zhang, X. Hu, C. Wang and W. Lin, *J. Am. Chem. Soc.*, 2017, **139**, 7020–7029.
- 32 Y. Song, Y. Pi, X. Feng, K. Ni, Z. Xu, J. S. Chen, Z. Li and W. Lin, *J. Am. Chem. Soc.*, 2020, **142**, 6866–6871.
- 33 X. Feng, Y. Song and W. Lin, *J. Am. Chem. Soc.*, 2021, **143**, 8184–8192.
- 34 L. Cao, Z. Lin, F. Peng, W. Wang, R. Huang, C. Wang, J. Yan, J. Liang, Z. Zhang, T. Zhang, L. Long, J. Sun and W. Lin, *Angew. Chemie Int. Ed.*, 2016, **55**, 4962–4966.
- 35 Y. Xu, S.-L. Yang, G. Li, R. Bu, X.-Y. Liu and E.-Q. Gao, *Chem. Mater.*, 2022, **34**, 5500-5510.
- 36 Y. Cheng, S. R. Tavares, C. M. Doherty, Y. Ying, E. Sarnello, G. Maurin, M. R. Hill, T. Li and D. Zhao, *ACS Appl. Mater. Interfaces*, 2018, **10**, 43095–43103.
- 37 Z. Tao, J. Wu, Y. Zhao, M. Xu, W. Tang, Q. Zhang, L. Gu, D. Liu and Z. Gu, *Nat. Commun.*, 2019, **10**, 1–8.

Chapter 5

Preparation and water purification performance of Zr-PTB membranes

5.1. Introduction

Tricarboxylate ligands are multidentate molecules that can form coordination bonds to metal nodes at three carboxylic acid groups. There are a number of different tricarboxylate ligands, the most widely known being benzene tricarboxylic acid used in HKUST-1.¹ In this chapter, larger tribenzoic ligands with tricarboxylate connectivity are used. Namely 1,3,5-benzenetribenzoic acid and 4''-(pyridine-2,4,6-triyl)tribenzoic acid (Figure 5.1).

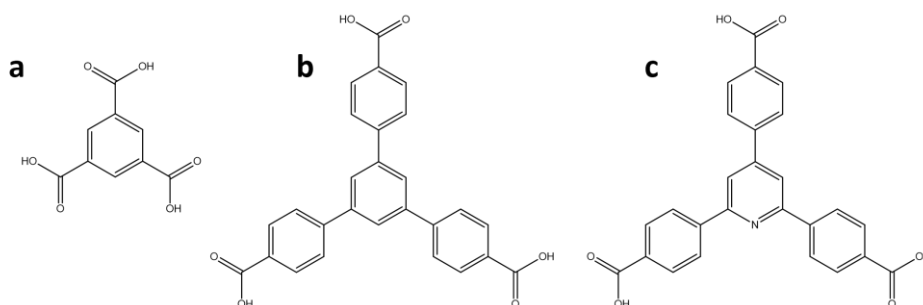


Figure 5.1. (a) Benzene tricarboxylic acid, (b) 1,3,5-benzenetribenzoic acid (H₃BTB), (c) 4''-(pyridine-2,4,6-triyl)tribenzoic acid (H₃PTB).

L. Cao *et al.* first reported the synthesis of 2D Hf-BTB in 2016.² As was utilized in **Chapter 2**, a capping method was employed to overcome the normal Hf₆ cluster geometry and form 2D layers. Formic acid was used as a capping agent so that six of the twelve connection sites on the cluster were protected by formate groups, leaving the remaining six in plane connection sites for BTB moieties (see Figure 5.2).² AFM analysis of the Hf-BTB nanosheets show that monolayer thickness (calculated based on the Van der Waals size of the Hf₆ cluster) was achieved.

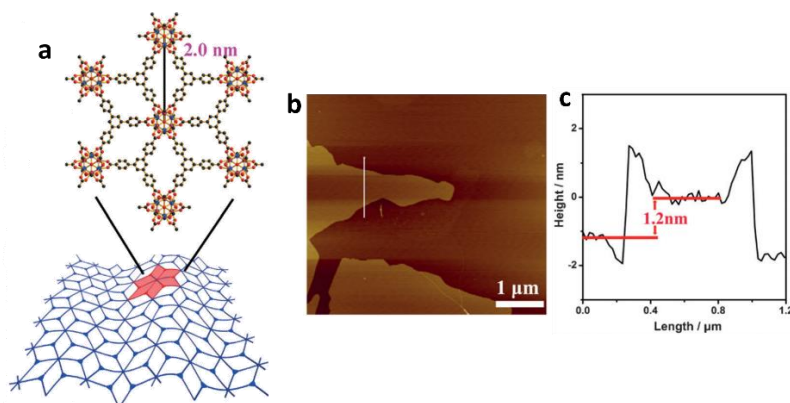


Figure 5.2. (a) Illustration showing the connectivity of the Hf-BTB MOF and layered nanosheet and (b) the AFM topographical profile and (c) associated height profile of a Hf-BTB MON. Figure reproduced from reference 2.

In this initial report and subsequent papers, Hf-BTB is used for catalysis applications.²⁻⁴ The alleviated framework strain when going from 3D to 2D and accessible active sites make Hf-BTB nanosheets catalytically superior to its 3D counterpart.³ Reports have also been published utilizing the Hf-BTB analogue – Zr-BTB, for CO₂ capture and high-resolution isomer separation.^{5,6} When Zr-BTB was incorporated into a polymer matrix, the high aspect ratio of the Zr-BTB nanosheets improved the polymer-filler integration which in turn led to an improved CO₂-selective separation performance.⁵

Finally there has been a single report of the synthesis of Zr-PTB nanosheets by Yan Xu *et al.*⁷ The Zr-PTB nanosheets were used as ultrasensitive pH probes via a cooperative protonation mechanism. AFM data for the Zr-PTB nanosheets was not reported, however SEM images included show that the Zr-PTB and Zr-BTB system have similar topologies (Figure 5.3).

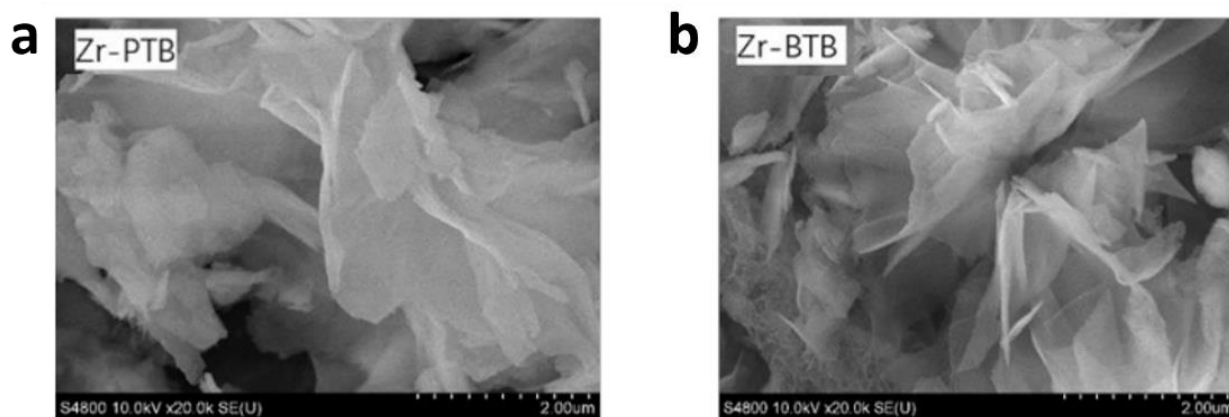


Figure 5.3. SEM images of (a) Zr-PTB and (b) Zr-BTB. Image reproduced from reference 7.

In this work, H₃BTB and H₃PTB ligands were synthesised by postdoctoral research associate Dr Ram R Prasad in the Foster group. The development of literature reported MON synthesis and exfoliation was also carried out by Dr Ram R Prasad.

This chapter builds on the initial screening of MONs for water purification investigated in **Chapter 5**. The chapter recaps the initial rejection results of Zr-BTB and Zr-PTB membranes tested with brilliant blue G (BBG) dye. Zr-PTB membranes are then explored further with additional compression steps, prolonged testing, additive inclusion, and mass loading optimisation to achieve a membrane with stable BBG rejection and permeance performance.

5.2. Results and discussion

5.2.1. Synthesis and characterisation of Zr-tricarboxylates

Synthesis of zirconium tricarboxylate based nanosheets was adapted from the reported syntheses of the Hf-BTB MOF commonly known as NUS-8.^{5,6} Both 1,3,5-benzenetricarboxylic acid (H₃BTB) and 4'-pyridine-2,4,6-triyltribenzoic acid (H₃PTB) were used with zirconium chloride to prepare Zr-tricarboxylate MONs.

Zirconium chloride (ZrCl₄) and either H₃BTB or H₃PTB were dissolved in a mixture of DMF, water and formic acid before heating to 120 °C for 48 h. The resultant white powder was washed firstly with DMF to remove unreacted ligand then with ethanol to remove residual DMF. Samples were analysed by PXRD to ensure synthesis was successful (Figure 4.15). The Zr-BTB and Zr-PTB PXRD patterns have a good match with the reference pattern produced within the Foster group, indicating the synthesis was successful.

Samples were then exfoliated via sonication in acetonitrile and 37 kHz for 12 h. After sonication samples were analysed by PXRD to ensure the structure was retained (Figure 4.15). AFM analysis was carried out to assess the nanosheets produced. Figure 4.16 shows the AFM profiles and scatter plots of associated height profiles of Zr-BTB (a, b) and Zr-PTB (c, d). Both Zr-BTB and Zr-PTB have a high

density of nanosheets between 100 – 300 nm in lateral size, however Zr-PTB (yellow) has more nanosheets under 20 nm in thickness compared to Zr-BTB (orange). Zr-BTB nanosheets have average lateral sizes and heights of 278 and 34 nm. Zr-PTB nanosheets have average lateral sizes and heights of 213 and 26 nm.

While the averages indicate that Zr-BTB nanosheets have larger lateral sizes on average, the spread of lateral sizes in the scatter plot of Zr-PTB nanosheets show a significant amount of > 350 nm MONs (Figure 4.16d). Dynamic light scattering (DLS) measurements were taken to analyse the nanosheet size distributions further. Figure 5.4 shows the DLS particle size distribution data for Zr-BTB (orange) and Zr-PTB (yellow). Due to assumption that the particles measured using a DLS machine are spherical, not 2D, the sizes of the nanosheets given by DLS data cannot be directly compared to the size analysis from AFM data.

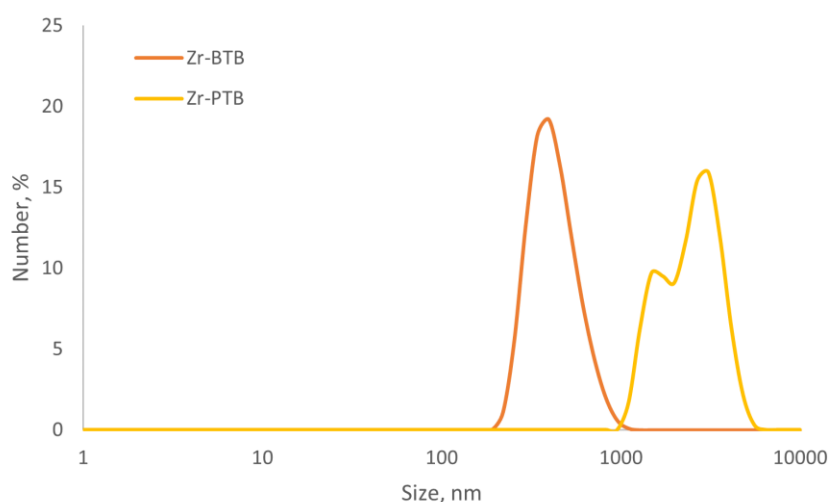


Figure 5.4. DLS particle size distribution collections for Zr-BTB (orange) and Zr-PTB (yellow) nanosheets.

As a general trend, Zr-PTB nanosheets have larger particle sizes than Zr-BTB. Zr-PTB displays two overlapping peaking, indicating two particles sizes. The nature of AFM analysis means smaller particle sizes are over sampled and larger particles are avoided, however DLS shows that there are a significant number of larger Zr-PTB particles.

5.2.2. Zr-tricarboxylate MON membranes on PES supports

Zr-BTB and Zr-PTB membranes were prepared using the following method which was developed in **Chapter 3**. Suspensions of exfoliated nanosheets, in acetonitrile, were further diluted with water before depositing on a PES support membrane via vacuum filtration to give nanosheet mass loadings of 400 mg m^{-2} . PES supports (47 mm diameter) with pores sizes 30 nm were used. Membranes were assembled into a Sterlitech HP4750 Stirred Cell for dead-end cell filtration testing. The test was carried out using a N_2 stream at 1 bar. Samples were taken at approximately 50 mL intervals for the duration of the test and the concentration of the filtrate was measured using a UV-Vis spectrometer. Membranes were tested using 10 mg L^{-1} stock solutions of brilliant blue G (BBG) in water that were prepared at least one day before testing to ensure the dyes were fully dissolved. Each membrane was repeated 3 times to assess the repeatability of the sample.

Figure 4.17 shows the percentage dye rejection and permeance data for Zr-BTB membranes tested with brilliant blue G dye. There is a high degree of variability in the rejection data for this membrane system, this could be due to an inhomogeneous MOF-MON mixture present in the suspension of Zr-BTB after exfoliation. When an aliquot is removed from the exfoliation suspension and diluted in water for membrane preparation, the proportion of MOF and MON in this mixture is unknown. Despite the variability, the general trend of decreasing rejection and permeance is seen.

Figure 5.5 shows the percentage rejection and permeance data for Zr-PTB membranes tested with brilliant blue G. The rejection results show an unusual rejection profile, whereby there is an initially high rejection of 84 %, this drops to an average of 33 % and then increases again to 63 %. There is a decrease in the permeance of the membrane over the course of the experiment. Both the rejection and permeance data have minimal variability in the results.

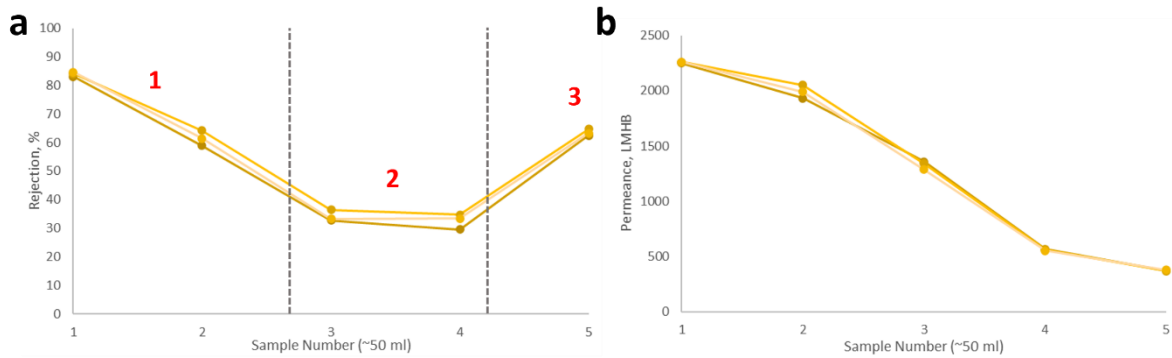


Figure 5.5. (a) Percentage rejection and (b) permeance data for Zr-PTB membranes tested with brilliant blue G dye. Each line of data points represents a repeat experiment. Points 1, 2 and 3, on (a) refer to adsorption, compression, and size exclusion respectively.

Figure 5.5a can be split into 3 sections; 1 – adsorption, 2 – nanosheet compression, 3 – size exclusion.

We propose that the initial rejection is due to an adsorptive mechanism, whereby dye molecules are adsorbing to the MONs and the PES. The rejection decreases as the adsorption sites fill and the dye molecules and water flow between the layers of MONs on the membrane surface. Then, as the nanosheets are compressed onto the membrane surface with the pressure of the feed solution, a more tightly packed continuous active layer is formed on the surface of the membrane (Figure 5.6), allowing the nanosheets to perform a size exclusion mechanism. This also accounts for the decline in permeance, as the more tightly packed the nanosheet active layer is, the barrier to water flow increases.



Figure 5.6. Illustration of Zr-PTB nanosheet compression on a PES support over the duration of the water purification test.

In order to bypass this process and start the water purification test at a size exclusion mechanism, a compression step was introduced to the membrane preparation. This process has some literature precedent; in a report by Y. Peng *et al.* a similar compaction process was employed to facilitate more constrictive interlayer channels.⁸ While the detailed percentage rejection and permeance data was not published, Y. Peng *et al.* concluded that before the compression, the large interlayer spacing between nanosheets enables large amounts of water molecules to transport through the membrane

while having poor rejection. Whereas, after the compression process there is a more well-distributed and compact coverage of nanosheets, resulting in decreased permeance.

5.2.3. Compression step optimisation

Based on the compaction process used by Y. Peng *et al.* whereby water was passed through the membrane prior to testing, an additional compression step to the preparation was introduced into the membrane preparation process. Initially membranes remained in the vacuum filtration set up while an additional 300 ml of water passed through. It was hypothesised that the membrane compression would cause the dye rejection to start around 63 % and either remain at this level or increase further.

Figure 5.7 shows the percentage rejection results of Zr-PTB membranes with no compression step (yellow) and Zr-PTB membrane prepared with a water compression in the vacuum filtration set up directly after deposition (blue). The membranes prepared with a compression step show lower rejection than the membranes without additional compression at the end of the test. Therefore, this method of compression was not successful.

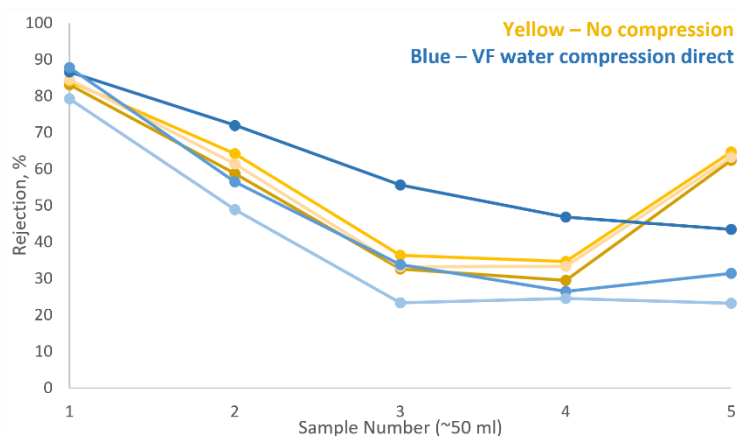


Figure 5.7. Comparison of BBG dye percentage rejection without any additional compression step (yellow) and with a compression step using water in the vacuum filtration set up (VF) (blue). Each line of data points represents a repeat experiment.

In normal preparation the MON-membrane is dried in air overnight before testing is carried out, therefore the water compression in the vacuum filtration set up was tried on dried MON-membranes.

Figure 5.8 shows the percentage rejection results of brilliant blue G dye when tested on Zr-PTB membranes prepared with no additional compression step (yellow) and when Zr-PTB membranes were air dried overnight before a compression step with water in a vacuum filtration set-up. Again, the membranes with additional compression showed lower rejection at the end of the test than the membranes with no compression, meaning this did not emulate the compression seen in initial tests.

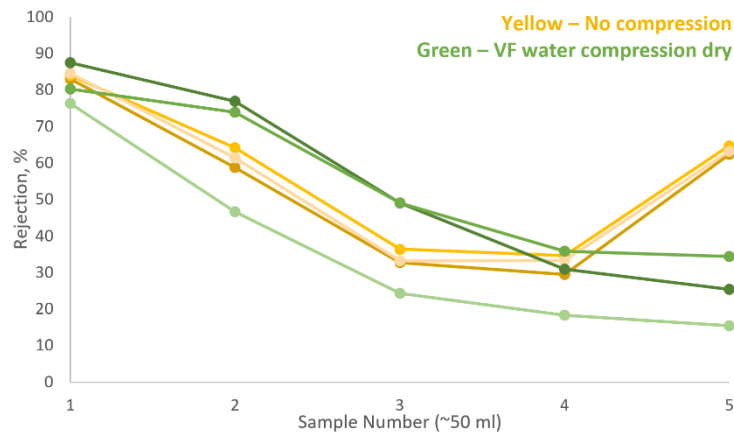


Figure 5.8. Comparison of BBG dye percentage rejection without any additional compression step (yellow) and with a compression step using water in the vacuum filtration set up (VF) after drying overnight (green). Each line of data points represents a repeat experiment.

The compression was next attempted using water as the feed in the dead-end cell on a Zr-PTB membrane that was dried overnight to ascertain if the pressure from the from the N₂ stream was crucial to the compression. 300 ml of deionised water was added to the stirred cell and passed through the membrane with a pressure of 1 bar. Figure 5.9 shows the percentage rejection results of Zr-PTB membranes with no compression step (yellow) compared to Zr-PTB membranes that were dried overnight then compressed with water in the dead-end cell (red). The compressed membrane gave lower rejection results than the membrane with no compression at the end of the test. This also did not show the upwards curve seen in membranes prepared with no compression.

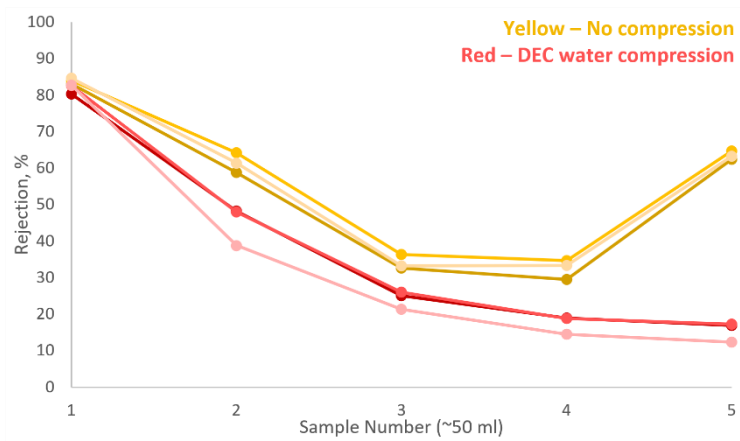


Figure 5.9. Comparison of BBG dye percentage rejection without any additional compression step (yellow) and with a compression step using water in the dead-end cell set up (DEC) after drying overnight (red). Each line of data points represents a repeat experiment.

Scanning electron microscopy (SEM) analysis was carried out on the Zr-PTB membranes with both vacuum filtration and dead-end cell water compression steps (after overnight drying) to compare with the pristine Zr-PTB membranes. This was also compared to SEM images of the Zr-PTB membranes with previously described compressions after water purification testing with brilliant blue G. Figure 5.10 shows the comparison of these SEM images.

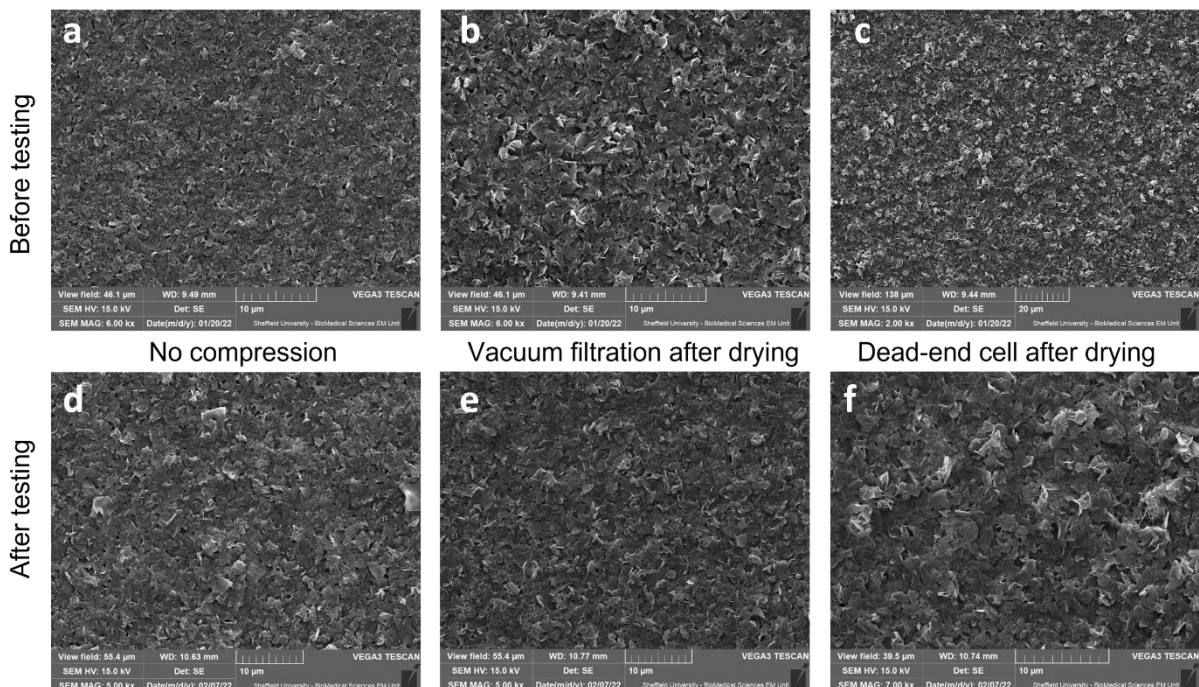


Figure 5.10. SEM images of Zr-PTB membranes without any compression steps before (a) and after testing (d), with a water compression in the vacuum filtration set-up before (b) and after testing (e), and with a water compression in the dead-end cell before (c) and after testing (f).

There is no observable difference between the membranes prepared with different compression steps. There is also no discernible difference between membranes before and after testing. All of the membranes have a full coating of Zr-PTB nanosheets on top of the membrane, with none of the PES support visible. These nanosheets are larger than the lateral sizes observed in the AFM analysis (Figure 4.16), however they are in line with the larger particles observed in the DLS data (Figure 5.4).

Finally, to ascertain if it was dye interactions with the MONs and membrane that was giving rise to the compression effect, Zr-PTB membranes, after overnight air drying, were subject to compression using a brilliant blue G dye solution (10 mg L^{-1}) in the vacuum filtration set up. Figure 5.11 shows the percentage rejection of Zr-PTB membranes after no compression step (yellow) and after a compression step in the vacuum filtration set-up with brilliant blue G (purple). When the Zr-PTB membranes are subject to BBG compression, over the course of the subsequent water purification test, the percentage dye rejection improves.

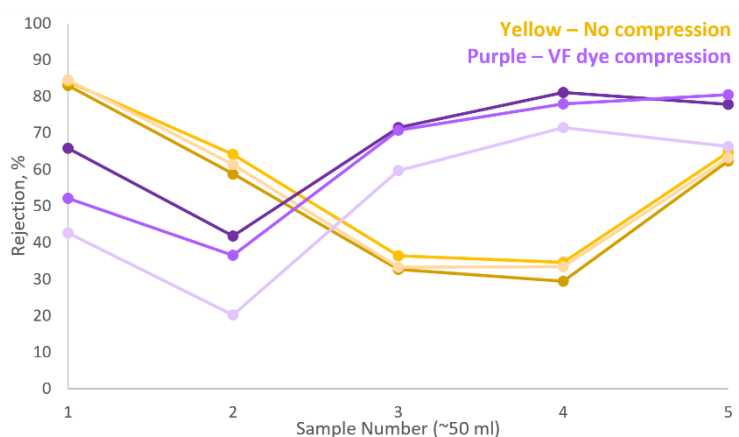


Figure 5.11. Comparison of BBG dye percentage rejection without any addition compression step (yellow) and with a compression step using BBG in the vacuum filtration (VF) set up after drying overnight (purple). Each line of data points represents a repeat experiment.

This confirms that the interactions between the brilliant blue G dye and the Zr-PTB membrane are at least partially responsible for the improvement of dye rejection over the duration of the test.

5.2.4. Prolonged testing

If the compression hypothesis is correct, a longer experiment duration would have the initial drop and then upwards curve seen in Figure 5.5, this would then stabilise at a rejection around 70 %. To evaluate if the Zr-PTB membranes behaved in this way past the initial ~250 mL test, prolonged testing was carried out. The dead-end cell used for testing has a maximum feed capacity of 300 mL, therefore, to extend the test duration, the experiment is paused to be refilled approximately every 250 mL to ensure the cell doesn't run dry. All the feed solution passing through the membrane can affect the surface of the membrane, therefore a small amount (30 - 50 mL) remains in the cell during the experiment. This was repeated twice to give a total filtered volume of approximately 750 mL. Figure 5.12 shows the percentage rejection of brilliant blue G dye over the duration of the extended experiment.

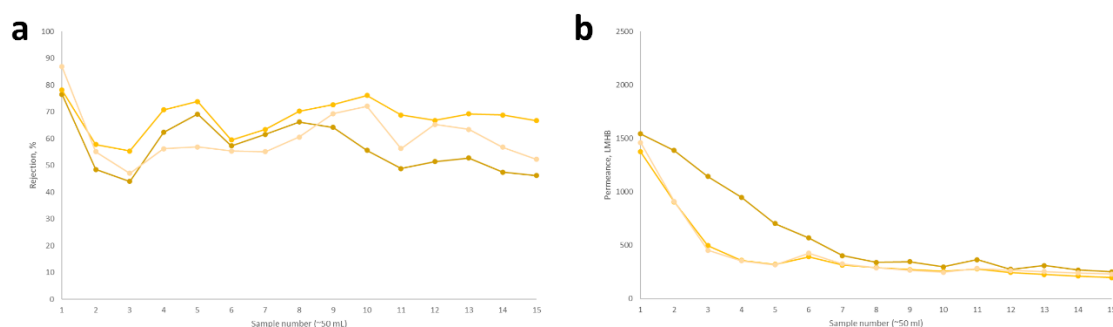


Figure 5.12. Zr-PTB membrane BBG dye percentage rejections (a) and permeance (b) over a prolonged test period. Each line of data points represents a repeat experiment.

Figure 5.12 shows that after roughly 300 mL of dye solution has passed through the membrane, the rejection stabilises at an average of 53 %. Drops in rejection at samples 6 and 11 are where the test is paused to add more feed solution to the dead-end cell. If the feed solution is not poured with care into the cell the Zr-PTB nanosheets in the active layer can be disrupted which affects the rejection. The relative stability of the rejection is good, however the rejection needs improving for this membrane to compete with current published MON-membranes.⁸⁻¹⁰ The permeance plateaus at around 400 mL and reaches an average of 180 LMHB at the end of the test.

After the success of Zr-PTB membranes prepared with a compression step in the vacuum filtration set-up using a brilliant blue G dye solution (10 mg L^{-1}) on the standard test length (see Figure 5.11), Zr-PTB membranes prepared with this dye compression step were evaluated with the prolonged testing technique. Figure 5.13 shows the percentage rejection and permeance data for Zr-PTB membranes prepared using the dye compression step (purple) compared to Zr-PTB membranes prepared with no compression step (yellow). Membranes prepared with the additional compression step have an increased rejection once the experiment has stabilised (around sample 8) compared to the membranes with no additional compression, with the test ending on an average rejection of 76 % compared with 53 % for pristine Zr-PTB. The compressed membranes also initially have a significantly higher permeance, however this rapidly decreases to similar values to the membranes without any compression.

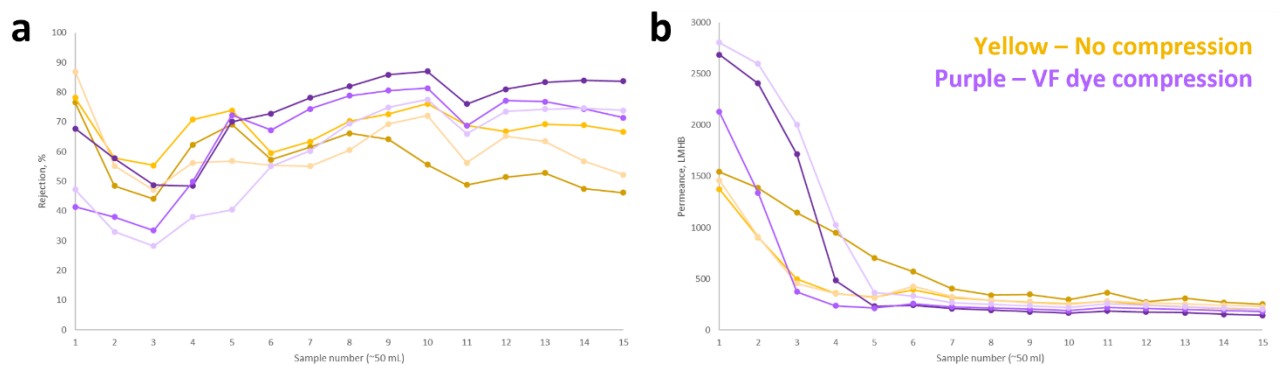


Figure 5.13. Comparison of (a) percentage rejection and (b) permeance data for Zr-PTB membranes without additional compression step (yellow) and with a dye compression step in the vacuum filtration set-up (purple) tested with brilliant blue G dye. Each line of data points represents a repeat experiment.

There is a smaller error with the rejection of the compressed membranes, this is more clearly seen when the results are presented as averages with error bars (Figure 5.14).

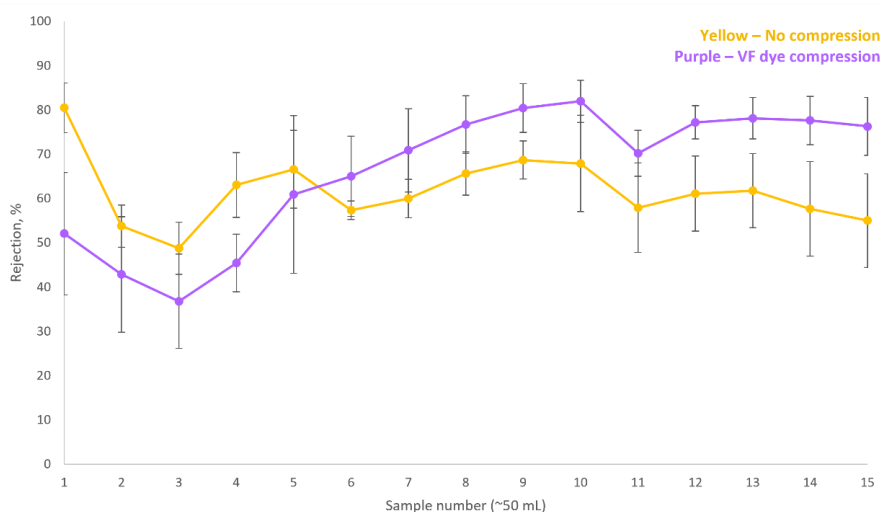


Figure 5.14. Comparison of average percentage rejection and associated error bars for Zr-PTB membranes without additional compression step (yellow) and with a dye compression step in the vacuum filtration set-up (purple) tested with brilliant blue G dye.

5.2.5. Zr-PTB membranes with additives on PES supports

In order to improve the stability of the Zr-PTB membranes over the duration of the water purification test, the inclusion of additives was explored. From an in-depth literature study of MOF/MON-membranes, a wide range of additives were highlighted. A trend of two common additives became clear; graphene oxide and polymeric additives. Of the 32 papers featuring MOF-membranes prepared with additives, eight included graphene oxide.^{11–18} Of the remaining reports, the additive with the next highest incidence is polydopamine (PDA), with six cases.^{16,17,19–22} Other examples of additives that have been used in MOF-membranes include polyethylenimine, polyamide and polyvinylidene fluoride.^{10,23,24} Due to GO and PDA having the highest amount of reports in MOF-membrane literature, these were chosen as the additives tested with Zr-PTB membranes.

5.2.6. Zr-PTB/GO membranes on PES supports

Graphene oxide has been shown to have excellent rejection capabilities, however the permeance achieved with GO membranes leaves a lot of to be desired. Research has shown that combining other materials, specifically MOFs with GO in membranes can improve the membrane permeance due to the porous nature of MOFs.¹³ There have been a number of examples of GO/MOF membranes giving

improved water purification performances than GO or MOF only membranes.^{12,13,15,18} It was using these literature examples that GO/Zr-PTB membranes were prepared.

0.2 mg m⁻² GO and 400 mg m⁻² Zr-PTB were diluted in distilled water before depositing onto a PES support membrane via a vacuum filtration technique. Membranes were then dried in air overnight. All membranes were tested using a Sterlitech HP4750 stirred dead-end cell. Method development of membrane preparation and testing with organic dye solutions is detailed in **Chapter 3**. Each membrane was prepared three times to carry out three repeat water purification tests. Figure 5.15 shows percentage rejection data for Zr-PTB/GO membranes compared to the rejection results for Zr-PTB only membranes.

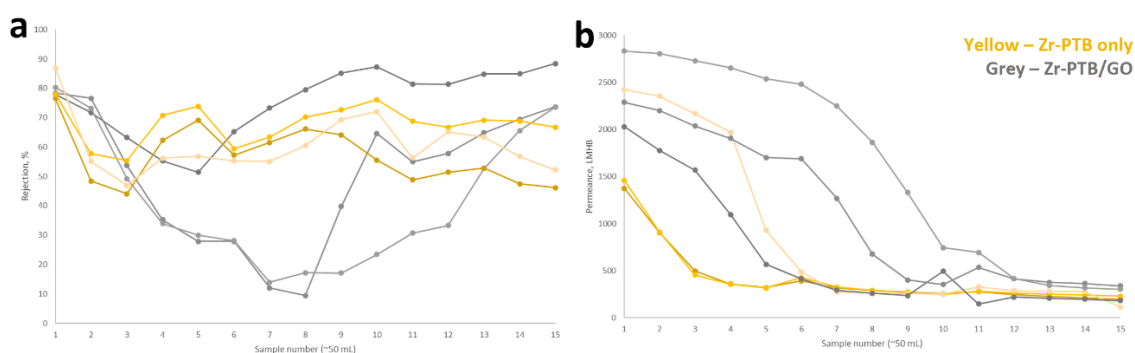


Figure 5.15. Comparison of percentage rejection data for Zr-PTB/GO membranes (grey) and Zr-PTB only membranes (yellow). Each line of data points represents a repeat experiment.

Figure 5.15 shows that Zr-PTB/GO membranes have a higher percentage rejection than Zr-PTB only membranes at the end of the experiment, however the Zr-PTB/GO results are very variable compared to the Zr-PTB only results. The instability and variability of the rejection results for Zr-PTB/GO is undesirable as it leads to inconsistent membranes.

5.2.7. Zr-PTB/PDA membranes on PES supports

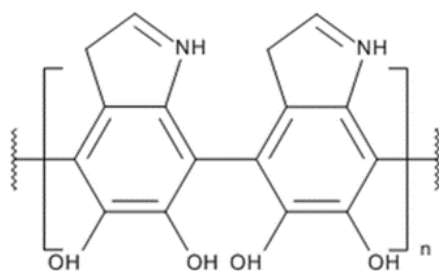


Figure 5.16. Chemical structure of polydopamine.

Research has shown that the structure of polydopamine (PDA) (Figure 5.16) is akin to the adhesive protein in mussels, which have good adhesion to organic and inorganic compounds.²⁵ It is for this reason that PDA can improve the compatibility and interactions between MOFs and polymeric membranes, and in turn improves the stability of these composite membranes.^{16,17} Additionally, PDA can prevent MOF agglomeration during membrane preparation, giving more homogeneous membranes.²⁰

The Zr-PTB/PDA membranes were prepared using an adapted method reported by Liu *et al.*¹⁷ An exfoliated suspension of Zr-PTB was diluted in distilled water. Dopamine hydrochloride (0.1 g) was added to this suspension followed by pH 8.5 Tris-HCl buffer (10 mL). This mixture was stirred at room temperature for 1 h before depositing onto PES support membranes via vacuum filtration. Membranes were then dried in air overnight. All membranes were tested using a Sterlitech HP4750 stirred dead-end cell. Method development of membrane preparation and testing with organic dye solutions is detailed in **Chapter 3**. Each membrane was prepared three times to carry out three repeat water purification tests.

Figure 5.17 shows the percentage rejection and permeance data for Zr-PTB membranes (yellow) compared to Zr-PTB/PDA membranes (teal) tested with brilliant blue G dye. On average the Zr-PTB/PDA membranes give a higher percentage rejection than the Zr-PTB only membranes. Zr-PTB/PDA membranes start with significantly higher permeance however, this drops down to the same level as Zr-PTB only membranes over the course of the test.

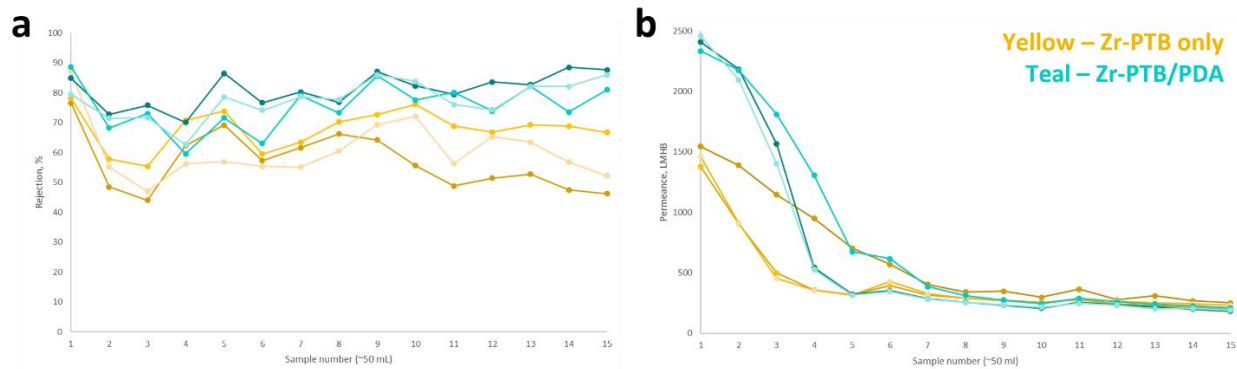


Figure 5.17. Comparison of (a) percentage rejection and (b) permeance data for Zr-PTB membranes (yellow) and Zr-PTB/PDA membranes (teal) tested with brilliant blue G dye. Each line of data points represents a repeat experiment.

Membranes prepared with Zr-PTB, and PDA not only exhibit a higher average percentage rejection, but they also have a smaller associated error. This can be clearly seen when the average rejection results are plotted along with error bars in Figure 5.18. This reduction in variability shows that the PDA improves not only the performance of the membrane, but the homogeneity of the prepared MON surface.

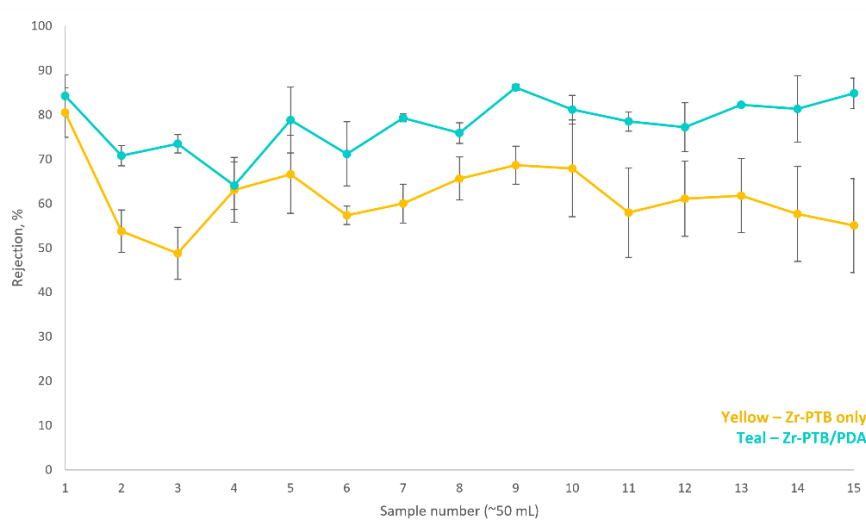


Figure 5.18. Comparison of average percentage rejection and associated error bars for Zr-PTB only (yellow) and Zr-PTB/PDA membranes (teal) tested with brilliant blue G dye.

Optimisation of Zr-PTB loading on Zr-PTB/PDA membranes was carried out to achieve the best possible dye rejection and permeance performance. For initial testing a MON mass loading of 400 mg m^{-2} was used. Lower and upper mass loadings of 200 mg m^{-2} and 800 mg m^{-2} were chosen to determine if the

rejection or permeance could be improved. Figure 5.19 shows the average percentage rejection and permeance data for these membranes.

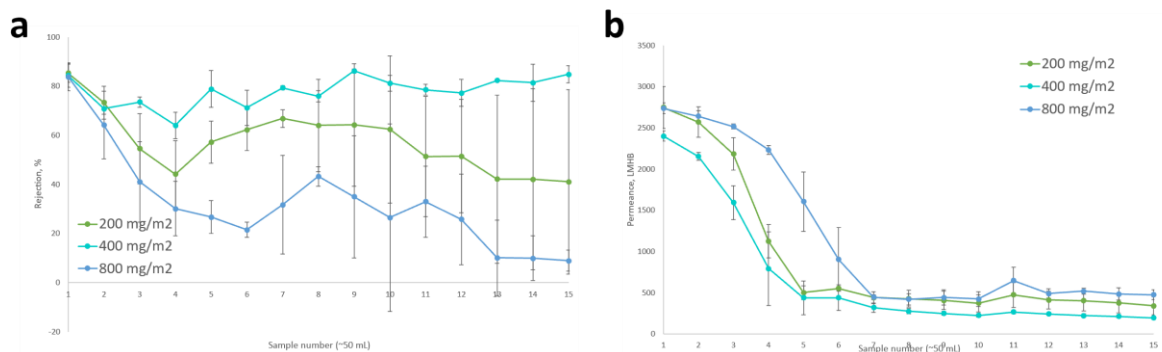


Figure 5.19. Comparison of average percentage rejection (a) and permeance (b) with associated error bars for Zr-PTB/PDA at different mass loadings; 200 mg m⁻² (green), 400 mg m⁻² (teal) and 800 mg m⁻² (blue), tested with brilliant blue G dye.

400 mg m⁻² loading gives the highest percentage rejection over the duration of the experiment. 400 mg m⁻² also gives the lowest permeance at the end of the test, this is to be expected as with higher rejection often comes lower permeance. Unexpectedly 800 mg m⁻², the highest MON loading, gives the lowest rejection and highest permeance. It is expected that the highest MON loading to have the thickest MON active layer on the membrane surface and therefore reject the highest amount of dye. While it is not clear why the highest loading of Zr-PTB leads to the lowest rejection, speculatively it could be due to the large loading disrupting the Zr-PTB/PDA film formation.

SEM analysis of the loading optimisation Zr-PTB/PDA membranes was attempted; however, the PDA interacts too strongly with the electron beam, leading to sample destruction, even with gold coating, meaning images were unable to be recorded.

5.3. Conclusion

In this chapter, the use of Zr-tricarboxylate MONs on PES membranes was explored in depth. Two different Zr-tricarboxylate MONs were investigated, Zr-PTB showed higher rejection and more stable permeance than Zr-BTB and so was taken forward for further optimisation. Zr-PTB membranes showed an unusual trend in the rejection whereby the rejection has an upward curve. The Zr-PTB rejection exhibits adsorption, compression and then size exclusion phases. Compression steps were introduced to the membrane preparation in attempt to move straight to the size exclusion mechanism of rejection. Compression steps with water did not give the desired size exclusion mechanism, however when a brilliant blue G solution was used to compress the membranes in a vacuum filtration set up, the Zr-PTB membranes performed with higher percentage rejection. Speculatively, the negatively charged brilliant blue G dye is interacting with, potentially adsorbing to, the Zr-PTB MONs, giving rise to the compression effect.

Prolonged testing was carried out to identify how the behaviour of the Zr-PTB membranes changes over time. After the initial compression section of the test, the Zr-PTB membrane rejection had a stable rejection of 53%. When an additional brilliant blue G compression is used, the average rejection at the end of the test is 76%.

Graphene oxide and polydopamine were used as additives to the Zr-PTB membranes to improve the performance. Zr-PTB/GO membrane rejection had high variability between results, whereas Zr-PTB/PDA membranes only have a small variation in the rejection results. The average rejection at the end of the Zr-PTB/PDA testing was 84 %, the highest rejection exhibited by any Zr-PTB membrane. MON loading on the Zr-PTB/PDA was optimised, with 400 mg m⁻² giving the optimal result.

5.4. References

- 1 T. Wang, H. Zhu, Q. Zeng and D. Liu, *Adv. Mater. Interfaces*, 2019, **6**, 1900423.
- 2 L. Cao, Z. Lin, F. Peng, W. Wang, R. Huang, C. Wang, J. Yan, J. Liang, Z. Zhang, T. Zhang, L. Long, J. Sun and W. Lin, *Angew. Chemie Int. Ed.*, 2016, **55**, 4962–4966.
- 3 Z. Hu, M. Mahdi, Y. Peng, Y. Qian and B. Zhang, *J. Mater. Chem. A Mater. energy Sustain.*, 2017, 8954–8963.
- 4 X. Feng, Y. Song and W. Lin, *J. Am. Chem. Soc.*, 2021, **143**, 8184–8192.
- 5 Y. Cheng, S. R. Tavares, C. M. Doherty, Y. Ying, E. Sarnello, G. Maurin, M. R. Hill, T. Li and D. Zhao, *ACS Appl. Mater. Interfaces*, 2018, **10**, 43095–43103.
- 6 Z. Tao, J. Wu, Y. Zhao, M. Xu, W. Tang, Q. Zhang, L. Gu, D.-H. Liu and Z. Gu, *Nat. Commun.*, 2019, **10**, 2911.
- 7 Y. Xu, S.-L. Yang, G. Li, R. Bu, X.-Y. Liu and E.-Q. Gao, *Chem. Mater.*, 2022, **34**, 5500–5520.
- 8 Y. Peng, R. Yao and W. Yang, *Chem. Commun.*, 2019, **55**, 3935–3938.
- 9 H. Ang and L. Hong, *ACS Appl. Mater. Interfaces*, 2017, **9**, 28079–28088.
- 10 L. Shu, L.-H. Xie, Y. Meng, T. Liu, C. Zhao and J.-R. Li, *J. Memb. Sci.*, 2020, **603**, 118049.
- 11 G. Yang, D. Zhang, G. Zhu, T. Zhou, M. Song, L. Qu, K. Xiong and H. Li, *RSC Adv.*, 2020, **10**, 8540–8547.
- 12 F. Xiao, M. Cao, R. Chu, X. Hu, W. Shi and Y. Chen, *J. Colloid Interface Sci.*, 2022, **610**, 671–686.
- 13 X. Sui, H. Ding, Z. Yuan, C. F. Leong, K. Goh, W. Li, N. Yang, D. M. D'Alessandro and Y. Chen, *Carbon N. Y.*, 2019, **148**, 277–289.
- 14 M. Dahanayaka, R. Babicheva, Z. Chen, A. W. K. Law, M. S. Wu and K. Zhou, *Appl. Surf. Sci.*, 2020, **503**, 144198.
- 15 H. Li, Y. Yin, L. Zhu, Y. Xiong, X. Li, T. Guo, W. Xing and Q. Xue, *J. Hazard. Mater.*, 2019, **373**, 725–732.
- 16 Y. Liu, M. Zhu, M. Chen, L. Ma, B. Yang, L. Li and W. Tu, *Chem. Eng. J.*, 2019, **359**, 47–57.
- 17 Y. Liu, D. Gan, M. Chen, L. Ma, B. Yang, L. Li, M. Zhu and W. Tu, *Sep. Purif. Technol.*, 2020, **253**, 117552.
- 18 S. Y. Fang, P. Zhang, J. L. Gong, L. Tang, G. M. Zeng, B. Song, W. C. Cao, J. Li and J. Ye, *Chem. Eng. J.*, 2020, **385**, 123400.
- 19 P. Song and Q. Lu, *Sep. Purif. Technol.*, 2020, **238**, 116454.
- 20 M. He, L. Wang, Y. Lv, X. Wang, J. Zhu, Y. Zhang and T. Liu, *Chem. Eng. J.*, 2020, **389**, 124452.
- 21 Y. Gong, S. Gao, Y. Tian, Y. Zhu, W. Fang, Z. Wang and J. Jin, *J. Memb. Sci.*, 2020, **600**, 117874.
- 22 Y. Cai, D. Chen, N. Li, Q. Xu, H. Li, J. He and J. Lu, *ACS Sustain. Chem. Eng.*, 2019, **7**, 2709–2717.
- 23 Z. Gu, S. Yu, J. Zhu, P. Li, X. Gao and R. Zhang, *Desalination*, 2020, **493**, 114661.
- 24 J. E. Efome, D. Rana, T. Matsuura and C. Q. Lan, *Sci. Total Environ.*, 2019, **674**, 355–362.

25 Y. Liu, K. Ai and L. Lu, *Chem. Rev.*, 2014, **114**, 5057–5115.

Chapter 6

Conclusion and Outlook

6.1. Summary of aims

Metal-organic nanosheets (MONs) are a class of two-dimensional (2D) material with diverse modular structures, giving a high degree of tunability which enables a varied set of properties, allowing for their use in a wide range of applications. A growing demand for alternative freshwater sources requires improved water purification techniques which requires new materials to address the fundamental limitations of current systems. This thesis examines the opportunity presented by highly tunable porous 2D nanosheets for addressing the limitations in permeability and selectivity of current water purification materials. The synthesis of 2D analogues of UiO-66 with a range of linkers was investigated, in order to expand available water stable MONs. The incorporation of MONs into composite membranes and the subsequent optimisation of these systems was explored to understand if MONs were a promising filler candidate for the improvement of water purification membranes. This chapter reflects on key developments in the synthesis of water stable MONs and the development of MON membranes, made in this thesis. The industrial applicability of MON membranes and future of this research is also explored.

6.2. Synthesis of water stable MONs

Developing new water stable MONs that are suitable for the use in membranes has been a key theme across this thesis, with several MONs being successfully synthesised. In **Chapter 2**, a range of UiO-66 analogues were synthesised using four different linkers. Defect mediated layered phases of zirconium tetrafluoro terephthalate ($Zr_6(F_4BDC)$) were successfully prepared following methods previously outlined in literature.¹ $Zr_6(F_4BDC)$ nanosheets suspended in water leading to their self-exfoliation. $Zr_6(F_4BDC)$ MONs were characterised via AFM, revealing MONs approaching monolayer thickness with large lateral dimensions (2.4 nm, 593 nm). However, later SEM analysis undertaken in **Chapter 3** revealed the presence of bulk material with an interpenetrated structure, indicating that $Zr_6(F_4BDC)$ had not fully exfoliated into nanosheets. This highlights the challenges in accurately analysing the particle sizes of materials.

Other linkers (terephthalic acid, 2-aminoterephthalic acid and 2-bromoterephthalic acid) regrettably did not form the defect mediated phase that is required to yield nanosheets. However, a mixed linker approach, adding 50 % tetrafluoro terephthalic acid (F_4BDC) and 50 % 2-aminoterephthalic acid (NH_2BDC) to the reaction mixture gave way to the formation of a **fcu/hcp** mixed phase. Exfoliation studies carried out on this system highlighted sonication in acetonitrile, at 37 kHz for 12 h as the optimum conditions to obtain $Zr_6(NH_2:F_4BDC)$ nanosheets. Obtaining these $Zr_6(NH_2:F_4BDC)$ nanosheets, with lateral size and thickness of 419 nm and 1.6 nm was a key achievement of **Chapter 2**. The exact factors leading to the formation of nanosheets in $Zr_6(NH_2:F_4BDC)$ is not known. Speculatively this ratio of linkers (50:50) could be creating order in the reaction mixture that allows the formation of the mixed phase that can be exfoliated. When the NMR is examined, the actual ratio of linkers in the final $Zr_6(NH_2:F_4BDC)$ product is 64:36. F_4BDC and NH_2BDC ligands are different sizes, with different intermolecular interactions, all of which would compete for space within the framework. Speculatively, this could be due to each pore only having enough space to fit one of the larger amino groups.

In this work a range of MONs were synthesised as potential MON-membrane candidates. As discussed above, **Chapter 2** investigated defect-mediated synthesis, producing nanosheets of $Zr_6(F_4BDC)$ and $Zr_6(NH_2:F_4BDC)$. **Chapter 4** saw the synthesis, characterisation, and testing of $CuBDC$, $NH_2-MIL-53$, $ZIF-7$, $Zr-BTB$ and $Zr-PTB$ MONs. AFM showed their nanosheets size to be 213 nm laterally and 23 nm in height, with the particles taking on a nice crystalline shape. These $Zr-PTB$ MONs are not the thinnest nanosheets prepared in this work, compared to $Zr_6(NH_2:F_4BDC)$ at a monolayer height of 1.6 nm, however the yield of the MONs after exfoliation is 100 %, which is very desirable in terms of membrane preparation in an industrially scaled up setting.

As is seen in **Chapter 2** and **Chapter 3**, one of the greatest challenges with MON characterisation is accurate size analysis. AFM, DLS and SEM are all useful techniques for size analysis of these materials, however each has its flaws and does not give a full picture. When carrying out AFM size analysis on

Zr₆(F₄BDC) MONs, the average height and lateral size of the nanosheets was 593 and 2.4 nm respectively. However, after the deposition of these MONs onto the membrane surface, SEM analysis showed that there was unexfoliated bulk material present, that was not seen by the inherent bias to thinner material in AFM. Not being able to get a full picture of the array of material sizes was a significant challenge to this work.

6.3. Development of MON based membranes

Developing the preparation and testing method for MON based membranes was a key challenge in this thesis. The effects of compression, different additives, and the importance of continuous active layers in the preparation of membranes was explored over **Chapters 3 – 5**.

In **Chapter 4**, initial testing of Zr-PTB membranes revealed an unusual upward curve in the rejection results. It was speculated that these Zr-PTB membranes exhibited three phases to the rejection; adsorption, compression, and size exclusion. For this reason, compression steps were introduced to the membrane preparation, a method not used in previous membrane preparation. The systematic development of a compression method led to the use of brilliant blue G as a compression solution, and the hypothesis that the interactions between the dye and MONs causes the compression effect. The unusual profile of Zr-PTB rejection also highlighted the need to develop prolonged water purification testing to fully understand the behaviour of the membranes. This introduction of the compression and prolonged testing highlighted that some MON-membranes could need a stabilising period in order to perform at their maximum potential. Learning from this, testing future MON-membranes for longer periods is a key method to get a fuller picture of membrane performance.

Chapter 3 and **Chapter 5** develop the use of additives to aid the preparation of MON-membranes. After the reported success of Ang and Hong using polydiallyldimethylammonium (PDDA) polymer as an additive, PDDA was used in **Chapter 3** to aid film formation on the support surface.² Systematic Zr₆(F₄BDC) and PDDA loading studies were carried out. **Chapter 3** highlighted the pitfalls of using PDDA as a polymer additive due to its high solubility in water and effect on the dye absorption spectra. It

was identified that PDDA interacts with brilliant blue G and methyl orange dyes, causing non-gaussian peaks with decreased maximum wavelengths. If the PDDA is resolubilising from the membrane surface and passing through the membrane with the permeate solution, then it will affect the permeance absorption measurements. **Chapter 5** moved away from PDDA and investigated graphene oxide and polydopamine (PDA) as potential additives. Methods for including these in MON-membranes were developed, with PDA and Zr-PTB membranes demonstrating acceptable and stable rejection and permeance results.

Zr-PTB membranes prepared with 400 mg m^{-2} MON loading and using PDA as the additive proved to be the most successful candidate. The membrane maintained a stable rejection of brilliant blue G dye over the prolonged water purification test, with an average rejection of 84 % at the end of the experiment, the highest exhibited in this thesis. This result is both successful, as the Zr-PTB/PDA membranes exhibit an improvement of 68 % compared to the pristine PES membrane, and promising, as there are many more avenues to be explored in this research. Finding an additive that improves the membranes performance, interacts well with the nanosheets, and does not degrade during water purification testing is an important factor in preparing successful membranes. Using an additive, such as PDA, can improve the performance and stability of the membranes.

Finally, from the research undertaken in **Chapters 3 – 5** it is clear that the most important factor when preparing a MON-membrane is having a continuous active layer of MONs on the surface of the support membrane. In **Chapter 3**, $\text{Zr}_6(\text{F}_4\text{BDC})$ MONs were used as initial MON candidates due to their stability in water. These membranes were tested using brilliant blue G dye in a stirred dead-end cell, with limited water purification performance. Analysis by SEM showed that, continuous active layers on the support surface did not form. This highlighted the need for a continuous layer of MONs on the support surface to achieve successful water purification results.

Chapter 5 investigated Zr-PTB MON-membranes which displayed a clearly homogenous active layer on the PES support surface when SEM analysis was undertaken, based on previous findings, this is a

crucial property of a successful MON-membrane. The high yield of Zr-PTB MONs is likely a contributing factor to the homogenous active layer, as the exfoliation suspension contained a 100 % of Zr-PTB MONs, whereas the previously discussed $Zr_6(F_4BDC)$ membranes, without a continuous active layer, from **Chapter 3** were prepared using a suspension containing only a 47 % MON yield. A knowledge of the MON yield and how to isolate these MONs from the bulk material in a suspension is a key piece of understanding that would enable more consistent preparation of MON-membranes with continuous active layers.

Learning from these examples, forming a continuous active layer of MONs on the support surface is a crucial starting place for a successful membrane. This can then be combined with an additive that has a strong, stable interactions with the MONs for additional membrane improvements. Finally, only with longer test periods can we understand the behaviour of these MON-membranes.

6.4. Industrial Applicability

Looking at the optimised Zr-PTB/PDA membranes developed in **Chapter 5**, the eventual future work on this system is to scale-up the synthesis and preparation for an industrial setting. Before Zr-PTB or any other MON systems can be considered for industrial applications, research must be carried out into scalable synthesis of MONs. Currently MONs are synthesised at milligram batch levels, this needs to be scaled to gram and kilogram sizes without compromising on quality for MONs to be industrially relevant. Preliminary industrial applicability studies were carried out at Evove facilities, preparing Zr-PTB membranes using a bar coating method and testing using a cross-flow cell. Vacuum deposition is not a scalable method of membranes preparation; therefore, a preparation method called bar coating was used to prepare Zr-PTB membranes. Difficulties arose from transitioning from a vacuum deposition to a bar coating due to the differences in the preparation methods. This led to low dye rejection in the cross-flow testing set-up. Developing a method of scaling up MON-membrane preparation is also a challenge that needs to be overcome to produce industrially viable MON-

membranes. However, the commercialisation of graphene and graphene oxide are promising examples that 2D materials can be scaled up for the use in industrial water purification membranes.

6.5. Outlook

This work has explored the synthesis of novel UiO-66 based MONs, as well as building the method of MON-membrane preparation and testing, new techniques for the Foster group. Extensive membrane screening and optimisation studies have been carried out to develop successful Zr-PTB/PDA membrane candidates with the potential for further improvement. The groundwork on the UiO-66 based MONs can be explored further, incorporating different linkers, and using post-synthetic functionalisation techniques to tailor these systems for a range of applications. Zr-PTB/PDA membranes have been shown to have potential as water purification membranes, the variety of additives, loading optimisation and alternative membrane preparation methods can be exploited to improve these membranes further. Finally, to understand these membranes at a more industrially relevant setting, the use of the cross-flow method of testing should be developed. As has been demonstrated in this body of work, MONs have all the ingredients for the use in successful water purification membranes, and I look forward to seeing where the future of MONs lies within the water purification field and how these materials grow.

6.6. References

- 1 F. C. N. Firth, M. J. Cliffe, D. Vulpe, M. Aragonés-Anglada, P. Z. Moghadam, D. Fairen-Jimenez, B. Slater and C. P. Grey, *J. Mater. Chem. A*, 2019, **7**, 7459–7469.
- 2 H. Ang and L. Hong, *ACS Appl. Mater. Interfaces*, 2017, **9**, 28079–28088.

Chapter 7

Experimental techniques

7.1. Metal-organic nanosheet synthesis and exfoliation

7.1.1. Zr₆(XBDC) compounds

The same general procedure was followed for the synthesis of all Zr₆(XBDC) compounds, with differing quantities of water and formic acid. All of the synthetic procedures were based on a hydrothermal method outlined by F. Firth in 2019.¹ Below the general synthetic method is described, followed by a table showing all of the reagent quantities.

Equimolar amounts of zirconium chloride (ZrCl₄) (0.3 mmol) and terephthalic acid-based ligand (see Table 7.1 for specific ligand) (0.3 mmol) were added to a 12 ml borosilicate glass vial. A quantity (detailed in Table 7.2) of distilled water, formic acid and dimethylformamide (DMF) was then added, and the solution was heated to 120 °C for 24 h. Reaction vials were then cooled to room temperature and the product, a solid white powder, was removed via centrifugation (4500 rpm, 1h). Fresh dimethylformamide (DMF) was then added to the product, this mixture was heated with stirring at 70 °C for a further 24 h to remove any unreacted ligand. Finally, the DMF from the washing stage was removed via centrifugation (4500 rpm, 1 h), the white powder product was dried at room temperature, then activated at 200 °C to remove any coordinated DMF.

Compound	Reagent							
	ZrCl ₄ / mg	F ₄ BDC / mg	NH ₂ BD C / mg	BDC / mg	BrBDC / mg	DMF / mL	Water / mL	Formic acid / mL
Zr₆(F₄BDC)	69.9	71.4	0	0	0	0	1.73	1.15
Zr ₆ (NH ₂ BDC)	69.9	0	54.3	0	0	4	0.4	1.5
	69.9	0	54.3	0	0	4	0.8	1.5
	69.9	0	54.3	0	0	4	1.2	1.5
	69.9	0	54.3	0	0	4	1.5	1.5
	69.9	0	54.3	0	0	4	0.4	2
	69.9	0	54.3	0	0	4	0.8	2
	69.9	0	54.3	0	0	4	1.2	2
	69.9	0	54.3	0	0	4	1.5	2
Zr ₆ (NH ₂ :F ₄ BDC)	69.9	64.3	5.4	0	0	4	0.4	2
	69.9	57.1	10.9	0	0	4	0.4	2
	69.9	50.0	16.3	0	0	4	0.4	2
	69.9	42.9	21.7	0	0	4	0.4	2
	69.9	35.7	27.2	0	0	4	0.4	2
Zr ₆ (BDC)	69.9	0	0	49.8	0	4	0.4	1.5
	69.9	0	0	49.8	0	4	0.8	1.5
	69.9	0	0	49.8	0	4	1.2	1.5
	69.9	0	0	49.8	0	4	1.5	1.5
	69.9	0	0	49.8	0	4	0.4	2
	69.9	0	0	49.8	0	4	0.8	2
	69.9	0	0	49.8	0	4	1.2	2
	69.9	0	0	49.8	0	4	1.5	2
Zr ₆ (BrBDC)	69.9	0	0	0	73.5	4	0.4	1.5
	69.9	0	0	0	73.5	4	0.8	1.5
	69.9	0	0	0	73.5	4	1.2	1.5
	69.9	0	0	0	73.5	4	1.5	1.5
	69.9	0	0	0	73.5	4	0.4	2
	69.9	0	0	0	73.5	4	0.8	2
	69.9	0	0	0	73.5	4	1.2	2
	69.9	0	0	0	73.5	4	1.5	2

Table 7.1. Reagent quantities for synthesis of Zr₆(XBDC) compounds. Rows in bold indicate syntheses that yielded MONs.

7.1.1.1. Zr₆(F₄BDC)

Phase purity of Zr₆(F₄BDC) (yield: 33.5 %) was analysed by PXRD (Figure 7.1) and corroborated by elemental analysis and thermogravimetric analysis (TGA) (Figure 7.2). Elemental analysis: calculated mass for Zr₁₂F₃₆C₇₂O₅₈H₁₄ %: C 24.23; H 0.39; found mass %: C 24.65; H 0.47.

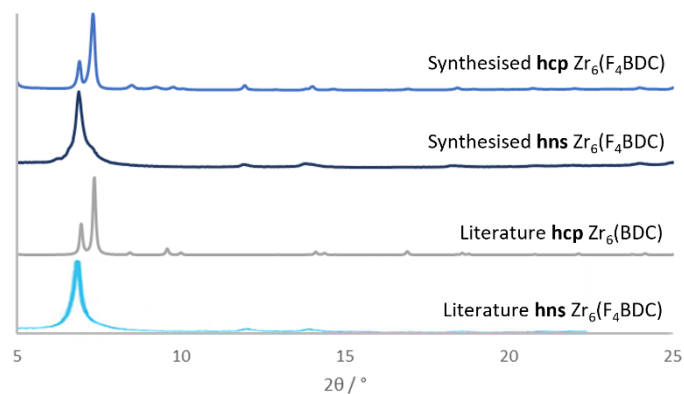


Figure 7.1. Stacked PXRD patterns comparing synthesised **hcp** and **hns** $Zr_6(F_4BDC)$ and literature reported patterns for **hns** $Zr_6(F_4BDC)$ and **hcp** $Zr_6(BDC)$. Literature **hns** $Zr_6(F_4BDC)$ reproduced from reference 1 and literature **hcp** $Zr_6(BDC)$ pattern calculated from single crystal structure in reference 2.

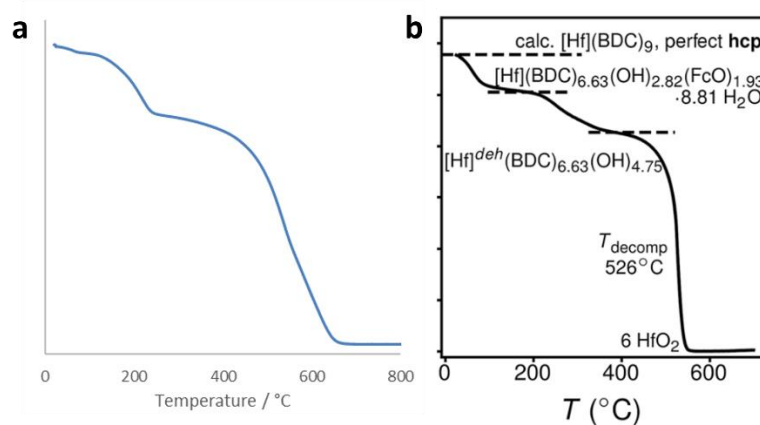


Figure 7.2. TGA trace for (a) as synthesised $Zr_6(F_4BDC)$ compared to (b) literature reported trace adapted from reference 1.

7.1.1.2. $Zr_6(NH_2:F_4BDC)$

Phase purity of $Zr_6(NH_2:F_4BDC)$ (yield: 81.2 %) was analysed by PXRD (Figure 7.3) and corroborated by elemental analysis and thermogravimetric analysis (TGA) (Figure 7.4). Elemental analysis was calculated for 64 % NH_2BDC inclusion: calculated mass for $Zr_{12}N_9C_{72}O_{58}H_{59}$ %: C 25.98; N 2.42; H 1.30; found mass %: C 26.39; N 2.70; H 1.22.

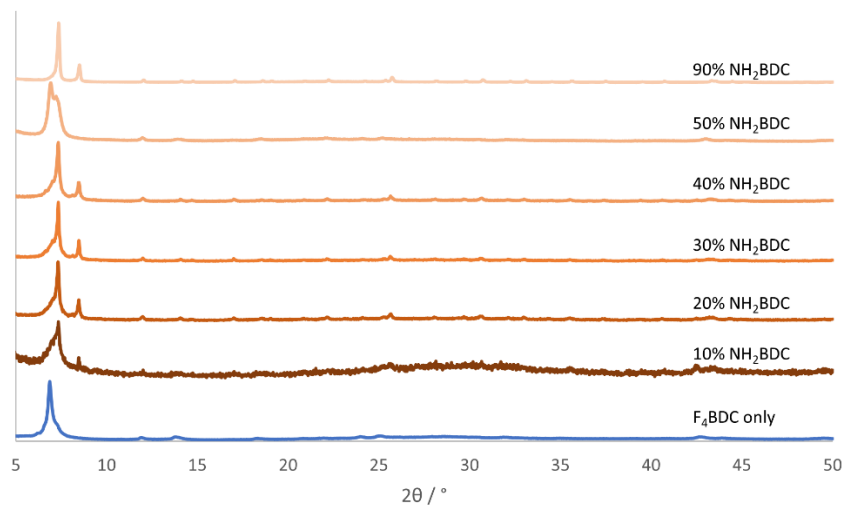


Figure 7.3. Stacked PXRD patterns showing increasing amounts of NH₂BDC included in Zr₆(NH₂:F₄BDC).

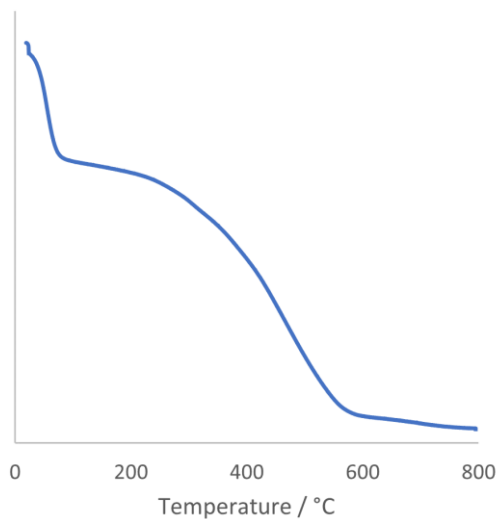


Figure 7.4. TGA trace for as synthesised Zr₆(NH₂:F₄BDC).

Figure 7.5 shows additional AFM image used for size analysis shown in Figure 2.17.

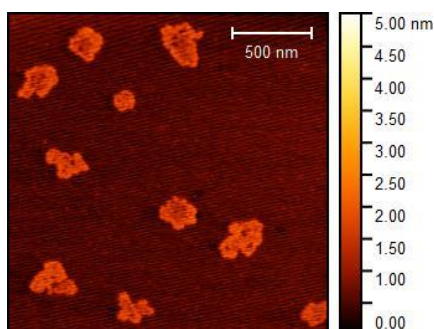


Figure 7.5. AFM topological profile of Zr₆(NH₂:F₄BDC) after exfoliation in ethanol at 37 kHz for 12 h.

7.1.1.3. Zr₆(XBDC) liquid exfoliation

All samples were exfoliated via sonication. Samples were suspended in the chosen solvent at a 1 mg mL⁻¹ concentration. An ultrasound bath was used at 100% power, at temperature <19 °C with stirring to prevent hot-spots. Table 7.2 shows the different sonication conditions used in the exfoliation of Zr₆(XBDC) compounds.

Compound	Solvent	Frequency / Hz	Time / h		
	Acetone	80	0.5		
			1		
			12		
			37	0.5	
				1	
				12	
		Acetonitrile		80	0.5
					1
					12
			37		0.5
					1
					12
	Water	80		0.5	
				1	
				12	
			37	0.5	
				1	
				12	
	Ethanol	80		0.5	
				1	
				12	
			37	0.5	
				1	
				12	
Zr ₆ (NH ₂ :F ₄ BDC)	Ethanol	37		12	
Zr ₆ (F ₄ BDC)	Ethanol	37		12	
Zr ₆ (NH ₂)BDC	Ethanol	37		12	
Zr ₆ (BDC)	Ethanol	37	12		
Zr ₆ (BrBDC)	Ethanol	37	12		

Table 7.2. Sonication conditions for the exfoliation of Zr₆(XBDC) compounds).

7.1.2. CuBDC

CuBDC was synthesised by a solvothermal method.³ Equimolar quantities of copper nitrate trihydrate ($\text{Cu}(\text{NO}_3)_2$) (0.15 mmol, 30 mg) terephthalic acid (BDC) (0.15 mmol, 25 mg) were dissolved in dimethyl formamide (DMF) (5 mL) in a 12 mL borosilicate glass vial and heated to 110 °C for 36 h. After cooling to room temperature, the product was washed with both DMF and diethyl ether using a centrifuge (12,000 rpm, 1 h). The supernatant was removed, and the product was dried to a powder in air. Yield: 94 %. Elemental analysis: calculated mass % for $\text{CuC}_{11}\text{H}_{11}\text{NO}_5$; C 45.43, H 3.81, N 4.82; Found mass %: C 45.10, H 3.91, N 4.65.

CuBDC MOFs were exfoliated via sonication. Samples (5 mg) were suspended in acetonitrile (6 mL) and sonicated at 80 kHz for 12 h. An ultrasound bath was used at 100% power, at temperature <19 °C with stirring to prevent hot-spots. MON yield: 60 % by mass.

7.1.3. NH_2 -MIL-53

2D NH_2 -MIL-53(Al) ($\text{Al}(\text{OH})[\text{H}_2\text{N-BDC}]$), where BDC = 1,4-benzenedicarboxylic acid) was synthesised solvothermally using a method outlined by Z. Li *et al.*⁴ Synthesis of NH_2 -MIL-53(Al) MOF was developed and carried out by Michael Harris, a PhD candidate in the Foster group. Characterisation of the MOF, exfoliation, MON analysis and water purification testing was personally performed. 2-amino terephthalic acid (NH_2BDC) (0.3 mmol, 50 mg) and aluminium chloride ($\text{AlCl}_3 \cdot 6\text{H}_2\text{O}$) (0.3 mmol, 40 mg) were dissolved in 30 ml distilled water. The solution was stirred for 30 minutes before adding urea (0.65 mmol) and stirring for a subsequent 30 minutes. The solution was transferred to Teflon lined steel autoclaves and heated to 150 °C in an oven for 5 hours. After removal from the oven, the reaction mixture was cooled to room temperature. The sample was washed with distilled water three times and removed from the suspension via centrifugation before drying in air (12,000 rpm, 1 h). Figure 7.6 shows the SEM image recorded for this NH_2 -MIL-53 MOF sample. Elemental analysis: calculated mass % for $\text{AlC}_8\text{H}_6\text{NO}_5$; C 43.07, H 2.71, N 6.28; Found mass %; C 31.11, H 3.48, N 5.85.

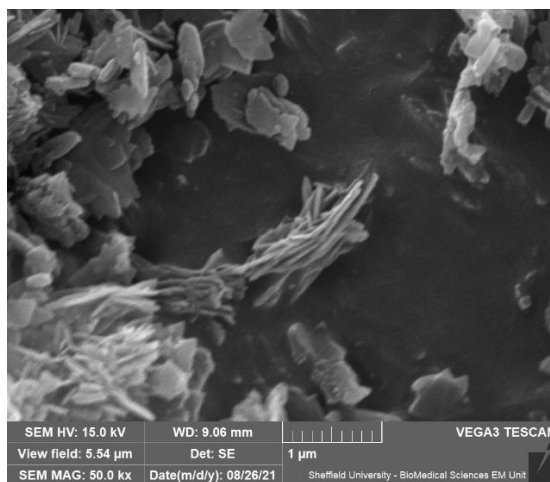


Figure 7.6. SEM image of NH₂-MIL-53.

MIL-53 was exfoliated via sonication. The sample (5 mg) was suspended in acetonitrile (6 mL) and sonicated at 37 Hz for 12 h. An ultrasound bath was used at 100% power, at temperature <19 °C with stirring to prevent hot-spots.

7.1.4. ZIF-7

ZIF-7-III was synthesised using a method reported by H. Lui *et al.*⁵ Amelia Wood, a PhD candidate in the Foster group developed the ZIF-7 nanosheet synthesis and exfoliation method, based on the published examples, that was followed in this chapter. Synthesis, exfoliation, and characterisation of the ZIF-7-III nanosheets was personally carried out following Amelia Wood's guidance. Zinc nitrate (Zn(NO₃)-6H₂O (0.25 mmol, 50 mg) and an excess of benzimidazole (1.6 mmol, 190 mg) were stirred with DMF for 1 h to create a homogenous solution before being kept statically at room temperature for a minimum of 72 h. The purple powder product was removed from the suspension by centrifugation (10,000 rpm, 10 mins) and washed with methanol three times and diethyl ether once before drying at 80 °C in a vacuum oven. Yield: 24 %. Elemental analysis: calculated mass % for ZnC₁₄H₁₀N₄O₂: C 50.12, H 3.00, N 16.7; Found mass %; C 55.78, H 3.26, N 17.76. The ZIF-7 sample not being fully dried after methanol and diethyl ether washing could be the reason for the discrepancy in mass %.

ZIF-7 was exfoliated via sonication. The sample (8 mg) was suspended in a 50:50 mixture of methanol:n-propanol (12 mL) and sonicated at 80 kHz for 2 h. An ultrasound bath was used at 100% power, at temperature <19 °C with stirring to prevent hot-spots. MON yield: 30%.

7.1.5. Zr-tricarboxylates

Synthesis of zirconium tricarboxylate based nanosheets was based on reported syntheses of the Hf-BTB MOF commonly known as NUS-8.^{6,7} Dr Ram R Prasad in the Foster group developed the Zr-BTB and Zr-PTB nanosheet synthesis and exfoliation method, based on the published examples, that was followed in this chapter. Synthesis, exfoliation, and characterisation of the Zr-BTB and Zr-PTB nanosheets was personally carried out following Dr Prasad's guidance. Dr Prasad additionally synthesised the H₃PTB linker used in the synthesis of Zr-PTB.

Zirconium chloride (ZrCl₄) (0.1 mmol) and either H₃BTB (0.1 mmol) or H₃PTB (0.1 mmol) were dissolved in a mixture of DMF (12.5 mL), water (2.5 mL) and formic acid (0.7 mL) before heating to 120 °C for 48 h. The resultant white powder was washed using centrifugation (12,000 rpm, 1 h), twice with DMF to remove unreacted ligand then twice with ethanol to remove residual DMF. The products were then dried to white powders in air. Zr-BTB yield: 54 %. Elemental analysis: calculated mass % for Zr₆C₅₇O₃₂H₄₅: C 38.26, H 2.53, Found mass %; C 35.82, H 3.23, N 0.83. Zr-PTB yield: 66 %. Elemental analysis: calculated mass % for Zr₆C₅₅O₃₂H₄₃N₂: C 36.88, H 2.42, N 1.56; Found mass %; C 36.29, H 3.33, N 4.30. The differences in mass % for both could be due to the DMF from the synthesis and washing stages not being completely removed from the structure.

Zr-tricarboxylate MOFs were exfoliated via sonication. Samples (3.35 mg) were suspended in acetonitrile (8 mL) and sonicated at 37 kHz for 12 h. An ultrasound bath was used at 100% power, at temperature <19 °C with stirring to prevent hot-spots. Zr-BTB MON yield: 24 %. Zr-PTB MON yield: 100 %.

7.1.6. Membrane preparation

Suspensions of exfoliated MONs, in the exfoliation solvent, were further diluted into 70 mL of distilled water and deposited via vacuum filtration onto a PES support membrane (Sterlitech, 47 mm diameter). The membranes were stored separately in petri dishes and dried overnight at room temperature.

7.1.7. MON/PDDA membranes

The MON/PDDA membranes were prepared using an adapted method reported by Liu *et al.*⁸ Suspensions of exfoliated MONs, in the exfoliation solvent, were further diluted into 70 mL of distilled water. To the diluted MON suspension, a 0.1 wt% aqueous solution of PDDA was also added and briefly mixed. Individual volumes of PDDA detailed in **Chapter 2 Section 3.2.3**. This MON/PDDA suspension was deposited via vacuum filtration onto a PES support membrane (Sterlitech, 47 mm diameter). The membranes were stored separately in petri dishes and dried overnight at room temperature.

7.1.8. MON/GO membranes

Suspensions of exfoliated MONs, in the exfoliation solvent, were further diluted into 70 mL of distilled water. To the diluted MON suspension, a suspension of graphene oxide (0.2 mg m^{-2}) was also added and briefly mixed. This MON/GO suspension was deposited via vacuum filtration onto a PES support membrane (Sterlitech, 47 mm diameter). The membranes were stored separately in petri dishes and dried overnight at room temperature.

7.1.9. MON/PDA membranes

Suspensions of exfoliated MONs, in the exfoliation solvent, were further diluted into 70 mL of distilled water. Dopamine chloride (0.1 g) was added to the diluted MON suspension, followed by pH 8.5 Tris-HCl buffer (10 mL). This mixture was stirred at room temperature for 1 h to allow the polydopamine (PDA) reaction to take place. This MON/PDA suspension was deposited via vacuum filtration onto a PES support membrane (Sterlitech, 47 mm diameter). The membranes were stored separately in petri

dishes and dried overnight at room temperature. PDA yields a black product, causing the MON/PDA membrane to be black.

7.2. Characterisation

7.2.1. Atomic force microscopy

All AFM images were recorded using a Bruker Multimode 5 Atomic Force Microscope, operating in soft-tapping mode in air under standard ambient conditions. Bruker OTESPA-R3 silicon cantilevers were used with an approximate drive amplitude of 18.70 mV and frequency of 236 kHz. Samples were prepared by depositing 20 μL of MON suspension onto freshly cleaved mica heated to 85 $^{\circ}\text{C}$. Images were processed using Gwyddion software, version 2.52.⁹

7.2.2. Dynamic light scattering

DLS data were collected using a Malvern Zetasizer Nano Series particle size analyser, using a He-Ne laser at 633 nm, operating in backscatter mode (173 $^{\circ}$). Samples were equilibrated at 298 K for 60 s prior to analysis.

7.2.3. Elemental analysis

Elemental analysis (carbon, hydrogen and nitrogen) was performed using a Vario MICRO cube CHN/S analyser equipped with a thermal conductivity detector. Approximately 2 – 5 mg sample was accurately weighed and sealed into a tin sample capsule. The sample was catalytically combusted and reduced to CO_2 , H_2O and N_2 , which were adsorbed into a collection tube. Gas release upon changes to the temperature allowed detection and subsequent signal integration allowed calculation of elemental percentages by mass.

7.2.4. Nuclear magnetic resonance spectroscopy

Solution-phase ^1H NMR spectroscopy (400 MHz, DMSO-d_6) was performed using a Bruker DPX-400 spectrometer. Approx. 10 mg of powder sample was suspended in a 750 μL DMSO-d_6 solution with 50 μL DCl (35 %) to digest the framework and 1 μL trimethyl silane (TMS) standard.

7.2.5. Powder x-ray diffraction

All powder X-ray diffraction data were collected on a Bruker D8 Advance powder diffractometer with a Cu-K α radiation and focusing Göbel mirrors, operating at 40 kV and 40 mA, recording in the range $4^\circ \leq 2\theta \leq 50^\circ$. Data were collected using a rotating capillary stage, with 0.7 mm borosilicate glass capillaries or on a rotatable flat plate stage. A knife edge to reduce scatter and a beamstop to avoid direct contact between the beam and detector at low angles were used. Data was processed using the Diffrac. Eva software (version 5).

7.2.6. Scanning electron microscopy

Samples for SEM analysis were loaded onto a carbon sticky tab on an aluminium sample stub and coated with approximately 20 nm of gold using an Edwards S150B sputter coater. SEM micrographs were collected using a TESCAN VEGA3 LMU SEM instrument, operating at 15 keV and using the secondary electron detector.

7.2.7. Thermogravimetric analysis

Thermogravimetric analyses were performed using a Perkin-Elmer Pyris 1 thermogravimetric analysis instrument. Approximately 3 – 6 mg of sample was weighed into a ceramic TGA pan. This was held under a nitrogen flow of 20 cm³ min⁻¹ at 30 °C for 10 minutes to purge the sample and allow for equilibration, then ramped to varying end temperatures (see individual traces for details) at 10 °C min⁻¹, unless otherwise specified, to monitor the change in mass. The samples were then held at the final temperature for a 10 min period to allow sample burn off.

7.2.8. Ultraviolet-visible spectroscopy

UV-vis absorption spectra were collected on a Cary 60 UV-vis instrument, using a 1 cm internal length quartz cuvette and Cary WinUV (version 3.00) software in absorbance mode, with a resolution of 1 nm⁻¹. Calculation of absorption coefficients, concentrations and deconvolution were undertaken with Excel software.

7.2.9. Water purification testing

Membranes were assembled into a Sterlitech HP4750 Stirred Cell for dead-end cell filtration testing. The test was carried out using a N₂ stream at 1 bar. Samples were taken at approximately 50 mL intervals for the duration of the test and the concentration of the filtrate was measured using a UV-Vis spectrometer. Membranes were tested using 10 mg L⁻¹ stock solutions of brilliant blue G (BBG) in water that were prepared at least one day before testing to ensure the dyes were fully dissolved. Each membrane was repeated 3 times to assess the repeatability of the sample. Percentage rejection (*R*) of dye was calculated using equation 1:

$$R = \left(\frac{C_f - C_p}{C_f} \right) \times 100\% \quad (1)$$

where *C_f* and *C_p* are the concentrations of the feed and permeate solutions.

Membrane permeance (*F*) was calculated using equation 2:

$$F = \frac{V_p}{A \times t \times \Delta P} \quad (2)$$

where *V_p* is the permeate volume (L), *A* is the effective area of the membrane (m²), *t* is the permeation time (h) and ΔP is the operating pressure (bar). The units of permeance are L m⁻² h⁻¹ bar⁻¹ (LMHB).

Figure 7.7 shows the average percentage rejection and permeance results for PES reference membranes tested with methyl orange (orange), brilliant blue G (blue), methylene blue (green) and rhodamine B (pink). The PES membranes show poor rejection and high permeance for all of the dyes. The rejection is initially higher for methyl orange, brilliant blue G and slightly for rhodamine B, it is likely that this is due to adsorption of the dyes to the PES.

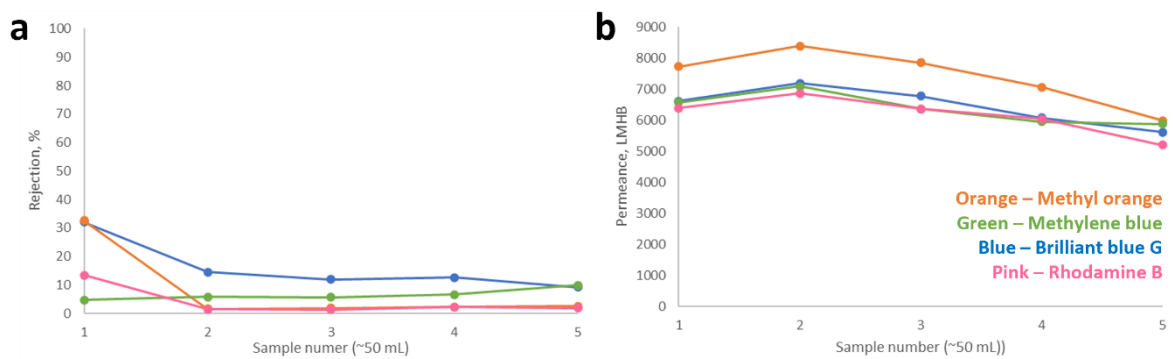


Figure 7.7. (a) Percentage rejection and (b) permeance data for PES reference membranes.

7.3. References

- 1 F. C. N. Firth, M. J. Cliffe, D. Vulpe, M. Aragonés-Anglada, P. Z. Moghadam, D. Fairen-Jimenez, B. Slater and C. P. Grey, *J. Mater. Chem. A*, 2019, **7**, 7459–7469.
- 2 M. J. Cliffe, E. Castillo-Martínez, Y. Wu, J. Lee, A. C. Forse, F. C. N. Firth, P. Z. Moghadam, D. Fairen-Jimenez, M. W. Gaultois, J. A. Hill, O. V. Magdysyuk, B. Slater, A. L. Goodwin and C. P. Grey, *J. Am. Chem. Soc.*, 2017, **139**, 5397–5404.
- 3 C. G. Carson, K. Hardcastle, J. Schwartz, X. Liu, C. Hoffmann, R. A. Gerhardt and R. Tannenbaum, *Eur. J. Inorg. Chem.*, 2009, **16**, 2338–2343.
- 4 Z. Li, D. Zhan, A. Saeed, N. Zhao, J. Wang, W. Xu and J. Liu, *Dalt. Trans.*, 2021, **50**, 8540–8548.
- 5 H. Liu, Y. Chang, T. Fan and Z. Gu, *Chem. Commun.*, 2016, **2**, 12984–12987.
- 6 Z. Tao, J. Wu, Y. Zhao, M. Xu, W. Tang, Q. Zhang, L. Gu, D. Liu and Z. Gu, *Nat. Commun.*, 2019, **10**, 1–8.
- 7 Y. Cheng, S. R. Tavares, C. M. Doherty, Y. Ying, E. Sarnello, G. Maurin, M. R. Hill, T. Li and D. Zhao, *ACS Appl. Mater. Interfaces*, 2018, **10**, 43095–43103.
- 8 Y. Liu, D. Gan, M. Chen, L. Ma, B. Yang, L. Li, M. Zhu and W. Tu, *Sep. Purif. Technol.*, 2020, **253**, 117552.
- 9 D. Nečas and P. Klapetek, *Cent. Eur. J. Phys.*, 2012, **10**, 181-188.



The University of Sheffield, Dec 2020